BRNO UNIVERSITY OF TECHNOLOGY

Faculty of Electrical Engineering
and Communication

MASTER'S THESIS

Brno, 2022 Bc. Lukáš Zezula

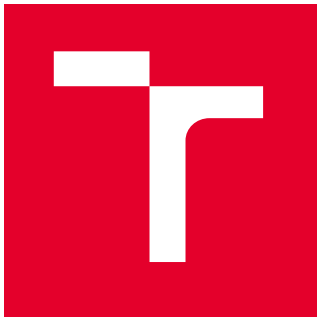

BRNO UNIVERSITY OF TECHNOLOGY

VYSOKÉ UČENÍ TECHNICKÉ V BRNĚ

FACULTY OF ELECTRICAL ENGINEERING AND COMMUNICATION

FAKULTA ELEKTROTECHNIKY
A KOMUNIKAČNÍCH TECHNOLOGIÍ

DEPARTMENT OF CONTROL AND INSTRUMENTATION

ÚSTAV AUTOMATIZACE A MĚŘICÍ TECHNIKY

FAULT RELEVANCE DIAGNOSTICS OF THE PMSM UNDER THE INTER-TURN SHORT CIRCUIT FAULT

DIAGNOSTIKA PORUCHY HLOUBKY MEZIZÁVITOVÉHO ZKRATU PMSM

MASTER'S THESIS
DIPLOMOVÁ PRÁCE

AUTHOR — **Bc. Lukáš Zezula**
AUTOR PRÁCE

SUPERVISOR — **doc. Ing. Petr Blaha, Ph.D.**
VEDOUCÍ PRÁCE

BRNO 2022

BRNO UNIVERSITY OF TECHNOLOGY
FACULTY OF ELECTRICAL ENGINEERING AND COMMUNICATION

Master's Thesis

Master's study program **Cybernetics, Control and Measurements**

Department of Control and Instrumentation

Student: Bc. Lukáš Zezula ***ID:*** 203380

Year of study: 2 ***Academic year:*** 2021/22

TITLE OF THESIS:

Fault relevance diagnostics of the PMSM under the inter-turn short circuit fault

INSTRUCTION:

1. Get acquainted with the inter-turn short circuit fault problem in permanent magnet synchronous motors (PMSM).
2. Become familiar with the state-of-the-art approaches to modeling and diagnostics of inter-turn fault (ITF).
3. Prepare the Simulink scheme containing PMSM model under the field-oriented control which is capable to simulate ITF with changeable relevance.
4. Create an algorithm for the ITF relevance diagnostics and validate it in simulations.
5. Validate the developed fault detection algorithm on the real PMSM which is capable of emulating ITF.

RECOMMENDED LITERATURE:

[1] P. Krause, O. Wasynczuk, S. D. Sudhoff and S. Pekarek. Analysis of electric machinery and drive systems. Third edition. Hoboken, N.J.:Wiley-IEEE Press series on power engineering, 2013. ISBN 978-1-118-02429-4.

[2] S. K. Sul, Control of electric machine drive system. Hoboken, N.J.:Wiley-IEEE Press, 2011. ISBN 978-0-470-59079-9.

Date of project specification: 7.2.2022 ***Deadline for submission:*** 18.5.2022

Supervisor: doc. Ing. Petr Blaha, Ph.D.

doc. Ing. Petr Fiedler, Ph.D.
Chair of study program board

ABSTRACT

This thesis describes the mathematical modeling of a permanent magnet synchronous motor under a stator winding's inter-turn short circuit fault, the discretization of obtained model, and the model-based fault relevance diagnostics. A description of a shorted machine is formed in the stator variables assuming the series-parallel winding connection and transformed into the rotor reference frame using extended Clarke's and Park's transformation matrix. A discrete-time equivalent of the designed model is formed based on the linear time-varying systems approach, considering the electrical angular velocity time-varying parameter with a defined integral. The discrete-time model is transformed into the stator reference frame to maximize the persistence of input signals. The fault relevance diagnostics are then realized based on the recursive parametric estimation of the discrete-time model. In addition, one chapter is dedicated to the control system description since the short circuits may affect state variables differently depending on the control system architecture and tuning. The experimental validation of the presented ideas follows at the end of each chapter.

KEYWORDS

Discrete-time systems, failure analysis, fault detection, mathematical analysis, inter-turn short circuits, mathematical model, model checking, parameter estimation, permanent magnet motors, time-varying systems, vector control.

ABSTRAKT

Tato práce popisuje matematické modelování mezizávitových zkratů fázového vinutí synchronního motoru s permanentními magnety, diskretizaci odvozeného modelu a diagnostiku závažnosti zkratu založenou na referenčním modelu. Popis zkratovaného stroje je vytvořen v proměnných statoru s uvažováním sérioparalelního zapojení vinutí a následně transformován do referenčního rámce rotoru pomocí rozšířené Clarkové a Parkovy transformační matice. Diskrétní ekvivalent navrženého modelu je vytvořen pomocí definované diskretizace lineárních časově variantních systémů, přičemž je uvažováno, že elektrická úhlová rychlost je časově variantní parametr s definovaným integrálem. Diskrétní model je transformován do referenčního rámce statoru, aby se maximalizovala perzistence vstupních signálů. Diagnostika závažnosti zkratu je poté realizována pomocí rekurzivního parametrického odhadu diskrétního modelu. Jedna z kapitol je věnována i popisu řídicího systému, neboť zkraty mohou ovlivnit stavové proměnné různým způsobem v závislosti na architektuře a volbě parametrů řídicího systému. Za každou kapitolou následuje experimentální ověření prezentovaných myšlenek.

KLÍČOVÁ SLOVA

Systémy s diskrétním časem, analýza poruch, detekce poruch, matematická analýza, mezizávitové zkraty, matematický model, ověření modelu, odhad parametrů, motory s permanentními magnety, časově variantní systémy, vektorové řízení.

ROZŠÍŘENÝ ABSTRAKT

Cílem této práce je především návrh diagnostického algoritmu pro detekci závažnosti mezizávitových zkratů statoru synchronního motoru s permanentními magnety. Požadavkem je, aby tento algoritmus běžel v reálném čase na dostupném procesoru AURIX application kit TC277. Tento procesor tedy musí být schopen navržený algoritmus spočítat za méně než $100\,\mu s$ daných periodou vzorkování. V této práci je závažnost zkratu interpretována jako časově variantní parametr modelu motoru, který je detekován algoritmem parametrického odhadu s proměnným koeficientem zapomínání. Návrh algoritmu je poté rozdělen do několika logických kroků: tvorba matematického modelu, diskretizace navrženého modelu a návrh algoritmu pro rekurzivní odhad parametrů diskrétního ekvivalentu. Jedna z kapitol je také věnována návrhu a ladění řídicího systému, neboť významným způsobem ovlivňuje chování motoru při dané poruše a některé proměnné použité při výpočtu akčních zásahů jsou vstupními signály algoritmu identifikace parametrů.

Při tvorbě matematického popisu mezizávitových zkratů se vychází z modelu zdravého motoru definovaného v literatuře. Jelikož má vinutí motoru rozprostřené parametry, je při modelování zkratů uvažována lineární distribuce odporu, indukčností a toku od permanentních magnetů. Aby navržený model lépe popisoval reálný motor, je definován pro sérioparalelní zapojení fázového vinutí. Společně s diferenciálními rovnicemi popisujícími proud jednotlivými statorovými fázemi je stanoven i elektromechanický krouticí moment zkratovaného motoru na základě analýzy energie ve vazebním poli stroje. Výsledný model je poté transformován do referenčního rámce rotoru pomocí rozšířené Clarkové a Parkovy transformační matice. Vzniklý popis umožňuje zkratovaný motor popsat pomocí jeho zdravého modelu a diferenciální rovnice popisující proud zkratem s definovaným odporem. Závažnost zkratu potom udává poměr zkratovaných závitů cívky na statorové fázi ku celkovému počtu závitů této cívky. Validace navrženého modelu je poté realizována srovnáním měřeného zkratového proudu a zpětně indukovaných napětí se simulovanými hodnotami, přičemž je motor v generátorickém režimu hnaný dynamometrem. Validace je realizována pro tři různá zapojení vinutí motoru.

Za účelem řízení stroje v referenčním rámci rotoru je použito zapojení pro dynamickou kompenzaci vazeb mezi jednotlivými složkami proudu. Výzkum autora v oblasti analytického ladění parametrů řídicího systému synchronního motoru s permanentními magnety je v této práci rozšířen tak, aby se maximalizovala robustnost řídicí smyčky a nemohlo při vzniku zkratu dojít k nestabilitě. Jelikož se při identifikaci závažnosti zkratu využívá informace o úhlové rychlosti, je v rámci řídicího systému popsán i pozorovatel úhlové rychlosti a jeho implementace s diskrétním časem, která zachová dynamiku sledování úhlu a rychlosti. Dále jsou popsány transformace

z proměnných statoru do referenčního rámce rotoru a modulace napětí prostorovým vektorem. Řídicí systém je poté nahrán do procesoru a odzkoušen pro tři různá zapojení vinutí na reálném motoru.

Spojitý model zkratovaného motoru je diskretizován na základě definovaného analytického řešení lineárních časově variantních systémů. Je uvažováno, že elektrická úhlová rychlost je časově proměnným parametrem, jehož integrací je elektrický úhel natočení. Na základě tohoto poznatku lze vyjádřit matici přechodů daného systému, a dokonce lze určit i semianalytický diskrétní model. Tento model je poté transformován do referenčního rámce statoru, kde jsou vstupní napěťové signály harmonické průběhy. Oproti referenčnímu rámci rotoru je tedy zajištěna větší perzistence napěťových vstupů, což je výhodné pro parametrickou identifikaci. Diskrétní model je v simulaci srovnaný se spojitým, který byl již validován na základě měření na skutečném stroji.

Aby bylo možné provést rekurzivní parametrický odhad, je nejprve diskrétní model zjednodušen na identifikaci závažnosti zkratu v konkrétní fázi a následně transformován do formy, ve které je jedna složka proudu zatížená zkratem a druhá sleduje chování zdravého motoru. Díky tomuto uspořádání je možné odhadovat parametry zdravé části motoru i v situaci, kdy je přítomen mezizávitový zkrat. Parametry zdravé části jsou odhadovány pomocí rekurzivního algoritmu s proměnným koeficientem zapomínání, aby bylo možné reflektovat mírné změny elektrických parametrů s provozními podmínkami. Dále je zavedena transformace proudové složky motoru zatížené zkratem tak, aby se potlačil vliv zdravých parametrů a k identifikaci zůstali pouze parametry související se zkratem. Tyto jsou poté identifikovány obdobným algoritmem jako zdravé parametry. Rozdíl spočívá v nastavení spodní meze koeficientu zapomínání, kdy u parametrů souvisejících se zkratem je tato mez podstatně nižší a její dosažení indikuje přítomnost mezizávitového zkratu. Za pomoci identifikovaných parametrů je poté spočítána normalizovaná závažnost zkratu, která udává, jaká část cívky na vinutí je zkratována nulovým odporem. Takto definovaný algoritmus je navíc rozšířen o filtraci signálů pro identifikaci adaptivním filtrem, aby bylo dosaženo potlačení rušivých harmonických složek. V této práci je rovněž prezentována analýza rušivých vlivů. Algoritmus detekce závažnosti zkratu je odzkoušen jak v rámci simulace se simulovaným rušením, tak na reálném pohonu.

Author's Declaration

Author:	Bc. Lukáš Zezula
Author's ID:	203380
Paper type:	Master's Thesis
Academic year:	2021/22
Topic:	Fault relevance diagnostics of the PMSM under the inter-turn short circuit fault

I declare that I have written this thesis independently, under the guidance of the advisor and using exclusively the technical references and other sources of information cited in the paper and listed in the comprehensive bibliography at the end of the paper.

As the author, I furthermore declare that, with respect to the creation of this paper, I have not infringed any copyright or violated anyone's personal and/or ownership rights. In this context, I am fully aware of the consequences of breaking Regulation § 11 of the Copyright Act No. 121/2000 Coll. of the Czech Republic, as amended, and of any breach of rights related to intellectual property or introduced within amendments to relevant Acts such as the Intellectual Property Act or the Criminal Code, Act No. 40/2009 Coll. of the Czech Republic, Section 2, Head VI, Part 4.

Brno 10.5.2022 .....

author's signature*

*The author signs only in the printed version.

ACKNOWLEDGEMENT

First of all, I would like to express my sincere gratitude to my supervisor, doc. Ing. Petr Blaha Ph.D. for the valuable guidance, encouragement, and constructive advice during my master's study. Further, I would like to thank Ing. Matúš Kozovský Ph.D. for all his help during the laboratory experiments and advice concerning practical algorithmic implementation. I am also thankful to Ing. Jakub Dokoupil Ph.D. for explaining parametric estimation algorithms and providing recommendations in this field.

Contents

List of Figures

List of Tables

Listings

Introduction

Permanent magnet synchronous motors (PMSMs) are classified as surface-mounted (SPMSMs) and interior (IPMSMs), depending on the position of the permanent magnets. The electrical model of the IPMSM is more complex than that of the SPMSM, but its characteristics better fit the requirements of today's hybrid and electric vehicles.

An inter-turn short circuit or an inter-turn fault (ITF) in the stator winding is the consequence of insulation failures between two or more turns in the same phase. It is the most common fault in electrical machines after bearing failures. ITFs usually occurs due to moisture ingress inside the motor's case, a thermal breakdown between the turns, or another failure. For example, a shattered bearing can get stuck between the coil turns and cause a short circuit. Shorted turns configure an extra circuit loop coupled to flux linkages by other motor windings and the rotor magnets. Owing to the low impedance and high-coupled flux linkage voltage, a high-fault current is thus induced in the shorted winding, which generates ohmic loss and heat that further weaken the surrounding insulation material [1]. This self-heating circle can lead to the machine break down and poses a potential fire hazard. According to the previous statements, there is a high demand for quick and reliable diagnostics of ITF and fault current compensation.

The diagnostics of ITFs exploit two main principles. One is based on processing measured signals and finding patterns that correspond to the fault relevance [2] - [5]; this principle can be highly accurate but is not suitable for online implementation because the embedded device must process large data packets. The other then identifies the resistance, inductance, and other parameters of a shorted phase, which depend on the fault relevance [6] - [9]. However, to achieve the proper functioning of this principle, a relatively precise mathematical description of the fault has to be provided together with a suitable discrete-time equivalent. Otherwise, the fault relevance can not be extracted from the identified parameters with sufficient precision. In some cases, both principles are combined to improve the diagnostic capabilities [10]. This thesis will discuss a novel model-based detection of inter-turn short circuit fault relevance.

Traditionally, many authors describe ITF models in the stator variables. This description is easily formable and allows modeling the asymmetry of the stator windings parameters. However, since the control system is usually defined in the rotor reference frame, it is welcome to transform the model described in stator variables into the rotor reference frame as well. Chapter 1 then aims to develop a simple mathematical ITF model in the rotor reference frame for fast simulations and fault detection using the model-based condition monitoring. The model is formed

in the stator variables, assuming a series-parallel winding connection in Section 1.1. Then the extended transformation matrix is presented in Section 1.2, and the model is transformed into the rotor reference frame in Section 1.3. Model is then realized in MATLAB Simulink environment as described in Section 1.4. In Section 1.5, the validation of the model is provided. For this purpose, the real machine is driven by a dynamometer to the angular velocity setpoint, and currents and electromotive force are measured and compared with the simulated values.

In real applications, a motor is controlled to the velocity setpoint using two cascade control loops. Therefore, the architecture of controllers and their tuning significantly impacts the state variables during the fault. Hence, Chapter 2 discusses the implemented control system. Firstly, an analytical control system parameters tuning is presented in Section 2.1. Then in Section 2.2, the discrete-time equivalent of the designed control system is calculated, and the integral windup phenomenon is handled. Section 2.3 deals with the realization and discrete-time implementation of an angle tracking observer for velocity estimation, and Section 2.4 describes input and output signals transformations and the min-max space vector modulation of the voltage requests. The proposed control system is then applied to control the experimental motor in Section 2.5.

Since this thesis aims for online model-based fault relevance diagnostics and the parametric estimation algorithms primarily support the discrete-time models, the defined continuous-time model must be discretized. Chapter 3 then presents a novel semianalytic discretization of the machine's model. Firstly, the healthy part of the model is discretized in Section 3.1, and then the fault current model's discrete-time equivalent is derived in Section 3.2. In Section 3.3, both model parts are combined and transformed into the stator reference frame, where the persistence of input signals is higher than in the rotor reference frame. Discrete-time model is then compared with the continuous one in Section 3.4.

The algorithm for the fault relevance identification is designed in Chapter 4. In Section 4.1, the discrete-time model is redefined to achieve a description suitable for the parametric estimation. Then the system noise analysis and adaptive filter design follow in Section 4.2. The filter is designed to suppress the periodic distortion in measured currents. Section 4.3 describes the recursive parametric estimation algorithm implemented in this thesis. In Section 4.4, the realization of the fault relevance diagnostic algorithm in MATLAB Simulink is discussed. Section 4.5 then presents the verification of the algorithm within the simulation, and Section 4.6 describes the algorithm validation on the experimental motor.

1 Inter-turn short circuits modeling

For the purpose of inter-turn short circuit modeling, a model of a healthy IPMSM has to be specified. This model provides necessary information about a magnetic flux distribution inside a motor. As mentioned by Sul in [11], the voltages across the stator windings u_a, u_b, u_c are defined as in

$$\begin{bmatrix} u_a \\ u_b \\ u_c \end{bmatrix} = \begin{bmatrix} R_s & 0 & 0 \\ 0 & R_s & 0 \\ 0 & 0 & R_s \end{bmatrix} \cdot \begin{bmatrix} i_a \\ i_b \\ i_c \end{bmatrix} + \frac{\mathrm{d}}{\mathrm{d}t} \begin{bmatrix} \lambda_a \\ \lambda_b \\ \lambda_c \end{bmatrix} \tag{1.1}$$

where R_s is the equivalent resistance of each stator winding (series resistance), i_a, i_b, i_c are the currents flowing in the stator windings, and $\lambda_a, \lambda_b, \lambda_c$ are the total fluxes linking each stator winding, consisting of the flux linkages of the phase windings and the permanent magnets. For a sinusoidal flux distribution, the total fluxes linking are

$$\begin{bmatrix} \lambda_a \\ \lambda_b \\ \lambda_c \end{bmatrix} = \begin{bmatrix} L_{aa} & L_{ab} & L_{ac} \\ L_{ba} & L_{bb} & L_{bc} \\ L_{ca} & L_{cb} & L_{cc} \end{bmatrix} \cdot \begin{bmatrix} i_a \\ i_b \\ i_c \end{bmatrix} + \begin{bmatrix} \lambda_{a,pm} \\ \lambda_{b,pm} \\ \lambda_{c,pm} \end{bmatrix}. \tag{1.2}$$

In (1.2), the phase-self and mutual inductances of the stator windings are defined as in (1.3) and the fluxes of the permanent magnets that link the stator windings as in (1.5). We have

$$\begin{aligned} L_{aa} &= L_s + L_m \cos(2\theta_e) & L_{ab} &= L_{ba} = -\frac{L_s}{2} + L_m \cos\left(2\theta_e - \frac{2\pi}{3}\right) \\ L_{bb} &= L_s + L_m \cos\left(2\theta_e + \frac{2\pi}{3}\right) & L_{ac} &= L_{ca} = -\frac{L_s}{2} + L_m \cos\left(2\theta_e + \frac{2\pi}{3}\right) \\ L_{cc} &= L_s + L_m \cos\left(2\theta_e - \frac{2\pi}{3}\right) & L_{bc} &= L_{cb} = -\frac{L_s}{2} + L_m \cos(2\theta_e). \end{aligned} \tag{1.3}$$

In (1.3), L_s is the average phase-self inductance of each of the stator windings, and L_m denotes the fluctuation in the phase-self inductance and mutual inductance with changing rotor electrical angle θ_e. These inductances can be expressed using d-axis and q-axis inductances:

$$L_s = \frac{L_d + L_q}{3} \qquad L_m = \frac{L_d - L_q}{3}. \tag{1.4}$$

The permanent magnet fluxes that link the stator windings are

$$\begin{aligned} \lambda_{a,pm} &= \lambda_{pm} \cos(\theta_e) \\ \lambda_{b,pm} &= \lambda_{pm} \cos\left(\theta_e - \frac{2\pi}{3}\right) \\ \lambda_{c,pm} &= \lambda_{pm} \cos\left(\theta_e + \frac{2\pi}{3}\right). \end{aligned} \tag{1.5}$$

In (1.5), λ_{pm} stands for the permanent magnets flux linkage.

As mentioned by Krause et al. in [12], the electromagnetic torque of the IPMSM can be established based on the total energy in the coupling field as in

$$T_e = p \begin{bmatrix} i_a \\ i_b \\ i_c \end{bmatrix}^T \cdot \left(\frac{1}{2} \frac{\partial \mathbf{L}}{\partial \theta_e} \begin{bmatrix} i_a \\ i_b \\ i_c \end{bmatrix} + \frac{\partial}{\partial \theta_e} \begin{bmatrix} \lambda_{a,pm} \\ \lambda_{b,pm} \\ \lambda_{c,pm} \end{bmatrix} \right) \tag{1.6}$$

where p stands for the number of pole pairs and $\mathbf{L}$ is the inductance matrix as in (1.2).

Traditionally, many authors describe ITF in the stator variables using the simplified winding architecture models [13]-[14]. These models assume that the stator winding is concentrated into one coil segment (Fig. 1.1), and the inductive couplings in a whole winding are affected by the ITF.

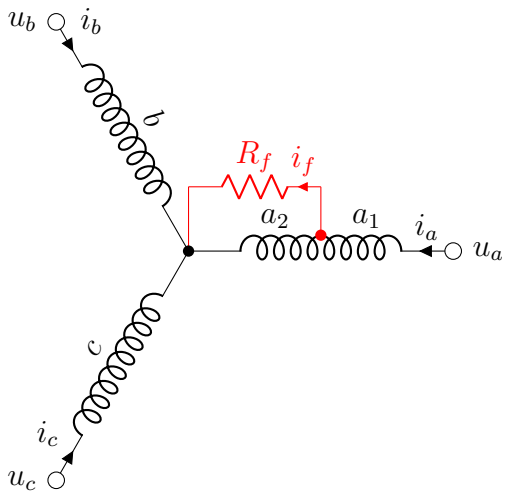

Fig. 1.1: Simplified three-phase winding under the ITF

This assumption leads to a relatively simple expression of the fault current i_f; however, the modeled fault current value is highly overrated due to the demanding inductive couplings. Typically, the phase winding of a motor consists of segments that are geometrically separated from each other. The main advantage of this arrangement is that the ITF cannot easily spread across the whole winding. Due to the segregation, there are also mutual inductances in the same phase; however, such inductances are significantly lower than those that occur due to the ITF and can be neglected. The ITF then affects inductances related only to one coil segment, not a whole winding. Gu presented the models that incorporate different winding configurations (three coils in series or three coils in parallel) in [15]. However, a model of the faulty IPMSM can be formed in a more general way, assuming that the

phase winding comprises n_p branches connected in parallel, and each of the branches consists of n_s coils in series. Figure 1.2 shows a universal phase winding connection applicable in determining a more accurate model of a faulty IPMSM.

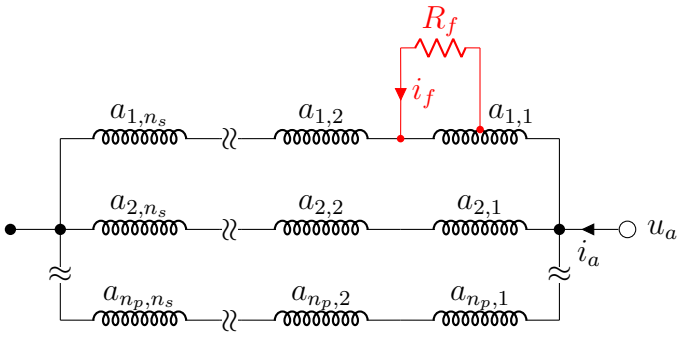

Fig. 1.2: Segregated phase 'a' winding under the ITF

1.1 Model in the stator variables

Due to the presence of an inter-turn short circuit in phase 'a' (Fig. 1.2), an additional fault current i_f occurs. This current flows through the short circuit resistance R_f and can be described by an additional differential equation. Assuming that the coil segments $a_{x,y}$ have an equivalent resistance $\frac{n_p}{n_s}R_s$ and inductance $\frac{n_p}{n_s}L_{aa}$, the previous connection can be simplified into the form presented in Figure 1.3.

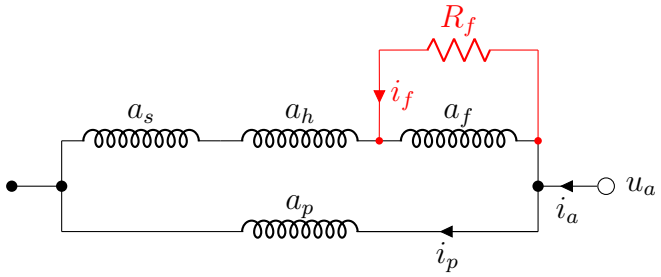

Fig. 1.3: Simplified segregated phase 'a' winding under the ITF

The ITF causes the division of phase segment $a_{1,1}$ into two parts. The part of the coil that is marked as a_h is not shorted, and thus the current $i_a - i_p$ flows through this coil segment. The current $i_a - i_p$ is then divided into the current that flows through the short circuit i_f and the current that flows through the shorted part of the winding a_f. This portion of the phase current is described by $i_a - i_p - i_f$

and contributes to the energy in the coupling field and thus to the electromagnetic torque. The voltage across the winding part a_f is expressed as $u_{a_f} = R_f i_f$ and the voltage across the winding parts a_s and a_h satisfies $u_{a_s a_h} = u_a - u_{a_f} = u_a - R_f i_f$.

The parameters of the equivalent winding model are related to the healthy machine parameters and the fault relevance ratio x_f. This parameter expresses the ratio between the number of shorted turns N_f and the number of total turns N of the shorted phase winding segment; then, $x_f = N_f/N$. The resistances of the healthy a_h, the faulty a_f, the series a_s, and the parallel a_p winding parts are expressed as in

$$\begin{aligned} R_{a_s} &= \frac{(n_s - 1)\, n_p}{n_s} R_s & R_{a_p} &= \frac{n_p}{n_p - 1} R_s \\ R_{a_h} &= \frac{(1 - x_f)\, n_p}{n_s} R_s & R_{a_f} &= \frac{x_f n_p}{n_s} R_s. \end{aligned} \tag{1.7}$$

The following table then describes the inductive couplings inside a machine under the ITF:

Tab. 1.1: Inductive couplings inside a machine under the ITF

Stator part	a_s	a_p	a_h	a_f	b	c
a_s	$\frac{(n_s-1)n_p}{n_s} L_{aa}$	0	0	0	$\frac{(n_s-1)}{n_s} L_{ab}$	$\frac{(n_s-1)}{n_s} L_{ac}$
a_p	0	$\frac{n_p}{n_p-1} L_{aa}$	0	0	L_{ab}	L_{ac}
a_h	0	0	$\frac{(1-x_f)^2 n_p}{n_s} L_{aa}$	$\frac{x_f(1-x_f)n_p}{n_s} L_{aa}$	$\frac{(1-x_f)}{n_s} L_{ab}$	$\frac{(1-x_f)}{n_s} L_{ac}$
a_f	0	0	$\frac{x_f(1-x_f)n_p}{n_s} L_{aa}$	$\frac{x_f^2 n_p}{n_s} L_{aa}$	$\frac{x_f}{n_s} L_{ab}$	$\frac{x_f}{n_s} L_{ac}$
b	$\frac{(n_s-1)}{n_s} L_{ba}$	L_{ba}	$\frac{(1-x_f)}{n_s} L_{ba}$	$\frac{x_f}{n_s} L_{ba}$	L_{bb}	L_{bc}
c	$\frac{(n_s-1)}{n_s} L_{ca}$	L_{ca}	$\frac{(1-x_f)}{n_s} L_{ca}$	$\frac{x_f}{n_s} L_{ca}$	L_{cb}	L_{cc}

Similarly, the permanent magnet fluxes that link the phase 'a' winding parts are defined as in

$$\begin{aligned} \lambda_{a_s,pm} &= \frac{(n_s - 1)}{n_s} \lambda_{a,pm} & \lambda_{a_p,pm} &= \lambda_{a,pm} \\ \lambda_{a_h,pm} &= \frac{(1 - x_f)}{n_s} \lambda_{a,pm} & \lambda_{a_f,pm} &= \frac{x_f}{n_s} \lambda_{a,pm}. \end{aligned} \tag{1.8}$$

Based on the parameters described in (1.7), (1.8), and table 1.1, the voltage and flux equations of the phase 'a' under the ITF are formed as in

$$\begin{bmatrix} u_{a_s a_h} \\ u_{a_f} \\ u_a \end{bmatrix} = \begin{bmatrix} \left(1 - \frac{x_f}{n_s}\right) n_p R_s & 0 & 0 \\ 0 & \frac{x_f}{n_s} n_p R_s & 0 \\ 0 & 0 & \frac{n_p}{n_p - 1} R_s \end{bmatrix} \cdot \begin{bmatrix} i_a - i_p \\ i_a - i_p - i_f \\ i_p \end{bmatrix} + \frac{\mathrm{d}}{\mathrm{d}t} \begin{bmatrix} \lambda_{a_s a_h} \\ \lambda_{a_f} \\ \lambda_{a_p} \end{bmatrix}$$

$$\begin{bmatrix}\lambda_{a_s a_h}\\ \lambda_{a_f}\\ \lambda_{a_p}\end{bmatrix} = \mathbf{L}_f \cdot \begin{bmatrix} i_a - i_p \\ i_a - i_p - i_f \\ i_p \\ i_b \\ i_c \end{bmatrix} + \begin{bmatrix}\left(1-\frac{x_f}{n_s}\right)\lambda_{a,pm}\\ \frac{x_f}{n_s}\lambda_{a,pm}\\ \lambda_{a,pm}\end{bmatrix} \tag{1.9}$$

where

$$\mathbf{L}_f = \begin{bmatrix} \frac{\left(n_s - 2x_f + x_f^2\right)n_p}{n_s}L_{aa} & \frac{x_f\left(1-x_f\right)n_p}{n_s}L_{aa} & 0 & \left(1-\frac{x_f}{n_s}\right)L_{ab} & \left(1-\frac{x_f}{n_s}\right)L_{ac} \\ \frac{x_f\left(1-x_f\right)n_p}{n_s}L_{aa} & \frac{x_f^2 n_p}{n_s}L_{aa} & 0 & \frac{x_f}{n_s}L_{ab} & \frac{x_f}{n_s}L_{ac} \\ 0 & 0 & \frac{n_p}{n_p-1}L_{aa} & L_{ab} & L_{ac} \end{bmatrix}. \tag{1.10}$$

Substituting for voltages in (1.9) and transforming the current vector provides the following form of the voltage and flux equations:

$$\begin{bmatrix} u_a \\ 0 \\ u_a \end{bmatrix} = \begin{bmatrix} \left(1-\frac{x_f}{n_s}\right)n_p R_s & R_f & -\left(1-\frac{x_f}{n_s}\right)n_p R_s \\ \frac{x_f}{n_s}n_p R_s & -\frac{x_f}{n_s}n_p R_s - R_f & -\frac{x_f}{n_s}n_p R_s \\ 0 & 0 & \frac{n_p}{n_p-1}R_s \end{bmatrix} \cdot \begin{bmatrix} i_a \\ i_f \\ i_p \end{bmatrix} + \frac{\mathrm{d}}{\mathrm{d}t}\begin{bmatrix}\lambda_{a_s a_h}\\ \lambda_{a_f}\\ \lambda_{a_p}\end{bmatrix}$$

$$\begin{bmatrix}\lambda_{a_s a_h}\\ \lambda_{a_f}\\ \lambda_{a_p}\end{bmatrix} = \mathbf{L}_f^* \cdot \begin{bmatrix} i_a \\ i_f \\ i_p \\ i_b \\ i_c \end{bmatrix} + \begin{bmatrix}\left(1-\frac{x_f}{n_s}\right)\lambda_{a,pm}\\ \frac{x_f}{n_s}\lambda_{a,pm}\\ \lambda_{a,pm}\end{bmatrix} \tag{1.11}$$

where

$$\mathbf{L}_f^* = \begin{bmatrix} \left(1-\frac{x_f}{n_s}\right)n_p L_{aa} & -\frac{x_f\left(1-x_f\right)n_p}{n_s}L_{aa} & -\left(1-\frac{x_f}{n_s}\right)n_p L_{aa} & \left(1-\frac{x_f}{n_s}\right)L_{ab} & \left(1-\frac{x_f}{n_s}\right)L_{ac} \\ \frac{x_f}{n_s}n_p L_{aa} & -\frac{x_f^2 n_p}{n_s}L_{aa} & -\frac{x_f}{n_s}n_p L_{aa} & \frac{x_f}{n_s}L_{ab} & \frac{x_f}{n_s}L_{ac} \\ 0 & 0 & \frac{n_p}{n_p-1}L_{aa} & L_{ab} & L_{ac} \end{bmatrix}. \tag{1.12}$$

Comparing voltages in (1.11) leads to the algebraic expression of the current flowing through the parallel branch i_p. We have

$$i_p = \frac{n_p - 1}{n_p}\left(i_a - \frac{x_f}{n_s}i_f\right). \tag{1.13}$$

If the number of shorted turns approaches 0; then $x_f = 0$ and the current flowing through the parallel branch satisfies $i_p = \frac{n_p-1}{n_p}i_a$. Hence, the current of the main branch is given as $i_a - i_p = \frac{1}{n_p}i_a$ and the currents flowing through all parallel branches are equal. If $x_f \neq 0$, then the current flowing through the main branch is given as

$i_a - i_p = \frac{1}{n_p} i_a + \frac{n_p - 1}{n_p} \frac{x_f}{n_s} i_f$, yielding in increase of the current in the branch that contains an ITF.

The algebraic expression (1.13) reduces the order of the differential equation system (1.11). Therefore, the model of IPMSM with segregated windings under an ITF can be formed in the stator variables as in

$$\begin{bmatrix} u_a \\ u_b \\ u_c \\ 0 \end{bmatrix} = \begin{bmatrix} \bar{x}_f^* R_s & 0 & 0 & R_f^* \\ 0 & R_s & 0 & 0 \\ 0 & 0 & R_s & 0 \\ x_f^* R_s & 0 & 0 & -x_f^* R_s - R_f^* \end{bmatrix} \cdot \begin{bmatrix} i_a \\ i_b \\ i_c \\ i_f \end{bmatrix} + \frac{\mathrm{d}}{\mathrm{d}t} \begin{bmatrix} \lambda_{a_s a_h} \\ \lambda_b \\ \lambda_c \\ \lambda_{a_f} \end{bmatrix}$$

$$\begin{bmatrix} \lambda_{a_s a_h} \\ \lambda_b \\ \lambda_c \\ \lambda_{a_f} \end{bmatrix} = \mathbf{L}_{f,c} \cdot \begin{bmatrix} i_a \\ i_b \\ i_c \\ i_f \end{bmatrix} + \begin{bmatrix} \bar{x}_f^* \lambda_{a,pm} \\ \lambda_{b,pm} \\ \lambda_{c,pm} \\ x_f^* \lambda_{a,pm} \end{bmatrix} \tag{1.14}$$

where

$$\mathbf{L}_{f,c} = \begin{bmatrix} \bar{x}_f^* L_{aa} & \bar{x}_f^* L_{ab} & \bar{x}_f^* L_{ac} & -x_f^* \bar{x}_f^* L_{aa} + L_f \\ L_{ba} & L_{bb} & L_{bc} & -x_f^* L_{ba} \\ L_{ca} & L_{cb} & L_{cc} & -x_f^* L_{ca} \\ x_f^* L_{aa} & x_f^* L_{ab} & x_f^* L_{ac} & -x_f^{*2} L_{aa} - L_f \end{bmatrix}. \tag{1.15}$$

The parameters x_f^*, $\bar{x}_f^*$, R_f^* and L_f are calculated out of the segregated winding parameters as in

$$\begin{aligned} x_f^* &= \frac{x_f}{n_s} & L_f &= x_f^{*2} n_p (n_s - 1) L_{aa} \\ \bar{x}_f^* &= 1 - \frac{x_f}{n_s} & R_f^* &= x_f^* \bar{x}_f^* (n_p - 1) R_s + R_f. \end{aligned} \tag{1.16}$$

If an ITF occurs in phase 'a', only the current i_a and current $i_a - i_f$, flowing through the a_f segment, contribute to the electromagnetic torque. The fault current i_f then affects the energy in the coupling field and the electromagnetic torque negatively. The electromagnetic torque formula is formed using the transformed current vector and inductance matrix $\mathbf{L}_{f,c}$ as

$$T_e = p \begin{bmatrix} i_a \\ i_b \\ i_c \\ i_a - i_f \end{bmatrix}^T \cdot \left(\frac{1}{2} \frac{\partial \mathbf{L}_{f,c}}{\partial \theta_e} \begin{bmatrix} i_a \\ i_b \\ i_c \\ i_f \end{bmatrix} + \frac{\partial}{\partial \theta_e} \begin{bmatrix} \bar{x}_f^* \lambda_{a,pm} \\ \lambda_{b,pm} \\ \lambda_{c,pm} \\ x_f^* \lambda_{a,pm} \end{bmatrix} \right). \tag{1.17}$$

1.2 Extended transformation matrix

The model defined in the stator variables (1.14), and (1.17) can be transformed into the rotor reference frame using Clarke's transformation matrix, which transforms the model from the stator variables (abc) into the stator reference frame $\alpha - \beta$, and Park's transformation matrix, which transforms the model from $\alpha - \beta$ into the rotor reference frame $d - q$. Due to the ITF, another differential equation related to the fault occurs and these transformation matrices have to be extended. The extension of the transformation matrices aims to transform the stator voltages and currents into the rotor reference frame $d - q$ and to preserve the fault current i_f. Hence, four state variables and three inputs are transformed into the three state variables and two inputs, which leads to the wide rectangular transformation matrix with three rows and four columns. The extended transformation matrix is then formed using the extended Clarke's $\Gamma_{c,ext}$ and Park's $\Gamma_{p,ext}$ transformation matrices as $\Gamma_{ext} = \Gamma_{p,ext} \cdot \Gamma_{c,ext}$. We have

$$\Gamma_{c,ext} = \frac{2}{3}\begin{bmatrix} 1 & -\frac{1}{2} & -\frac{1}{2} & 0 \\ 0 & \frac{\sqrt{3}}{2} & -\frac{\sqrt{3}}{2} & 0 \\ 0 & 0 & 0 & \frac{3}{2} \end{bmatrix} \qquad \Gamma_{p,ext} = \begin{bmatrix} \cos(\theta_e) & \sin(\theta_e) & 0 \\ -\sin(\theta_e) & \cos(\theta_e) & 0 \\ 0 & 0 & 1 \end{bmatrix}. \tag{1.18}$$

The extended transformation matrix reads

$$\Gamma_{ext} = \frac{2}{3}\begin{bmatrix} \cos(\theta_e) & \cos\left(\theta_e - \frac{2\pi}{3}\right) & \cos\left(\theta_e + \frac{2\pi}{3}\right) & 0 \\ -\sin(\theta_e) & -\sin\left(\theta_e - \frac{2\pi}{3}\right) & -\sin\left(\theta_e + \frac{2\pi}{3}\right) & 0 \\ 0 & 0 & 0 & \frac{3}{2} \end{bmatrix}. \tag{1.19}$$

The non-square matrix (1.19) does not have an inverse. However, this matrix has rank 3, allowing us to find a right-hand pseudoinverse that enables transformation from the rotor reference frame into the stator variables:

$$\Gamma_{ext}^{-1} = \Gamma_{ext}^{T}\left(\Gamma_{ext}\Gamma_{ext}^{T}\right)^{-1}. \tag{1.20}$$

The voltages and currents are then transformed as in

$$\begin{bmatrix} u_a \\ u_b \\ u_c \\ 0 \end{bmatrix} = \Gamma_{ext}^{-1}\begin{bmatrix} u_d \\ u_q \\ 0 \end{bmatrix} \qquad \begin{bmatrix} i_a \\ i_b \\ i_c \\ i_f \end{bmatrix} = \Gamma_{ext}^{-1}\begin{bmatrix} i_d \\ i_q \\ i_f \end{bmatrix}. \tag{1.21}$$

Inter-turn short circuits may affect the state variables in the rotor reference frame differently, depending on the form of Clarke's transformation matrix. In (1.18), a direct form of the transformation matrix was used. This form is characterized by

the multiplication factor $\frac{2}{3}$. However, the extended Clarke's transformation matrix may be formed more generally, using the multiplication factor K as in

$$\Gamma^*_{c,ext} = K \begin{bmatrix} 1 & -\frac{1}{2} & -\frac{1}{2} & 0 \\ 0 & \frac{\sqrt{3}}{2} & -\frac{\sqrt{3}}{2} & 0 \\ 0 & 0 & 0 & \frac{1}{K} \end{bmatrix}. \tag{1.22}$$

Use of general extended Clarke's transformation matrix $\Gamma^*_{c,ext}$ results in scaling the voltage inputs and the current outputs. We have

$$\begin{bmatrix} u_d \\ u_q \end{bmatrix} = \frac{2}{3K} \begin{bmatrix} u_{d,in} \\ u_{q,in} \end{bmatrix} \qquad \begin{bmatrix} i_{d,out} \\ i_{q,out} \end{bmatrix} = \frac{3K}{2} \begin{bmatrix} i_d \\ i_q \end{bmatrix}. \tag{1.23}$$

1.3 Model in the rotor reference frame

The differential equations characterizing the $d-q$ currents are determined if (1.21) is substituted into (1.14). The resulting system of differential equations preserves the expression of fault current defined in (1.14). However, derived equations related to the $d-q$ currents are highly complicated and miss the physical meaning. The solution to this problem lies in the state transform, which divides $d-q$ currents into the healthy part and the contribution related to the fault current. We have

$$\begin{bmatrix} i_d \\ i_q \end{bmatrix} = \begin{bmatrix} i_{d,h} \\ i_{q,h} \end{bmatrix} + \frac{2x^*_f}{3} \begin{bmatrix} \cos(\theta_e) \\ -\sin(\theta_e) \end{bmatrix} i_f \tag{1.24}$$

where θ_e stands for the electrical angle. The state transform (1.24) is obtainable if the derived expression of faulty $d-q$ currents is compared with the expression of healthy $d-q$ currents $i_{d,h}$ and $i_{q,h}$ mentioned by Sul in [11]. Hence, $i_{d,h}$ and $i_{q,h}$ are described by the following system of differential equations:

$$\frac{\mathrm{d}}{\mathrm{d}t} \begin{bmatrix} i_{d,h} \\ i_{q,h} \end{bmatrix} = \begin{bmatrix} -\frac{R_s}{L_d} & \frac{L_q}{L_d}\omega_e \\ -\frac{L_d}{L_q}\omega_e & -\frac{R_s}{L_q} \end{bmatrix} \cdot \begin{bmatrix} i_{d,h} \\ i_{q,h} \end{bmatrix} + \begin{bmatrix} \frac{1}{L_d} & 0 & 0 \\ 0 & \frac{1}{L_q} & -\frac{1}{L_q}\omega_e \end{bmatrix} \cdot \begin{bmatrix} u_d \\ u_q \\ \lambda_{pm} \end{bmatrix} \tag{1.25}$$

where L_d and L_q denote inductances in the machine's direct and quadrature axis, R_s and λ_{pm} stand for the equivalent resistance of stator phases and the permanent magnets flux linkage, and ω_e represents the recent electrical angular velocity of a motor.

Similarly, the differential equation that describes the fault current i_f is determined based on the faulty $d-q$ currents and the state transform (1.24). We have

$$\frac{\mathrm{d}}{\mathrm{d}t}\left(3L_f i_f\right) = -R_{f,dq} i_f + 3x^*_f \begin{bmatrix} \cos(\theta_e) \\ -\sin(\theta_e) \end{bmatrix}^T \cdot \begin{bmatrix} u_d \\ u_q \end{bmatrix} \tag{1.26}$$

where $R_{f,dq} = x_f^* \left(3 - 2x_f^*\right) R_s + 3R_f^*$ and L_f, x_f^* and R_f^* are defined as in (1.16).

The electromagnetic torque of IPMSM under the ITF is obtained by substituting (1.21) and (1.24) into (1.17), yielding

$$T_e = \frac{3}{2} p i_{q,h} (\lambda_{pm} + (L_d - L_q) i_{d,h}) + \frac{1}{2} p \frac{\partial L_f}{\partial \theta_e} i_f^2. \tag{1.27}$$

The electromagnetic torque is also divided into the healthy part and the fluctuation caused by i_f, just as the $d-q$ currents (1.24). If the number of shorted turns approaches 0, then out of (1.26), the fault current is also approaching 0; thus, i_d, i_q, and T_e are given only by the healthy part of the model. If $x_f^* \neq 0$, the distortion with the dominant frequency $2\omega_e$ occurs in the d-q currents and the electromagnetic torque. This fact is provable based on the definition of fault current and trigonometric identities.

The presented model was derived for an ITF in phase 'a'. However, the same procedure can be applied to determine machine models under ITFs in phases 'b' and 'c'. The model of faulty IPMSM with segregated windings and ITF in phase 'a' is then extendable to simulate short circuits in the different phases, using the redefinition

$$\begin{aligned} L_f &= {x_f^*}^2 n_p (n_s - 1)(L_s + L_m \cos(2\theta_e + \phi)) \\ \frac{\mathrm{d}}{\mathrm{d}t}(3 L_f i_f) &= -R_{f,dq} i_f + 3 x_f^* \begin{bmatrix} \cos(\theta_e + \frac{\phi}{2}) \\ -\sin(\theta_e + \frac{\phi}{2}) \end{bmatrix}^T \cdot \begin{bmatrix} u_d \\ u_q \end{bmatrix} \\ \begin{bmatrix} i_d \\ i_q \end{bmatrix} &= \begin{bmatrix} i_{d,h} \\ i_{q,h} \end{bmatrix} + \frac{2 x_f^*}{3} \begin{bmatrix} \cos(\theta_e + \frac{\phi}{2}) \\ -\sin(\theta_e + \frac{\phi}{2}) \end{bmatrix} i_f \end{aligned} \tag{1.28}$$

where if $\phi = 0$ then the ITF is in phase 'a', if $\phi = \frac{2\pi}{3}$ then the ITF is in phase 'b', and if $\phi = -\frac{2\pi}{3}$ then the ITF is in phase 'c'.

Note that if the parallel branches of phase winding consist only of one coil segment, then $n_s = 1$ and $L_f = 0$, and it is possible to describe the fault current algebraically. For this type of winding connection, the fault current is defined as in

$$i_f = \frac{3 x_f^*}{R_{f,dq}} \begin{bmatrix} \cos(\theta_e + \frac{\phi}{2}) \\ -\sin(\theta_e + \frac{\phi}{2}) \end{bmatrix}^T \cdot \begin{bmatrix} u_d \\ u_q \end{bmatrix}. \tag{1.29}$$

The phase shift and the frequency of i_f then correspond with the phase shift and the frequency of i_a, i_b, or i_c, depending on ϕ.

1.4 Realization of the model in MATLAB Simulink

According to Section 1.3, the model of IPMSM under the ITF is divided into two parts. One describes the healthy IPMSM model, and the other is related to the ITF. Thus it is possible to model these parts independently on each other and combine them in the model's output. Figure 1.4 shows the core of the model.

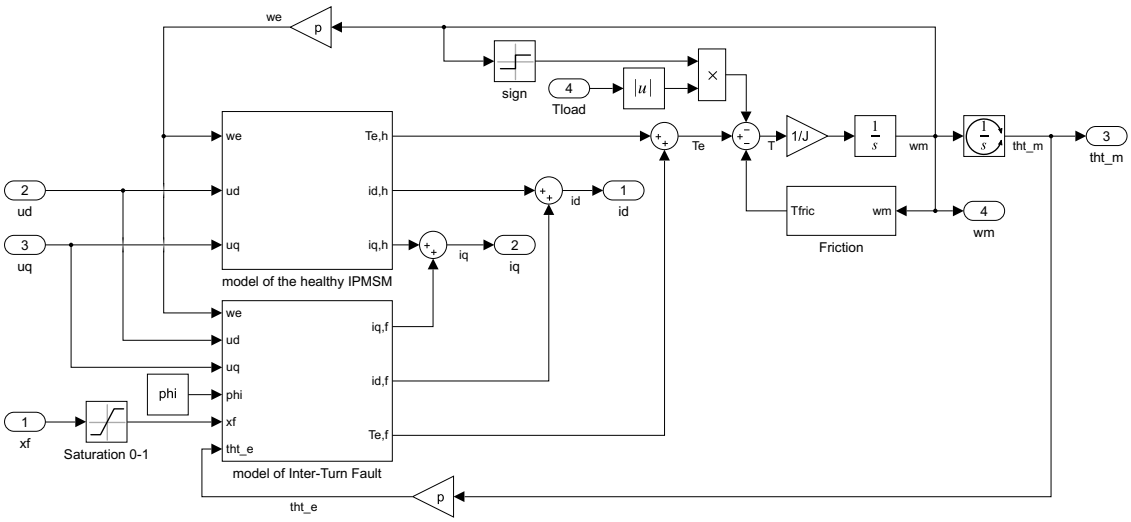

Fig. 1.4: Model of IPMSM under the ITF

As shown in Figure 1.4, a mechanical subsystem is also modeled in the core. A motion equation that describes a mechanical angular velocity ω_m is formed as in

$$\frac{\mathrm{d}\omega_m}{\mathrm{d}t} = \frac{1}{J}\left(T_e - T_{fric} - T_{load}\right) \tag{1.30}$$

where J stands for the moment of inertia, T_{load} is a torque load connected to a shaft of machine, and T_{fric} is dynamic friction torque inside a motor. We have

$$T_{fric} = \mathrm{sign}(\omega_m)\left(B|\omega_m| + T_{dry}\right). \tag{1.31}$$

Parameters B and T_{dry} express the viscous friction coefficient and the dry friction. The static friction is neglected.

A mechanical angular velocity is the first derivative of mechanical angle θ_m; then $\mathrm{d}\theta_m/\mathrm{d}t = \omega_m$. Since the machine is controlled to the angular velocity setpoint, the mechanical angle tends to grow to infinity. Hence, the wrap state function is implemented in the model presented in Figure 1.4. This function normalizes the mechanical angle to interval $\langle -\pi, \pi \rangle$, preventing the value of θ_m from overwhelming. The relation between the mechanical and electrical angle and mechanical and electrical angular velocity is then defined as in

$$\theta_e = p\theta_m \qquad\qquad \omega_e = p\omega_m \tag{1.32}$$

where p is the number of pole pairs.

The healthy part of the model of IPMSM under the ITF is then formed using a flux-based model of IPMSM in $d-q$ coordinates (Fig. 1.5).

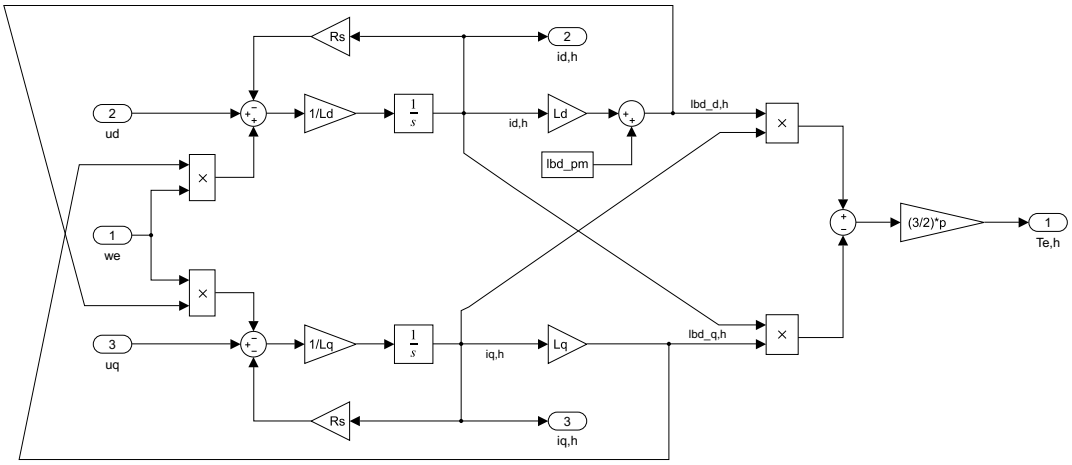

Fig. 1.5: Healthy part of the model of IPMSM under the ITF

Due to the demand for changeable fault relevance during the simulation, a relatively complicated expression of parameters x_f^*, $R_{f,dq}$, L_f, and $\mathrm{d}L_f/\mathrm{d}\theta_e$ occurs. Therefore, the model of ITF is divided into two parts to preserve clarity. One part of the model describes the varying parameters (Fig. 1.6), and the other defines the fault current and torque (Fig. 1.7).

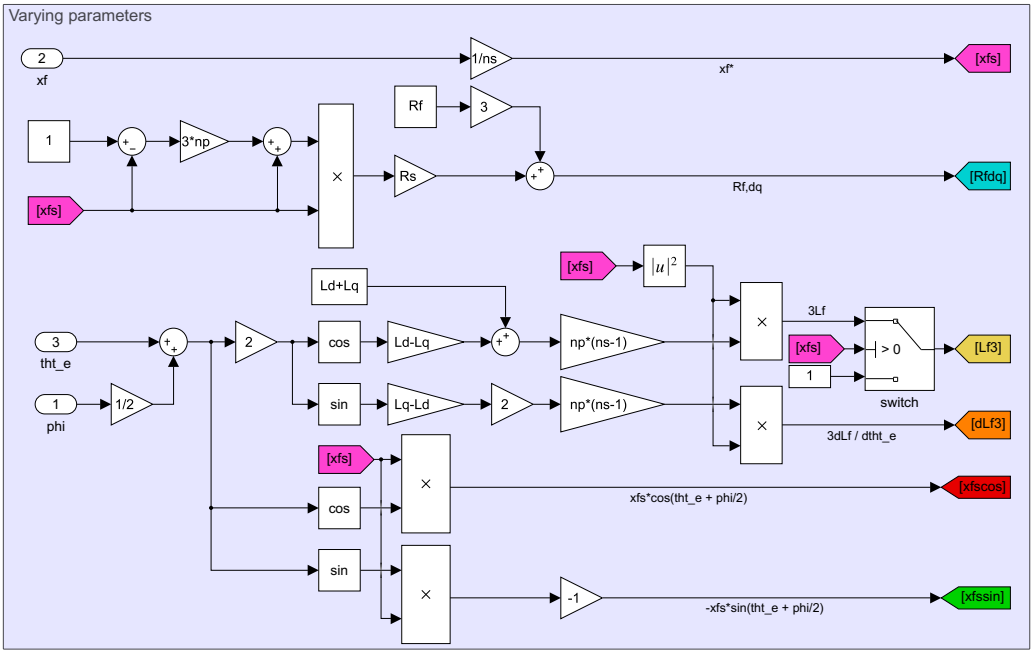

Fig. 1.6: Varying parameters in the ITF model

As shown in Figure 1.6, switching of L_f is present. If $x_f = 0$, then $L_f = 0$, and a division by 0 occurs in the fault current model. Therefore, to prevent this situation, the value of L_f is switched to be 1 if $x_f = 0$. A similar problem occurs if $n_s = 1$; however, this problem is solved by conditioned expression in the fault current's model (Fig. 1.7).

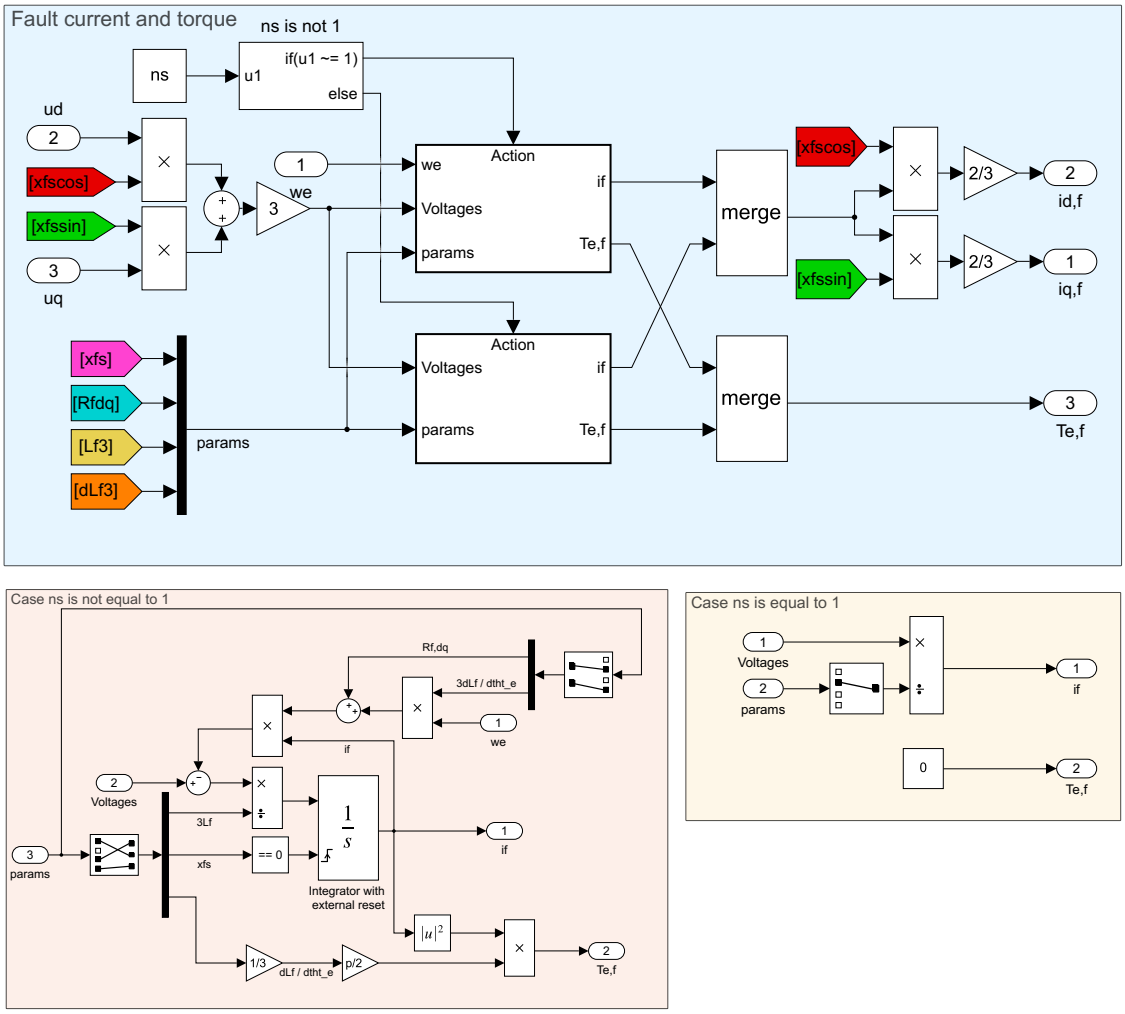

Fig. 1.7: Model of the fault current and torque

If $n_s = 1$, then the fault current i_f is expressed algebraically and modeled as in (1.29). On the other hand, if $n_s \neq 1$, then the fault current satisfies (1.28). Note that if x_f is switched to be 0, the voltage inputs are multiplied by $x_f^* = 0$, and the state of the fault current is forced to be 0 by the external reset of integrator. Hence, the fault current and torque are 0 in this situation and the model acts as a model of healthy IPMSM.

1.5 Model validation

Typically, vector control is used to drive alternate current machines. Vector control embodies a variable-frequency drive control method that employs two closed control loops to regulate the electromagnetic torque and angular velocity. Using the IPMSM in closed control loops is the most natural approach. Such control loops, however, have a significant impact on the machine behavior during a fault. Hence, this thesis provides open-loop validation to ensure that the machine behavior does not depend on the control loop architecture and tuning.

The validation is performed on a configurable motor for the following winding connections: $n_p = 1$ and $n_s = 1$, $n_p = 1$ and $n_s = 3$, $n_p = 2$ and $n_s = 3$. The measured electrical parameters for the different winding connections are presented in the table below:

Tab. 1.2: Electrical parameters of the validated machine

Connection	$n_p = 1;\ n_s = 1$	$n_p = 1;\ n_s = 3$	$n_p = 2;\ n_s = 3$
$R_s\ [m\Omega]$	39.11	112.1	42.68
$L_d\ [\mu H]$	572.0	1751	745.2
$L_q\ [\mu H]$	560.6	1696	699.7
$\lambda_{pm}\ [mWb]$	1.807	5.522	4.998
$R_f\ [m\Omega]$	42.41	45.20	45.38

The machine, driven by a dynamometer to the angular velocity setpoint, is disconnected from the inverter, and the inter-turn short circuits are emulated in the phase 'a' with the local fault relevance $x_f = 6/25$, $x_f = 9/25$, and $x_f = 14/25$ using a relay. The back electromotive force and fault current are measured using an oscilloscope. The fault current, together with the electrical angle, is also acquired by the microcontroller, and both measurements are synchronized based on the fault current waveform. A photo of the testbench utilized in validating the faulty model is displayed in Figure 1.8.

The back electromotive force is transformed from the stator variables (abc) into the rotor reference frame $d-q$ using the information about the electrical angle. The fault current and $d-q$ voltages are then transformed into the frequency domain using the fast Fourier transform. As can be seen in the model from Section 1.3, the ITF causes the fault current with the dominant frequency ω_e, which leads to distortion in the $d-q$ frame mainly on the frequency $2\omega_e$. Hence, the model validation uses the first harmonic of i_f and the second harmonics of the induced u_d and u_q.

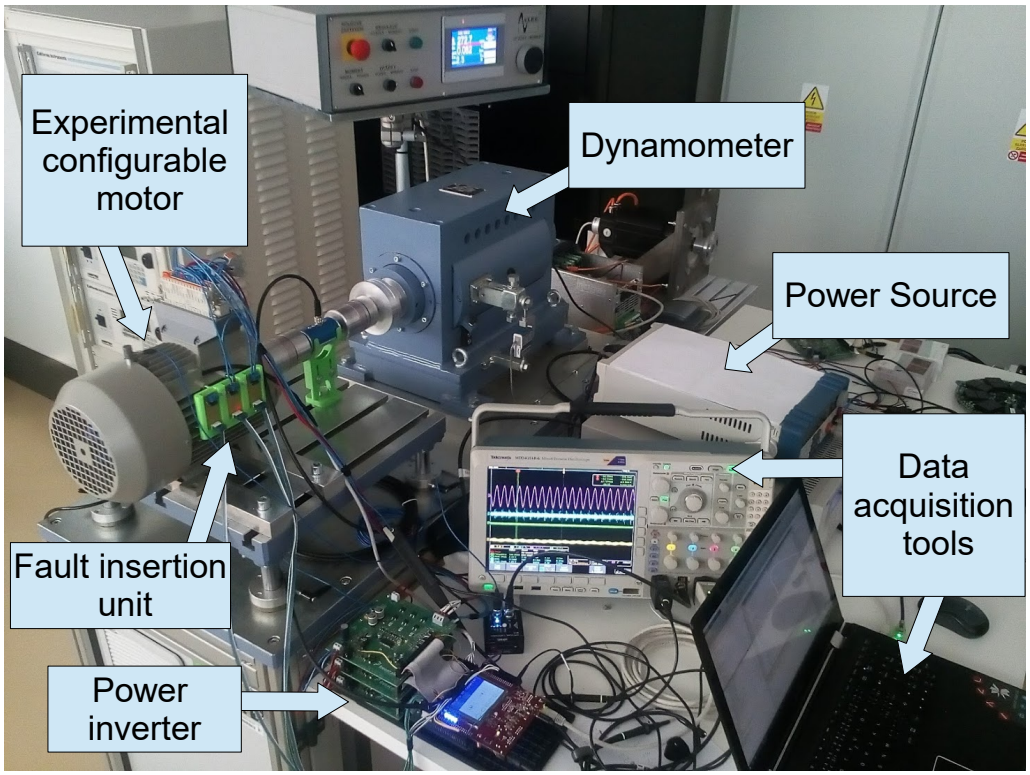

Fig. 1.8: Photo of the testbench

As the machine is disconnected from the inverter, the currents satisfy the conditions $i_a = 0$, $i_b = 0$, and $i_c = 0$, yielding $i_d = 0$ and $i_q = 0$. This condition may be employed to derive a model that considers ω_e as the input and u_d, u_q and i_f as the outputs (Appendix A). The resulting model is then used to simulate the back electromotive force and the fault current during the ITF. The simulated data are processed similarly to the measured waveforms.

Comparing the simulation with the measurement exploits the relative error, calculated as in (1.33) for each measured point of the fault current's first harmonic and the second harmonics of the induced u_d and u_q. We have

$$error = 100 \cdot \left| \frac{measured - simulated}{measured} \right|. \tag{1.33}$$

Relative errors for each examined winding connection are then statistically processed, and the mean value and variance are calculated. These statistics express how precisely the model approximates the measured amplitudes in each measured point.

The comparison of the simulation and the measurement for three motor configurations is visualized in Figure 1.9.

a) winding connection $n_p = 1$; $n_s = 1$

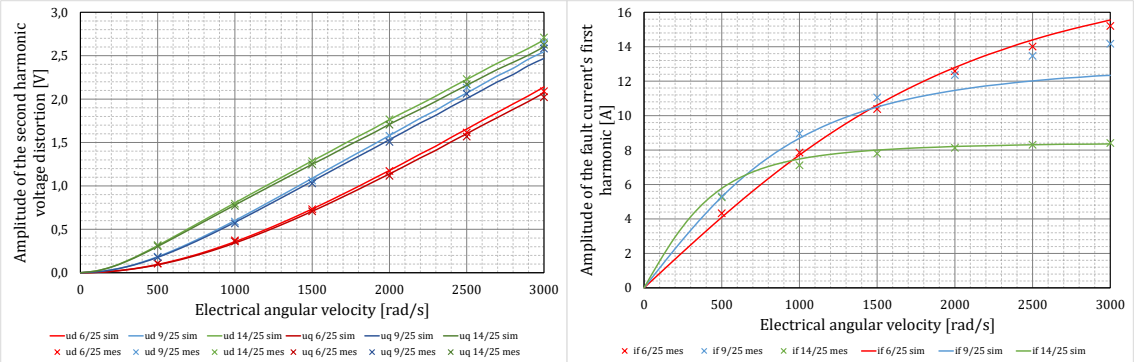

b) winding connection $n_p = 1$; $n_s = 3$

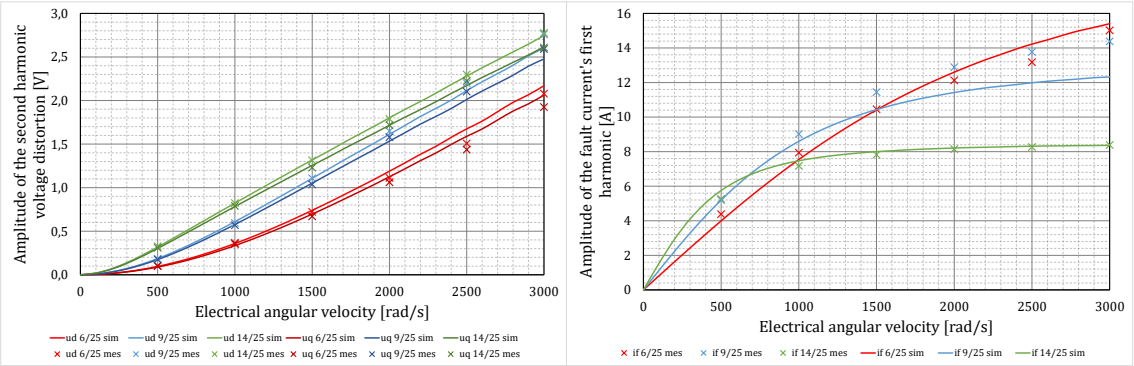

c) winding connection $n_p = 2$; $n_s = 3$

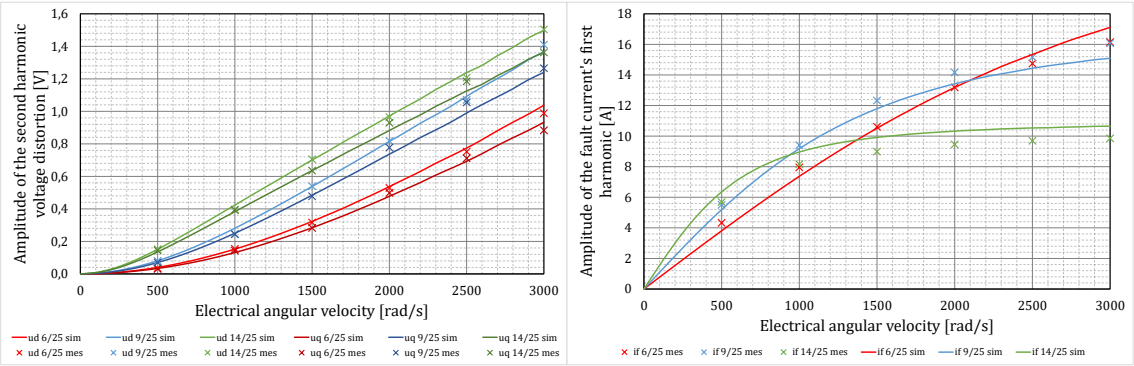

Fig. 1.9: Comparison between the measurement and the simulation

The relative error statistics are presented in the following table:

Tab. 1.3: Calculated relative error statistics

Connection	$n_p = 1$; $n_s = 1$	$n_p = 1$; $n_s = 3$	$n_p = 2$; $n_s = 3$
Mean value [%]	2.9	4.1	4.4
Variance [%]	10.8	13.9	13.7

2 Control system architecture and tuning

This thesis aims for the closed-loop diagnostics of ITF relevance. In this configuration, the state variables are affected by ITF and by control system architecture and tuning. The alternate current machines are commonly controlled in the rotor reference frame, where direct axis current i_d defines the magnetic flux, and quadrature axis current i_q determines the electromagnetic torque T_e. Proportional-integral (PI) controllers are then usually used to keep the current components i_d and i_q at their requested values i_d^* and i_q^*. Due to the nonlinear second harmonic distortion in the rotor reference frame caused by an ITF, the system can become unstable if the current controllers are tuned aggressively, especially at the higher electrical angular velocities ω_e. Hence, robustness is a crucial control system property that has to be maximized.

As seen in the healthy part of IPMSM model (1.25), current components are coupled by terms that depend on the electrical angular velocity ω_e. Generally, if a machine operates in the low-speed region, current controllers compensate couplings between $d-q$ currents without much effort. However, with a growing ω_e, couplings between the current components become dominant and are usually compensated by feedforward compensation techniques. Some of the compensation techniques were presented by Xingye et al. in [16]. Such techniques were derived based on the measurable disturbance compensation approach and ensure a high robustness of the control loop. Figure 2.1 shows a control system architecture with the diagonal compensation decoupling current controllers described in [16].

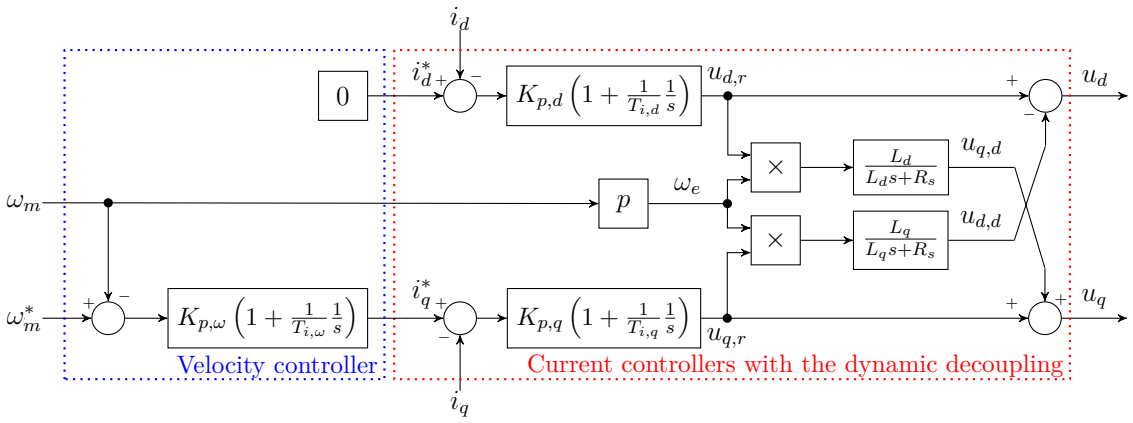

Fig. 2.1: Control system architecture

In Figure 2.1, s is the Laplace operator, $K_{p,d}$, $K_{p,q}$, and $K_{p,\omega}$ stand for proportional gains of PI controllers and $T_{i,d}$, $T_{i,q}$, and $T_{i,\omega}$ are integral time constants of PI controllers.

Due to the position of magnets in IPMSMs, i_d also contributes to the electromagnetic torque and the most efficient combination of currents that provides the required torque can be determined based on the peak torque per amper curve [11]. However, the contribution of i_d to T_e is dependent on the difference between the direct and quadrature axis inductance L_d and L_q, which is neglectable in case of the configurable motor used for experiments (Tab. 1.2). Then it is possible to control the electromagnetic torque using only the quadrature axis current requests i_q^*. Since the flux weakening technique is not implemented in this thesis, the direct axis current setpoint is $i_d^* = 0$. This instantaneous torque control loop, also called the current loop, is extended by a PI controller of mechanical angular velocity ω_m (Fig. 2.1). The control action of this PI controller then defines the requested value of quadrature axis current i_q^* (thus the requested value of electromagnetic torque), enabling us to drive a machine to the angular velocity setpoint ω_m^*.

2.1 Control system parameters tuning

Zezula presented an analytic solution for the parameters tuning of the IPMSM control system that ensures robustness to parameters changes in [17]. The designed parameters read

$$\begin{aligned} K_{p,d} &= C_{cl}\frac{L_d}{T_s} & T_{i,d} &= \frac{L_d}{R_s} \\ K_{p,q} &= C_{cl}\frac{L_q}{T_s} & T_{i,q} &= \frac{L_q}{R_s} \\ K_{p,\omega} &= C_{vl}\frac{20J}{3p\lambda_{pm}T_s} & T_{i,\omega} &= 10\frac{T_s}{C_{cl}} \end{aligned} \tag{2.1}$$

where T_s is the sampling period, $C_{cl} \in \langle 0, \pi/9 \rangle$ stands for the current loop scaling factor tuned based on the possible electrical parameters changes, and C_{vl} represents the velocity loop scaling factor that ensures the phase margin of the velocity loop of at least 46° (traditionally around 55°, depending on C_{cl}). The velocity loop scaling factor C_{vl} can be then analytically expressed out of C_{cl} as in

$$C_{vl} = \frac{\sigma^2\sqrt{C_{cl}^2+\sigma^2}}{C_{cl}\sqrt{C_{cl}^2+100\sigma^2}} \qquad \sigma = \sqrt{\frac{C_{cl}\left(\sqrt{9801C_{cl}^2+14520C_{cl}+3600}-101C_{cl}-60\right)}{200}}. \tag{2.2}$$

However, (2.2) can be approximated on interval $C_{cl} \in \langle 0, \pi/9 \rangle$ using a second-order polynomial with a relative error lower than 1.8 %. We have

$$C_{vl} \approx \frac{1}{32}C_{cl} - \frac{1}{40}C_{cl}^2. \tag{2.3}$$

The current loop scaling factor C_{cl} is then calculated by solving an algebraic stability criterion for different combinations of reachable values of electrical parameters.

This solution provides an optimal design of parameters; however, the calculation of C_{cl} might be complicated if an ITF occurs. As mentioned by Sul in [11], since the dynamics of the current and velocity loop differs, the integral time constant of the PI controllers should be tuned as in

$$T_{i,\omega} \geq 5 \max\left(T_{i,d}, T_{i,q}\right). \tag{2.4}$$

If the integral time constants follow $T_{i,\omega} = 10 \max\left(T_{i,d}, T_{i,q}\right)$ and (2.1) is substituted into (2.4), the current loop scaling factor C_{cl} reads

$$C_{cl} = \frac{T_s R_s}{\max\left(L_d, L_q\right)}. \tag{2.5}$$

Hence, assuming relations (2.3) and (2.5), controllers parameters can be expressed as in

$$\begin{aligned}
K_{p,d} &= \frac{R_s L_d}{\max(L_d, L_q)} & T_{i,d} &= \frac{L_d}{R_s} \\
K_{p,q} &= \frac{R_s L_q}{\max(L_d, L_q)} & T_{i,q} &= \frac{L_q}{R_s} \\
K_{p,\omega} &= \left(\frac{5}{24} - \frac{1}{6}\frac{T_s R_s}{\max(L_d, L_q)}\right) \frac{R_s J}{p\lambda_{pm} \max(L_d, L_q)} & T_{i,\omega} &= 10\frac{\max(L_d, L_q)}{R_s}.
\end{aligned} \tag{2.6}$$

Note that the zeros of PI current controllers are placed to compensate poles in the diagonal decoupling blocks (Fig. 2.1).

Electrical parameters of the examined motor are defined as in Table 1.2, $p = 21$, $J = 0.01 kg{\cdot}m^2$, and $T_s = 100 \mu s$. Calculated controllers parameters are summarized in the following table:

Tab. 2.1: Control system parameters

Connection	$n_p = 1$; $n_s = 1$	$n_p = 1$; $n_s = 3$	$n_p = 2$; $n_s = 3$
$K_{p,d}$ $[-]$	0.0391	0.112	0.0427
$K_{p,q}$ $[-]$	0.0383	0.109	0.0401
$K_{p,\omega}$ $[-]$	3.73	1.14	1.13
$T_{i,d}$ $[s]$	0.0146	0.0156	0.0175
$T_{i,q}$ $[s]$	0.0143	0.0151	0.0164
$T_{i,\omega}$ $[s]$	0.146	0.156	0.175

2.2 Discrete-time equivalent and anti-windup

The exact discretization is highly complicated due to the control system's nonlinear couplings between voltages and electrical angular velocity (Fig. 2.1). However, the mechanical subsystem has significantly slower dynamics than the machine's current loop. Hence, the electrical angular velocity can be considered constant over one sampling period.

In real applications of IPMSM, the mechanical angle $\theta_m(t)$ is sampled with the same sampling period T_s as (abc) currents, and $\theta_e(t)$ is calculated out of $\theta_m(t)$ as in (1.32). This sampling rate is crucial because the information about $\theta_e(t)$ is required in the rotor reference frame transformation. The electrical angular velocity $\omega_e(t)$ is then estimated using an angle tracking observer (ATO). Hence, the sampling rate designed to the current loop's dynamics is highly overrated in a slower mechanical subsystem, and only minor changes of $\omega_e(t)$ occur during one sampling period T_s. The maximum possible change of $\omega_e(t)$ during one sampling period is reached if the maximum electromagnetic torque is generated and minimum torque load and friction torque are connected to a machine's shaft. We have

$$T_{max} = T_{e,max} - T_{fric,min} - T_{load,min}. \tag{2.7}$$

If the minimum values of torque load $T_{load,min}$ and friction torque $T_{fric,min}$ are unknown, they can be considered 0, resulting in $T_{max} = T_{e,max}$. The maximum electromagnetic torque is then given as in $T_{e,max} = \frac{3}{2} p \lambda_{pm} I_{max}$, where I_{max} stands for the current vector limitation. If the maximum torque is generated, the electrical angular velocity $\omega_e(t)$ can be derived out of the motion equation (1.30) as in

$$\frac{\mathrm{d}\omega_e}{\mathrm{d}t} = \frac{p}{J} T_{max} \qquad\qquad \omega_e(k+1) = \omega_e(k) + \frac{p}{J} T_{max} \int_{kT_s}^{(k+1)T_s} \mathrm{d}t \tag{2.8}$$

where k is the actual step of the discretized system. The maximum possible change $\Delta_{\omega_e,max}$ of $\omega_e(t)$ during one sampling period reads

$$\Delta_{\omega_e,max} = \frac{p}{J} T_{max} T_s = \frac{3p^2 \lambda_{pm} I_{max} T_s}{2J}. \tag{2.9}$$

If the current limitation of the examined motor is $I_{max} = 8\,A$, then the maximum torque $T_{max} = T_{e,max}$ and $\Delta_{\omega_e,max}$ are calculated in the following table:

Tab. 2.2: The maximum possible changes of electrical angular velocity

Connection	$n_p = 1;\ n_s = 1$	$n_p = 1;\ n_s = 3$	$n_p = 2;\ n_s = 3$
$T_{max}\ [Nm]$	0.455	1.392	1.260
$\Delta_{\omega_e,max}\ [rad/s]$	0.0956	0.2922	0.2645

Since the maximum possible changes of $\omega_e(t)$ during one sampling period are very low (even if the minimum torque load and friction are neglected), the electrical angular velocity $\omega_e(t)$ can be represented on the interval $kT_s \leq t < (k+1)T_s$ by a constant value estimated by an angle tracking observer. Error caused by this simplification is irrelevant compared to system noise and error of ATO. The control system can be then discretized as a linear time-invariant system.

Based on the parameters tuning (2.6) and the constant electrical angular velocity over one sampling period assumption, the control system (Fig. 2.1) can be written in Laplace transform as in

$$\begin{bmatrix} U_d(s) \\ U_q(s) \end{bmatrix} = \begin{bmatrix} -K_{p,d}\left(1+\frac{1}{T_{i,d}}\frac{1}{s}\right) & -\frac{K_{p,d}\omega_e}{s} \\ \frac{K_{p,q}\omega_e}{s} & -K_{p,q}\left(1+\frac{1}{T_{i,q}}\frac{1}{s}\right) \\ -\frac{K_{p,\omega}K_{p,q}\omega_e}{s}\left(1+\frac{1}{T_{i,\omega}}\frac{1}{s}\right) & K_{p,\omega}K_{p,q}\left(1+\frac{1}{T_{i,q}}\frac{1}{s}\right)\left(1+\frac{1}{T_{i,\omega}}\frac{1}{s}\right) \end{bmatrix}^T \cdot \begin{bmatrix} I_d(s) \\ I_q(s) \\ E_\omega(s) \end{bmatrix} \tag{2.10}$$

where $E_\omega(s) = \Omega_m^*(s) - \Omega_m(s)$. Hence, the continuous-time multiple-input multiple-output system (2.10) can be discretized using the zero-order hold. We have

$$\begin{bmatrix} U_d(z) \\ U_q(z) \end{bmatrix} = \begin{bmatrix} -K_{p,d}\left(1+\frac{T_s}{T_{i,d}}\frac{z^{-1}}{1-z^{-1}}\right) & \omega_e T_{i,q}\left(K_{p,q}\frac{T_s}{T_{i,q}}\frac{z^{-1}}{1-z^{-1}}\right) & F_{13}(z) \\ -\omega_e T_{i,d}\left(K_{p,d}\frac{T_s}{T_{i,d}}\frac{z^{-1}}{1-z^{-1}}\right) & -K_{p,q}\left(1+\frac{T_s}{T_{i,q}}\frac{z^{-1}}{1-z^{-1}}\right) & F_{23}(z) \end{bmatrix} \cdot \begin{bmatrix} I_d(z) \\ I_q(z) \\ E_\omega(z) \end{bmatrix} \tag{2.11}$$

where z is the Z-transform operator and

$$\begin{aligned} F_{13}(z) &= -K_{p,\omega}\left(1+\frac{T_s}{2T_{i,\omega}}+\frac{T_s}{T_{i,\omega}}\frac{z^{-1}}{1-z^{-1}}\right)\omega_e T_{i,q}\left(K_{p,q}\frac{T_s}{T_{i,q}}\frac{z^{-1}}{1-z^{-1}}\right) \\ F_{23}(z) &= K_{p,\omega}K_{p,q}\left(1+\left(\frac{T_s}{T_{i,\omega}}+\frac{T_s}{T_{i,q}}+\frac{T_s^2}{2T_{i,\omega}T_{i,q}}\right)\frac{z^{-1}}{1-z^{-1}}+\frac{T_s^2}{T_{i,\omega}T_{i,q}}\frac{z^{-2}}{(1-z^{-1})^2}\right). \end{aligned} \tag{2.12}$$

However, since $1 \gg \frac{T_s}{2T_{i,\omega}}$, $\frac{T_s}{T_{i,q}} \gg \frac{T_s^2}{2T_{i,\omega}T_{i,q}}$, and $\frac{T_s}{T_{i,\omega}} \gg \frac{T_s^2}{2T_{i,\omega}T_{i,q}}$, the transfer functions (2.12) can be approximated as in

$$\begin{aligned} F_{13}(z) &\approx -K_{p,\omega}\left(1+\frac{T_s}{T_{i,\omega}}\frac{z^{-1}}{1-z^{-1}}\right)\omega_e T_{i,q}\left(K_{p,q}\frac{T_s}{T_{i,q}}\frac{z^{-1}}{1-z^{-1}}\right) \\ F_{23}(z) &\approx K_{p,\omega}\left(1+\frac{T_s}{T_{i,\omega}}\frac{z^{-1}}{1-z^{-1}}\right)K_{p,q}\left(1+\frac{T_s}{T_{i,q}}\frac{z^{-1}}{1-z^{-1}}\right) \end{aligned} \tag{2.13}$$

Hence, the velocity and current controllers can be separated.

A straightforward anti-windup technique can be used in the velocity controller since the current limitation I_{max} is usually constant for a particular machine. Therefore, the well-known clamping anti-windup method is implemented. This technique reads that if $|i_q^*| > I_{max}$, then $|i_q^*|$ is limited to I_{max}, and $T_s/T_{i,\omega} = 0$. Due to this

conditioning, an integrator is turned off if the limit value is reached. If the limitation is static, this method prevents accumulating energy in the integrator. Figure 2.2 shows the MATLAB Simulink realization of the velocity controller with the clamping anti-windup.

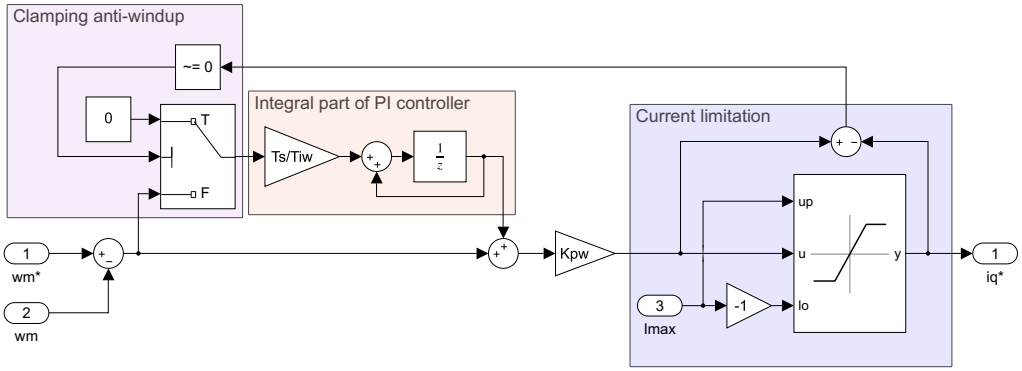

Fig. 2.2: Velocity controller with the clamping anti-windup

In Figure 2.2 the current limitation I_{max} is represented by an input signal even though it is a constant value. This enables us to change the value of this parameter inside the processor without repetitive code generating.

In the current controllers, the output voltages are limited based on an inverter's DC bus voltage U_{dc}. However, U_{dc} represents a voltage limitation in the stator variables (abc) and is transformed into $d-q$ frame as in $U_{max} = U_{dc}/\sqrt{3}$. Then U_{max} is a voltage limitation in the rotor reference frame. Direct and quadrature axis voltage components are then limited as $|u_d| \leq U_{max}$ and $|u_q| \leq \sqrt{U_{max}^2 - u_d^2}$. Figure 2.3 shows the MATLAB Simulink realization of the current controllers (2.11) with the voltage limitation.

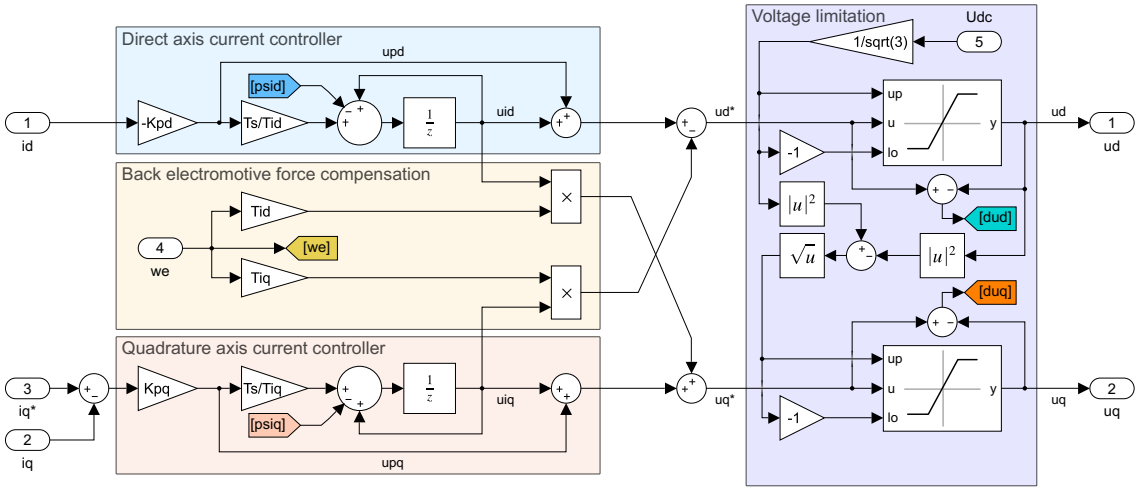

Fig. 2.3: Current controllers

The clamping anti-windup method cannot be sufficiently implemented in current controllers since the limitation of voltage components change dynamically (especially the limitation of quadrature axis voltage). Due to this issue, the back-calculation anti-windup method is derived and implemented.

If the voltages are saturated, differences $\Delta_{u,d}$ and $\Delta_{u,q}$ between required voltage outputs u_d^* and u_q^* and real voltage outputs u_d and u_q occur. We have

$$\begin{bmatrix} u_d^* \\ u_q^* \end{bmatrix} - \begin{bmatrix} u_d \\ u_q \end{bmatrix} = \begin{bmatrix} \Delta_{u,d} \\ \Delta_{u,q} \end{bmatrix} \tag{2.14}$$

where

$$\begin{bmatrix} u_d^* \\ u_q^* \end{bmatrix} = \begin{bmatrix} u_{p,d} \\ u_{p,q} \end{bmatrix} + \begin{bmatrix} 1 & -T_{i,q}\omega_e \\ T_{i,d}\omega_e & 1 \end{bmatrix} \cdot \begin{bmatrix} u_{i,d} \\ u_{i,q} \end{bmatrix}. \tag{2.15}$$

Voltage signals $u_{p,d}$ and $u_{p,q}$ stand for the proportional contributions of PI controllers, and $u_{i,d}$ and $u_{i,q}$ represent outputs of integral parts (Fig. 2.3). Voltages of integral parts should then be compensated to satisfy zero difference conditions as in

$$\begin{bmatrix} u_{d,c}^* \\ u_{q,c}^* \end{bmatrix} - \begin{bmatrix} u_d \\ u_q \end{bmatrix} = \begin{bmatrix} 0 \\ 0 \end{bmatrix} \tag{2.16}$$

where

$$\begin{bmatrix} u_{d,c}^* \\ u_{q,c}^* \end{bmatrix} = \begin{bmatrix} u_{p,d} \\ u_{p,q} \end{bmatrix} + \begin{bmatrix} 1 & -T_{i,q}\omega_e \\ T_{i,d}\omega_e & 1 \end{bmatrix} \cdot \begin{bmatrix} u_{i,d} - \psi_d \\ u_{i,q} - \psi_q \end{bmatrix}. \tag{2.17}$$

Comparing (2.14) and (2.16) and removing the algebraic loop by inserting the unit delay block provides the solution of compensating voltages ψ_d and ψ_q as in

$$\begin{bmatrix} \psi_d(k+1) \\ \psi_q(k+1) \end{bmatrix} = \frac{1}{1 + T_{i,d}T_{i,q}\omega_e(k)^2} \begin{bmatrix} 1 & T_{i,q}\omega_e(k) \\ -T_{i,d}\omega_e(k) & 1 \end{bmatrix} \cdot \begin{bmatrix} \Delta_{u,d}(k) \\ \Delta_{u,q}(k) \end{bmatrix}. \tag{2.18}$$

The back-calculation anti-windup of current controllers is shown in Figure 2.4.

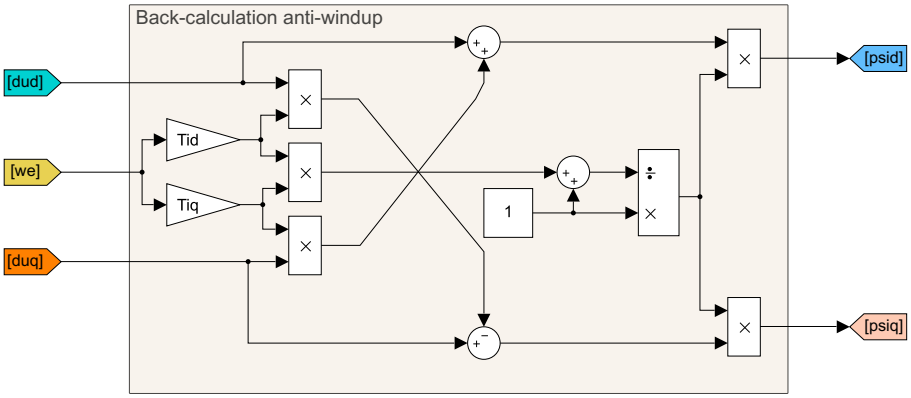

Fig. 2.4: Back-calculation anti-windup of current controllers

2.3 Angle tracking observer

Angle tracking observer embodies a phase-locked loop that minimizes the difference between an estimated angle and an angle read from measured signals. ATO in the base form comprises a phase detector that calculates an error $\tilde{\theta}_e$ between the estimated and the actual position, a PI controller that compensates the error, and an integrator that integrates the control action of the PI controller [18]. The control action of the PI controller then represents an estimated angular velocity $\hat{\omega}_e$, and the estimated angle $\hat{\theta}_e$ is obtained by integrating the estimated velocity. This connection is widely used; however, when a motor speeds up at a constant acceleration, the conventional ATO causes a steady-state error in its estimated position. This problem was solved by Wang et al. in [19] by involving a first-order compensation module that utilizes the estimated speed to generate a signal proportional to the motor's acceleration, thus compensating the position error if $\theta_e = ct^2$. If there is a demand for higher-order position changes $\theta_e = ct^3$, the higher-order compensation module has to be implemented to compensate for the error appropriately. In this thesis; however, a conventional ATO is implemented since the steady-state angle error is neglectable for the calculated frequency bandwidth of the examined machine.

The angle tracking observer in the base form is visualized in Figure 2.5.

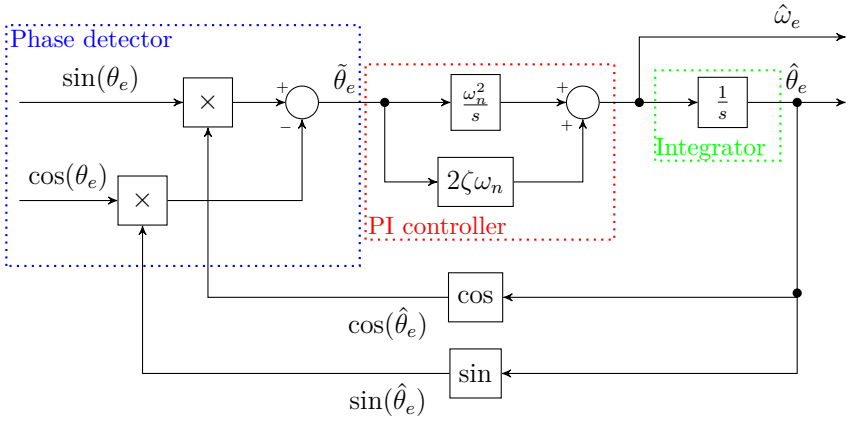

Fig. 2.5: Angle tracking observer

In Figure 2.5, ζ stands for a damping ratio, and ω_n is a natural frequency of ATO tuned based on the frequency bandwidth $\omega_n = \omega_b/2$. As mentioned by Sul in [11], since the direct axis current i_d is controlled to zero, the frequency bandwidth ω_b of IPMSM is calculated based on the voltage and current limitation $U_{max} = U_{dc}/\sqrt{3}$ and I_{max} as in

$$\omega_b = \frac{U_{dc}}{\sqrt{3\left(\lambda_{pm}^2 + L_q^2 I_{max}^2\right)}}. \tag{2.19}$$

The frequency bandwidths of the examined machine are then presented in the following table for three winding connections:

Tab. 2.3: Frequency bandwidths of the examined machine

Connection	$n_p = 1;\ n_s = 1$	$n_p = 1;\ n_s = 3$	$n_p = 2;\ n_s = 3$
$U_{dc}\ [V]$	55/3	55	55
$\omega_b\ [rad/s]$	2189	2168	4232

The estimated angle $\hat{\theta}_e$ tracks the actual one θ_e, and the difference between angles $\tilde{\theta}_e$ tends to zero. Hence, the system (Fig. 2.5) can be linearized using the small-angle approximation. We have

$$\tilde{\theta}_e = \sin(\theta_e)\cos(\hat{\theta}_e) - \cos(\theta_e)\sin(\hat{\theta}_e) = \sin(\theta_e - \hat{\theta}_e) \approx \theta_e - \hat{\theta}_e. \tag{2.20}$$

The angle-tracking transfer function of the linearized system is then expressed as in

$$\frac{\hat{\Theta}_e(s)}{\Theta_e(s)} = \frac{2\zeta\omega_n s + \omega_n^2}{s^2 + 2\zeta\omega_n s + \omega_n^2}. \tag{2.21}$$

For the second-order system (2.21) to achieve the tradeoff between responsiveness and overshoot, it is common practice to set ζ as $\sqrt{2}/2$. The estimated velocity $\hat{\omega}_e$ can be then expressed as the first derivative of the estimated angle $\hat{\theta}_e$. We have

$$\hat{\Omega}_e(s) = s\hat{\Theta}_e(s) \qquad \frac{\hat{\Omega}_e(s)}{\Theta_e(s)} = \frac{2\zeta\omega_n s^2 + \omega_n^2 s}{s^2 + 2\zeta\omega_n s + \omega_n^2}. \tag{2.22}$$

The designed ATO is implemented as a part of the control system in a discrete form. Hence, the discrete-time equivalents of transfer functions (2.21) and (2.22) must be calculated, and open-loop transfer functions $\frac{\hat{\Theta}_e(z)}{\hat{\Omega}_e(z)}$ and $\frac{\hat{\Omega}_e(z)}{\hat{\Theta}_e(z)}$ have to be expressed to preserve the phase detector part of ATO. If a machine runs at the constant angular velocity, the electrical angle satisfies $\theta_e(t) = ct$. On the other hand, if a motor runs at a constant acceleration, the electrical angle meets $\theta_e(t) = ct^2$. Hence, these two (or most likely more) representations of $\theta_e(t)$ have to be taken into account in the discretization procedure. Then the piecewise linear approximation of $\theta_e(t)$ is applied to preserve the simplicity of the discrete-time equivalents, yielding

$$\theta_e(t) = \theta_e(k) + \frac{t - kT_s}{T_s}(\theta_e(k+1) - \theta_e(k)) \qquad kT_s \le t < (k+1)T_s. \tag{2.23}$$

Note that approximation (2.23) provides an exact solution if $\theta_e(t) = ct$. The discrete-time equivalents are then calculated as in

$$\frac{\hat{\Theta}_e(z)}{\Theta_e(z)} = \frac{(z-1)^2}{T_s z} Z_{ekv}\left\{\frac{1}{s^2}\frac{\hat{\Theta}_e(s)}{\Theta_e(s)}\right\} \qquad \frac{\hat{\Omega}_e(z)}{\Theta_e(z)} = \frac{(z-1)^2}{T_s z} Z_{ekv}\left\{\frac{1}{s}\frac{\hat{\Theta}_e(s)}{\Theta_e(s)}\right\} \tag{2.24}$$

where $Z_{ekv}\{F(s)\}$ represents the Z-transform equivalent of a transmission defined in the Laplace transform. The open-loop transfer functions are then derived using the angle error definition $\tilde{\Theta}_e(z) = \Theta_e(z) - z^{-1}\hat{\Theta}_e(z)$ (this definition prevents an algebraic loop occurrence) as follows:

$$\frac{\hat{\Theta}_e(z)}{\hat{\Omega}_e(z)} = \frac{\hat{\Theta}_e(z)}{\Theta_e(z)}\left(\frac{\hat{\Omega}_e(z)}{\Theta_e(z)}\right)^{-1} \qquad \frac{\hat{\Omega}_e(z)}{\tilde{\Theta}_e(z)} = \frac{\hat{\Omega}_e(z)}{\Theta_e(z)}\left(1 - z^{-1}\frac{\hat{\Theta}_e(z)}{\Theta_e(z)}\right)^{-1}. \tag{2.25}$$

Listing 2.1 presents the discretization procedure realized in MATLAB.

Listing 2.1: Discretization of ATO in MATLAB

```
wn = 2189/2; zeta = sqrt(2)/2; Ts = 100e-6;
F_tht = tf([2*zeta*wn,wn^2],[1,2*zeta*wn,wn^2]);
F_omg = tf([2*zeta*wn,wn^2,0],[1,2*zeta*wn,wn^2]);
F_tht = zpk(c2d(F_tht,Ts,'foh'));
F_omg = zpk(c2d(F_omg,Ts,'foh'));
F0_omg = tf(minreal(F_omg/zpk(1-F_tht/tf('z')),1e-4))
F0_tht = minreal(F_tht/F_omg,1e-4);
% Separating feedforward coupling
[num_tht,den_tht] = tfdata(F0_tht,'v');
[~,~,K_tht] = residue(num_tht,den_tht)
F0_tht_c = tf(F0_tht - K_tht)
```

The resulting discrete-time equivalents are described as in

$$\frac{\hat{\Theta}_e(z)}{\hat{\Omega}_e(z)} = K_\theta + T_s\frac{z^{-1}}{1 - z^{-1}} \qquad \frac{\hat{\Omega}_e(z)}{\tilde{\Theta}_e(z)} = \frac{b_1 - b_0 z^{-1}}{1 - a_1 z^{-1} - a_0 z^{-2}} \tag{2.26}$$

where the parameters calculated for three winding connections are presented in the following table:

Tab. 2.4: Discretized ATO's parameters

Connection	$n_p = 1;\ n_s = 1$	$n_p = 1;\ n_s = 3$	$n_p = 2;\ n_s = 3$
K_θ	$5.067 \cdot 10^{-5}$	$5.066 \cdot 10^{-5}$	$5.134 \cdot 10^{-5}$
b_1	1488	1474	2769
b_0	1377	1365	2384
a_1	0.9209	0.9217	0.8450
a_0	0.0680	0.0674	0.1164

Figure 2.6 shows the MATLAB Simulink implementation of the designed angle tracking observer.

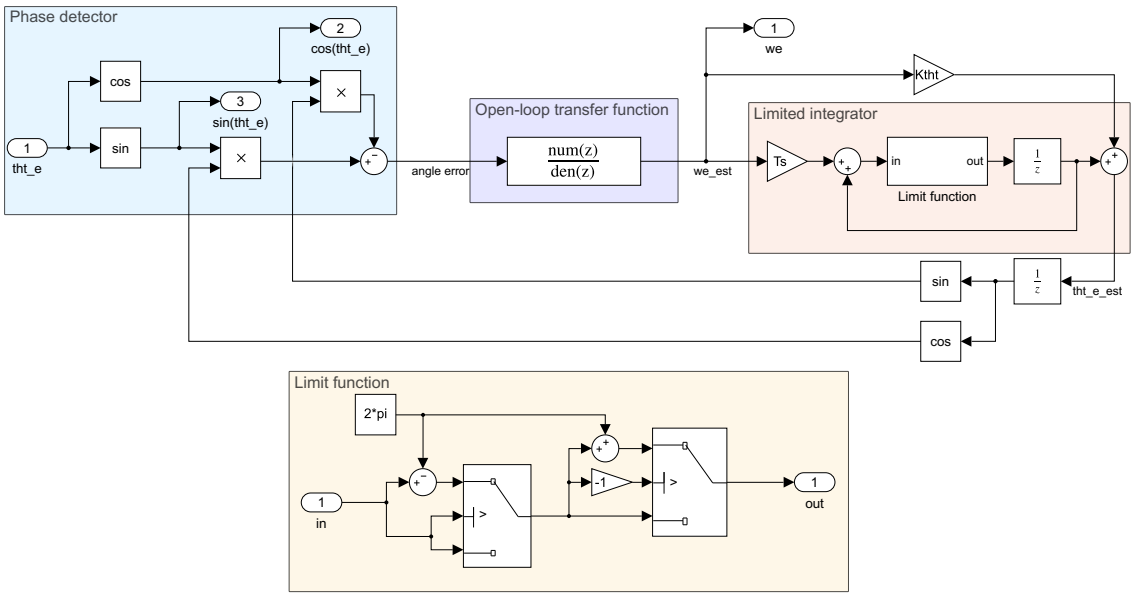

Fig. 2.6: Implementation of the designed angle tracking observer

In Figure 2.6, the limit function is implemented into the discretized integrator to prevent overwhelming the estimated angle. This function ensures that if the input angle θ_{in} is higher than $+\pi$, the output angle θ_{out} value is given by $\theta_{out} = \theta_{in} - 2\pi$. On the other hand, if $\theta_{in} < -\pi$, then $\theta_{out} = \theta_{in} + 2\pi$.

2.4 Transformations and space vector modulation

Since the control system is tuned in the rotor reference frame, the currents measured in the stator variables have to be appropriately transformed. For this purpose, Park's and Clarke's transformation is employed. We have

$$\begin{bmatrix} i_d(k) \\ i_q(k) \end{bmatrix} = \frac{2}{3} \begin{bmatrix} \cos(\theta_e(k)) & \sin(\theta_e(k)) \\ -\sin(\theta_e(k)) & \cos(\theta_e(k)) \end{bmatrix} \cdot \begin{bmatrix} 1 & -\frac{1}{2} & -\frac{1}{2} \\ 0 & \frac{\sqrt{3}}{2} & -\frac{\sqrt{3}}{2} \end{bmatrix} \cdot \begin{bmatrix} i_a(k) \\ i_b(k) \\ i_c(k) \end{bmatrix}. \tag{2.27}$$

Similarly, the voltage requests calculated in the rotor reference frame have to be transformed into the stator variables using inverse Park's and Clarke's transformation. However, due to the calculation time of the discretized control algorithm, a unit delay occurs in the control loop. Hence, the control system does not compute voltage requests for the actual step k but calculates it for the following step $k+1$. In this case, the electrical angle θ_e applied in the transformation matrix has to be evaluated for step $k+1$. The value $\theta_e(k+1)$ can be calculated assuming the constant electrical angular velocity over one sampling period as in

$$\theta_e(k+1) \approx \theta_e(k) + T_s\omega_e(k). \tag{2.28}$$

Voltage requests in the stator variables are then expressed using the angle sum trigonometric identities and inverse transformation matrices. We have

$$\begin{bmatrix} u_a(k+1) \\ u_b(k+1) \\ u_c(k+1) \end{bmatrix} = \begin{bmatrix} 1 & 0 \\ -\frac{1}{2} & \frac{\sqrt{3}}{2} \\ -\frac{1}{2} & -\frac{\sqrt{3}}{2} \end{bmatrix} \cdot \begin{bmatrix} \cos(\theta_e(k)) & -\sin(\theta_e(k)) \\ \sin(\theta_e(k)) & \cos(\theta_e(k)) \end{bmatrix} \cdot \begin{bmatrix} \cos(T_s\omega_e(k)) & -\sin(T_s\omega_e(k)) \\ \sin(T_s\omega_e(k)) & \cos(T_s\omega_e(k)) \end{bmatrix} \cdot \begin{bmatrix} u_d(k+1) \\ u_q(k+1) \end{bmatrix}. \tag{2.29}$$

Alternating voltage waveforms required to drive PMSMs are then commonly generated using the three-phase power inverter with the pulse width modulation. In the basic form, the three-phase power inverter consists of six switches that enable connecting the DC bus voltage between the particular machine phases at a certain moment. These switches are then controlled by logical signals with changeable duty cycles $\delta_a(k)$, $\delta_b(k)$, and $\delta_c(k)$ that are adjusted based on the generated control system voltage requests $u_a(k)$, $u_b(k)$, and $u_c(k)$ and implemented modulation technique. The main objective of the modulation technique is to maximize the utilization of limited DC bus voltage. In this thesis, the Min-Max third harmonics injection approach [20] is implemented as an equivalent of the space vector modulation (SVM) technique. According to the Min-Max modulation strategy, the duty cycles of the inverter's switches are calculated as in

$$\begin{aligned} \delta_a(k) &= \frac{1}{2} + \frac{u_a(k)}{U_{dc}} - \frac{\max(u_a(k), u_b(k), u_c(k)) + \min(u_a(k), u_b(k), u_c(k))}{2U_{dc}} \\ \delta_b(k) &= \frac{1}{2} + \frac{u_b(k)}{U_{dc}} - \frac{\max(u_a(k), u_b(k), u_c(k)) + \min(u_a(k), u_b(k), u_c(k))}{2U_{dc}} \\ \delta_c(k) &= \frac{1}{2} + \frac{u_c(k)}{U_{dc}} - \frac{\max(u_a(k), u_b(k), u_c(k)) + \min(u_a(k), u_b(k), u_c(k))}{2U_{dc}}. \end{aligned} \tag{2.30}$$

The control system implementation is visualized in Figure 2.7.

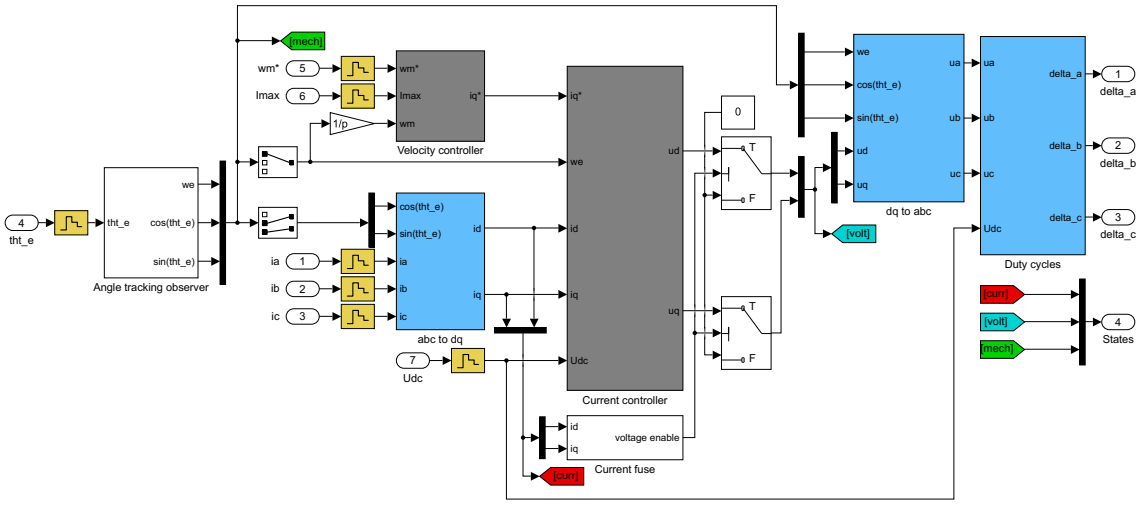

Fig. 2.7: Control system implementation in MATLAB Simulink

In Figure 2.7, a current fuse is implemented. This fuse ensures that the voltage outputs u_d and u_q are disconnected until the control system is restarted if the current vector magnitude $\sqrt{i_d^2 + i_q^2}$ reaches the defined critical value I_{crit}.

2.5 Control system validation

For the purpose of control system validation, a measurement on the configurable motor was performed. A C code was generated using the Embedded Coder app out of the MATLAB Simulink control system model, and the generated code was implemented into preprogrammed AURIX Application Kit TC277. The kit was connected to the inverter, the DC bus voltage was adjusted to $U_{dc} = 45\,V$, and the quadrature axis current request limitation was set to be $I_{max} = 5\,A$. The critical value of the current vector was defined by $I_{crit} = 20\,A$. The angular velocity was then controlled by a slow ramp to $w_m = 10\,rad/s$ to ensure proper initialization.

After the initialization, the step requests of angular velocity were performed, and the transients were measured. Subsequently, inter-turn short circuits were emulated in phase 'a' with fault relevance $x_f = 6/25$ for connection $n_p = 1$, $n_s = 1$, and $x_f = 14/25$ for connections $n_p = 1$, $n_s = 3$ and $n_p = 2$, $n_s = 3$. In configuration $n_p = 1$ and $n_s = 1$, the fault current quickly reaches higher values; therefore, faults with lesser relevance are emulated to prevent overheating. Figure 2.8 visualize measured characteristics for three winding connections.

a) winding connection $n_p = 1$; $n_s = 1$

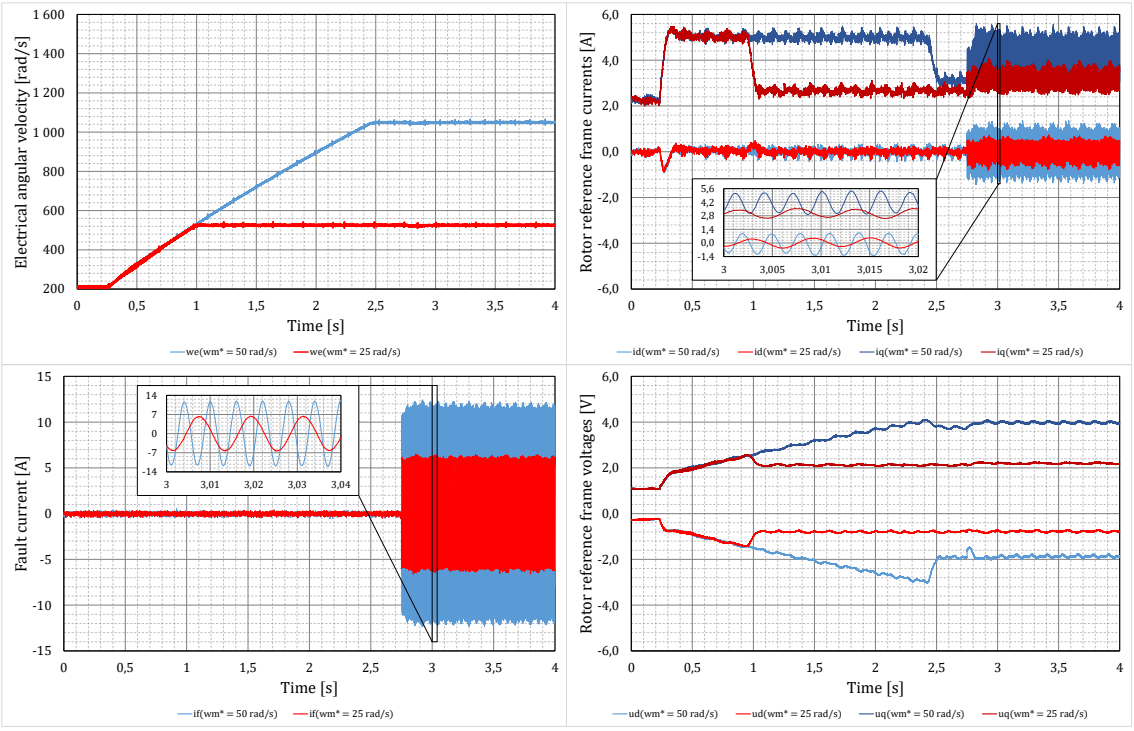

b) winding connection $n_p = 1$; $n_s = 3$

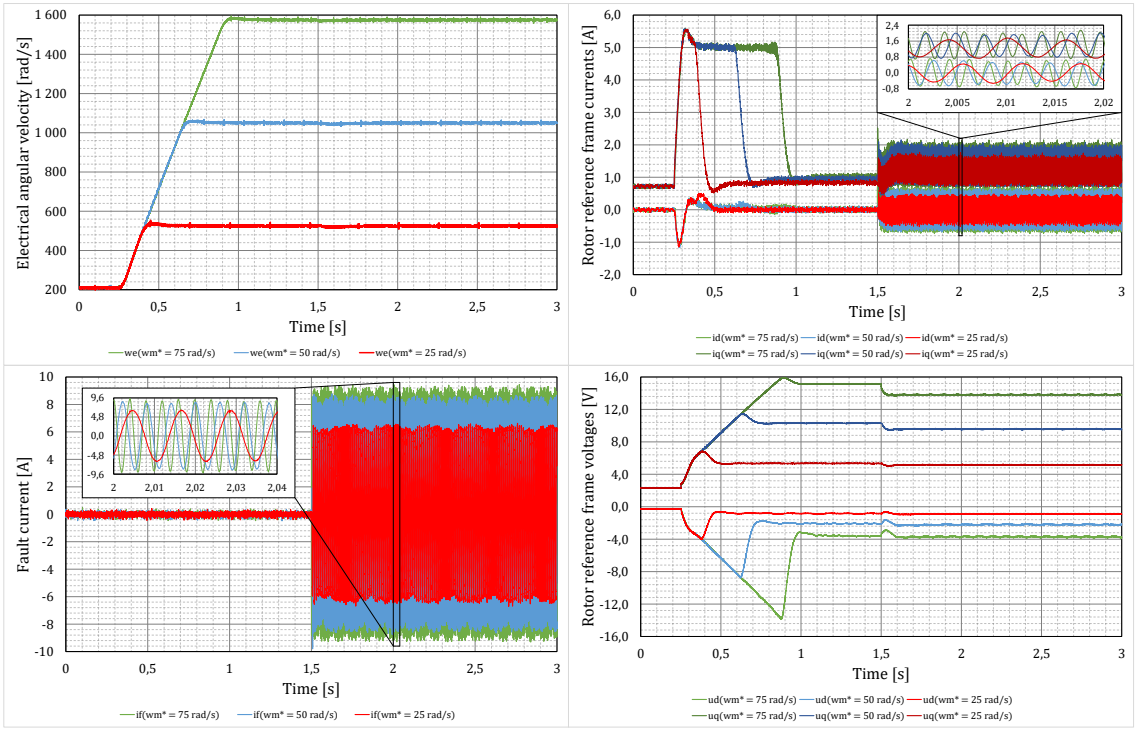

c) winding connection $n_p = 2$; $n_s = 3$

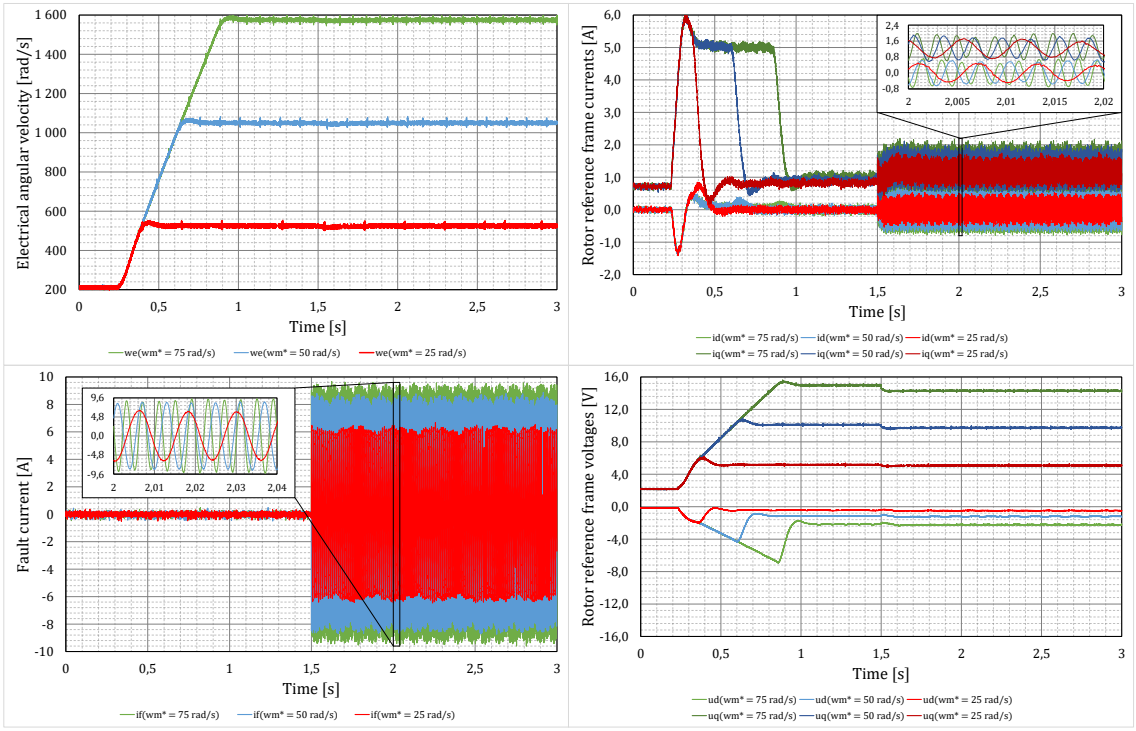

Fig. 2.8: Responses of controlled machine for three winding connections

3 Discrete-time equivalent of ITF model

Since identification algorithms primarily support discrete-time models, therefore, for the purpose of fault relevance diagnostics, the model described in Section 1.3 has to be discretized. Traditionally, many authors discretize machine models using the Finite difference method, such as the forward Euler method (first-order) or the second-order Runge–Kutta method [21] - [22]. These methods approximate a time derivative by the finite set of differences, leading to an inexact solution lacking physical meaning and amplifying the higher frequencies of system noise. Furthermore, this solution might be even unstable at higher electrical angular velocities. Due to these issues, a novel machine discretization procedure based on the linear time-varying systems approach [23] - [24] is presented. The key idea lies in the integral relationship between the electrical angular velocity and angle $\theta_e(t) = \int_{kT_s}^{t} \omega_e(\tau)d\tau + \theta_e(k)$. Hence, in the discretization procedure, the electrical angular velocity $\omega_e(t)$ can be considered a time-varying parameter with the defined integral. Since the model of the shorted machine consists of two parts tied in the output equation, it is possible to discretize these parts separately and combine their discrete-time equivalents.

3.1 Healthy part discretization

The system of differential equations describes the healthy part of the ITF model as in (1.25). This system can be written in a linear time-varying form. We have

$$\frac{\mathrm{d}}{\mathrm{d}t}\begin{bmatrix} i_{d,h}(t) \\ i_{q,h}(t) \end{bmatrix} = \mathbf{A}_h(t)\begin{bmatrix} i_{d,h}(t) \\ i_{q,h}(t) \end{bmatrix} + \mathbf{B}_h(t)\begin{bmatrix} u_d(t) \\ u_q(t) \\ \lambda_{pm} \end{bmatrix} \tag{3.1}$$

where

$$\mathbf{A}_h(t) = \begin{bmatrix} -\frac{R_s}{L_d} & \frac{L_q}{L_d}\omega_e(t) \\ -\frac{L_d}{L_q}\omega_e(t) & -\frac{R_s}{L_q} \end{bmatrix} \qquad \mathbf{B}_h(t) = \begin{bmatrix} \frac{1}{L_d} & 0 & 0 \\ 0 & \frac{1}{L_q} & -\frac{1}{L_q}\omega_e(t) \end{bmatrix}. \tag{3.2}$$

However, since the direct and quadrature axis inductances of the validated machine (Table 1.2) are close to each other, they can be approximated by a common $d-q$ inductance $L_{dq} = \frac{L_d+L_q}{2}$, yielding

$$\mathbf{A}_h(t) \approx \begin{bmatrix} -\frac{R_s}{L_{dq}} & \omega_e(t) \\ -\omega_e(t) & -\frac{R_s}{L_{dq}} \end{bmatrix} \qquad \mathbf{B}_h(t) \approx \frac{1}{L_{dq}}\begin{bmatrix} 1 & 0 & 0 \\ 0 & 1 & -\omega_e(t) \end{bmatrix}. \tag{3.3}$$

Discrete-time equivalent's state matrix $\mathbf{A}_{d,h}((k+1)T_s, kT_s) = e^{\int_{kT_s}^{(k+1)T_s} \mathbf{A}_h(\tau)d\tau}$ is then calculated based on the state matrix $\mathbf{A}_h(t)$ time integral. We have

$$\int_{kT_s}^{(k+1)T_s} \mathbf{A}_h(\tau)d\tau = \begin{bmatrix} -\frac{R_s}{L_{dq}}T_s & (\theta_e(k+1) - \theta_e(k)) \\ -(\theta_e(k+1) - \theta_e(k)) & -\frac{R_s}{L_{dq}}T_s \end{bmatrix}. \tag{3.4}$$

Based on the matrix exponential definition for some special cases of matrix $\mathbf{A}_h(t)$ described by Bernstein and So in [25], the discrete-time equivalent's state matrix $\mathbf{A}_{d,h}((k+1)T_s, kT_s)$ gains the following form:

$$\mathbf{A}_{d,h}((k+1)T_s, kT_s) = e^{-\frac{R_s}{L_{dq}}T_s} \begin{bmatrix} \cos(\theta_e(k+1) - \theta_e(k)) & \sin(\theta_e(k+1) - \theta_e(k)) \\ -\sin(\theta_e(k+1) - \theta_e(k)) & \cos(\theta_e(k+1) - \theta_e(k)) \end{bmatrix}. \tag{3.5}$$

Hence, the discrete-time equivalent of system (3.1) is defined as in

$$\begin{bmatrix} i_{d,h}(k+1) \\ i_{q,h}(k+1) \end{bmatrix} = \mathbf{A}_{d,h}((k+1)T_s, kT_s) \begin{bmatrix} i_{d,h}(k) \\ i_{q,h}(k) \end{bmatrix} + \int_{kT_s}^{(k+1)T_s} \mathbf{A}_{d,h}((k+1)T_s, \tau)\mathbf{B}_h(\tau) \begin{bmatrix} u_d(\tau) \\ u_q(\tau) \\ \lambda_{pm} \end{bmatrix} d\tau. \tag{3.6}$$

However, system (3.6) can be expressed more illustratively in the stator reference frame. We have

$$\begin{bmatrix} i_{\alpha,h}(k+1) \\ i_{\beta,h}(k+1) \end{bmatrix} = e^{-\frac{R_s}{L_{dq}}T_s} \begin{bmatrix} i_{\alpha,h}(k) \\ i_{\beta,h}(k) \end{bmatrix} + \frac{1}{L_{dq}} \int_{kT_s}^{(k+1)T_s} e^{-\frac{R_s}{L_{dq}}((k+1)T_s - \tau)} \begin{bmatrix} 1 & 0 & \omega_e(\tau)\sin(\theta_e(\tau)) \\ 0 & 1 & -\omega_e(\tau)\cos(\theta_e(\tau)) \end{bmatrix} \begin{bmatrix} u_\alpha(\tau) \\ u_\beta(\tau) \\ \lambda_{pm} \end{bmatrix} d\tau. \tag{3.7}$$

For the purpose of discretization, the inverter switching can be neglected, and the stator reference frame voltages can be considered constant over one sampling period $u_\alpha(t) = u_\alpha(k) = const.$ and $u_\beta(t) = u_\beta(k) = const.$ if $kT_s \leq t < (k+1)T_s$. Evaluating integrals then results in the following form of system (3.7):

$$\begin{bmatrix} i_{\alpha,h}(k+1) \\ i_{\beta,h}(k+1) \end{bmatrix} = e^{-\frac{R_s}{L_{dq}}T_s} \begin{bmatrix} i_{\alpha,h}(k) \\ i_{\beta,h}(k) \end{bmatrix} + \mathbf{B}_{d,h}^{\alpha\beta} \begin{bmatrix} u_\alpha(k) \\ u_\beta(k) \\ \lambda_{pm} \end{bmatrix} \tag{3.8}$$

where

$$\mathbf{B}_{d,h}^{\alpha\beta} = \frac{1}{R_s} \begin{bmatrix} 1 - e^{-\frac{R_s}{L_{dq}}T_s} & 0 & \frac{R_s}{L_{dq}} \int_{kT_s}^{(k+1)T_s} e^{-\frac{R_s}{L_{dq}}((k+1)T_s - \tau)} \omega_e(\tau)\sin(\theta_e(\tau))d\tau \\ 0 & 1 - e^{-\frac{R_s}{L_{dq}}T_s} & -\frac{R_s}{L_{dq}} \int_{kT_s}^{(k+1)T_s} e^{-\frac{R_s}{L_{dq}}((k+1)T_s - \tau)} \omega_e(\tau)\cos(\theta_e(\tau))d\tau \end{bmatrix}. \tag{3.9}$$

Integrals in expression (3.9) do not have an analytic solution since the time representation of the electrical angle is unknown. However, these integrals can be simplified

using integration by parts to the velocity independent form. We have

$$
\begin{aligned}
I_1 &= \frac{R_s}{L_{dq}} \int_{kT_s}^{(k+1)T_s} e^{-\frac{R_s}{L_{dq}}((k+1)T_s-\tau)} \omega_e(\tau) \sin(\theta_e(\tau)) d\tau \\
I_1 &= -\frac{R_s}{L_{dq}} \left(\cos(\theta_e(k+1)) - e^{-\frac{R_s}{L_{dq}}T_s} \cos(\theta_e(k)) \right) + \\
&\quad + \frac{R_s^2}{L_{dq}^2} \int_{kT_s}^{(k+1)T_s} e^{-\frac{R_s}{L_{dq}}((k+1)T_s-\tau)} \cos(\theta_e(\tau)) d\tau \\
I_2 &= -\frac{R_s}{L_{dq}} \int_{kT_s}^{(k+1)T_s} e^{-\frac{R_s}{L_{dq}}((k+1)T_s-\tau)} \omega_e(\tau) \cos(\theta_e(\tau)) d\tau \\
I_2 &= -\frac{R_s}{L_{dq}} \left(\sin(\theta_e(k+1)) - e^{-\frac{R_s}{L_{dq}}T_s} \sin(\theta_e(k)) \right) + \\
&\quad + \frac{R_s^2}{L_{dq}^2} \int_{kT_s}^{(k+1)T_s} e^{-\frac{R_s}{L_{dq}}((k+1)T_s-\tau)} \sin(\theta_e(\tau)) d\tau.
\end{aligned} \tag{3.10}
$$

It is possible to calculate integrals in (3.10) numerically [26]; however, such solution leads to non-zero back electromotive force if $\omega_e = 0$. This issue results in a significant distortion occurring in rotor reference frame currents. Therefore, integrals in (3.10) are approximately solved based on the mathematical analysis of back electromotive force. The solution of integrals in (3.10) can be approximated as in

$$
\begin{aligned}
\frac{R_s^2}{L_{dq}^2} \int_{kT_s}^{(k+1)T_s} e^{-\frac{R_s}{L_{dq}}((k+1)T_s-\tau)} \cos(\theta_e(\tau)) d\tau &\approx \frac{R_s}{L_{dq}} \left(K_1 \cos(\theta_e(k+1)) - K_2 \cos(\theta_e(k)) \right) \\
\frac{R_s^2}{L_{dq}^2} \int_{kT_s}^{(k+1)T_s} e^{-\frac{R_s}{L_{dq}}((k+1)T_s-\tau)} \sin(\theta_e(\tau)) d\tau &\approx \frac{R_s}{L_{dq}} \left(K_1 \sin(\theta_e(k+1)) - K_2 \sin(\theta_e(k)) \right)
\end{aligned} \tag{3.11}
$$

where constants K_1 and K_2 have to be calculated based on the back electromotive force properties. Substituting (3.11) into (3.10) results in

$$
\begin{aligned}
I_1 &\approx -\frac{R_s}{L_{dq}} \left((1-K_1) \cos(\theta_e(k+1)) - \left(e^{-\frac{R_s}{L_{dq}}T_s} - K_2 \right) \cos(\theta_e(k)) \right) \\
I_2 &\approx -\frac{R_s}{L_{dq}} \left((1-K_1) \sin(\theta_e(k+1)) - \left(e^{-\frac{R_s}{L_{dq}}T_s} - K_2 \right) \sin(\theta_e(k)) \right).
\end{aligned} \tag{3.12}
$$

If a motor's angular velocity equals 0, then the electrical angle reads $\theta_e(k+1) = \theta_e(k)$ and the back electromotive force has to be 0. Therefore, $I_1 = 0$ and $I_2 = 0$ if $\theta_e(k+1) = \theta_e(k)$, yielding

$$
1 - K_1 = e^{-\frac{R_s}{L_{dq}}T_s} - K_2. \tag{3.13}
$$

As seen in (3.1), the contributions of permanent magnets to $\mathrm{d}i_d/\mathrm{d}t$ and $\mathrm{d}i_q/\mathrm{d}t$ are equal to 0 and $-\omega_e(t)\lambda_{pm}/L_{dq}$. Therefore, the contributions of permanent magnets to the derivatives of stator reference frame currents $\mathrm{d}i_\alpha/\mathrm{d}t$ and $\mathrm{d}i_\beta/\mathrm{d}t$ are equal to $\sin(\theta_e(t))\omega_e(t)\lambda_{pm}/L_{dq}$ and $-\cos(\theta_e(t))\omega_e(t)\lambda_{pm}/L_{dq}$, resulting in $K_1 = 0$.

Hence, the healthy part of the shorted motor model can be written in the linear time-varying discrete-time form as in

$$\begin{bmatrix} i_{\alpha,h}(k+1) \\ i_{\beta,h}(k+1) \end{bmatrix} = \mathbf{A}_{d,h}^{\alpha\beta}((k+1)T_s, kT_s) \begin{bmatrix} i_{\alpha,h}(k) \\ i_{\beta,h}(k) \end{bmatrix} + \mathbf{B}_{d,h}^{\alpha\beta}((k+1)T_s, kT_s) \begin{bmatrix} u_\alpha(k) \\ u_\beta(k) \\ \lambda_{pm} \end{bmatrix} \quad (3.14)$$

where

$$\begin{aligned} \mathbf{A}_{d,h}^{\alpha\beta}((k+1)T_s, kT_s) &= \begin{bmatrix} e^{-\frac{R_s}{L_{dq}}T_s} & 0 \\ 0 & e^{-\frac{R_s}{L_{dq}}T_s} \end{bmatrix} \\ \mathbf{B}_{d,h}^{\alpha\beta}((k+1)T_s, kT_s) &= \frac{1}{R_s} \begin{bmatrix} 1 - e^{-\frac{R_s}{L_{dq}}T_s} & 0 & I_1((k+1)T_s, kT_s) \\ 0 & 1 - e^{-\frac{R_s}{L_{dq}}T_s} & I_2((k+1)T_s, kT_s) \end{bmatrix} \\ I_1((k+1)T_s, kT_s) &\approx -\frac{R_s}{L_{dq}} \left(\cos(\theta_e(k+1)) - \cos(\theta_e(k))\right) \\ I_2((k+1)T_s, kT_s) &\approx -\frac{R_s}{L_{dq}} \left(\sin(\theta_e(k+1)) - \sin(\theta_e(k))\right). \end{aligned} \quad (3.15)$$

3.2 Fault current discretization

The differential equation and output relation describe the fault current contribution as in (1.28). However, since the inductances of the validated machine are close to each other (Table 1.2), the fault inductance can be approximated as in

$$L_f \approx \frac{2}{3} {x_f^*}^2 n_p (n_s - 1) L_{dq}. \quad (3.16)$$

Then the differential equation describing the fault current can be written in the following form:

$$\frac{\mathrm{d}}{\mathrm{d}t} i_f = -\frac{R_{f,dq}}{3L_f} i_f + \frac{x_f^*}{L_f} \begin{bmatrix} \cos(\theta_e + \frac{\phi}{2}) \\ -\sin(\theta_e + \frac{\phi}{2}) \end{bmatrix}^T \cdot \begin{bmatrix} u_d \\ u_q \end{bmatrix} \quad (3.17)$$

where

$$R_{f,dq} = x_f^* \left(3 - 2x_f^*\right) R_s + 3R_f^*. \quad (3.18)$$

Transforming the input vector into the stator reference frame provides the linear time-invariant definition of fault current. We have

$$\frac{\mathrm{d}}{\mathrm{d}t} i_f = -\frac{R_{f,dq}}{3L_f} i_f + \frac{x_f^*}{L_f} \begin{bmatrix} \cos(\frac{\phi}{2}) \\ -\sin(\frac{\phi}{2}) \end{bmatrix}^T \cdot \begin{bmatrix} u_\alpha \\ u_\beta \end{bmatrix}. \quad (3.19)$$

The discrete-time equivalent of the linear time-invariant system (3.19) is then well defined as in

$$i_f(k+1) = e^{-\frac{R_{f,dq}}{3L_f}T_s} i_f(k) + \frac{3x_f^*}{R_{f,dq}} \left(1 - e^{-\frac{R_{f,dq}}{3L_f}T_s}\right) \begin{bmatrix} \cos(\frac{\phi}{2}) \\ -\sin(\frac{\phi}{2}) \end{bmatrix}^T \cdot \begin{bmatrix} u_\alpha(k) \\ u_\beta(k) \end{bmatrix}. \quad (3.20)$$

3.3 Stator reference frame discrete-time model

Discretized model of healthy part (3.14) and fault current (3.20) can be combined into one discrete-time system as in

$$\begin{bmatrix} i_{\alpha,h}(k+1) \\ i_{\beta,h}(k+1) \\ i_f(k+1) \end{bmatrix} = \begin{bmatrix} \mathbf{A}_{d,h}^{\alpha\beta}((k+1)T_s, kT_s) & \mathbf{0} \\ \mathbf{0}^T & e^{-\frac{R_{f,dq}}{3L_f}T_s} \end{bmatrix} \cdot \begin{bmatrix} i_{\alpha,h}(k) \\ i_{\beta,h}(k) \\ i_f(k) \end{bmatrix} + \begin{bmatrix} \mathbf{B}_{d,h}^{\alpha\beta}((k+1)T_s, kT_s) \\ \mathbf{B}_{d,f}^{\alpha\beta}((k+1)T_s, kT_s) \end{bmatrix} \cdot \begin{bmatrix} u_\alpha(k) \\ u_\beta(k) \\ \lambda_{pm} \end{bmatrix} \tag{3.21}$$

where $\mathbf{A}_{d,h}^{\alpha\beta}((k+1)T_s, kT_s)$ and $\mathbf{B}_{d,h}^{\alpha\beta}((k+1)T_s, kT_s)$ are defined as in (3.15), $\mathbf{0}^T$ stands for $\begin{bmatrix} 0 & 0 \end{bmatrix}$, and $\mathbf{B}_{d,f}^{\alpha\beta}((k+1)T_s, kT_s)$ reads

$$\mathbf{B}_{d,f}^{\alpha\beta}((k+1)T_s, kT_s) = \frac{3x_f^*}{R_{f,dq}} \begin{bmatrix} \left(1 - e^{-\frac{R_{f,dq}}{3L_f}T_s}\right)\cos(\frac{\phi}{2}) & -\left(1 - e^{-\frac{R_{f,dq}}{3L_f}T_s}\right)\sin(\frac{\phi}{2}) & 0 \end{bmatrix}. \tag{3.22}$$

Since $Z\left\{\mathbf{A}_d^{\alpha\beta}((k+1)T_s, kT_s)\mathbf{i}(k)\right\} = \mathbf{A}_d^{\alpha\beta}((k+1)T_s, kT_s)Z\left\{\mathbf{i}(k)\right\}$ where $\mathbf{i}(k)$ stands for $\begin{bmatrix} i_{\alpha,h}(k) & i_{\beta,h}(k) & i_f(k) \end{bmatrix}^T$ and $\mathbf{A}_d^{\alpha\beta}((k+1)T_s, kT_s)$ is the state matrix as in (3.21), it is possible to describe system (3.21) using Z-transform. We have

$$\begin{bmatrix} I_{\alpha,h}(z) \\ I_{\beta,h}(z) \\ I_f(z) \end{bmatrix} = \left(z\mathbf{I} - \mathbf{A}_d^{\alpha\beta}((k+1)T_s, kT_s)\right)^{-1} Z\left\{ \mathbf{B}_d^{\alpha\beta}((k+1)T_s, kT_s) \begin{bmatrix} u_\alpha(k) \\ u_\beta(k) \\ \lambda_{pm} \end{bmatrix} \right\} \tag{3.23}$$

where $\mathbf{I}$ is the 3×3 identity matrix and $\mathbf{B}_d^{\alpha\beta}((k+1)T_s, kT_s)$ is the input matrix as in (3.21). Evaluating expression (3.23) leads to the following solution:

$$\begin{bmatrix} I_{\alpha,h}(z) \\ I_{\beta,h}(z) \\ I_f(z) \end{bmatrix} = \begin{bmatrix} \frac{1}{R_s}\frac{1-e^{-\frac{R_s}{L_{dq}}T_s}}{z-e^{-\frac{R_s}{L_{dq}}T_s}} & 0 & \frac{3x_f^*\cos(\frac{\phi}{2})}{R_{f,dq}}\frac{1-e^{-\frac{R_{f,dq}}{3L_f}T_s}}{z-e^{-\frac{R_{f,dq}}{3L_f}T_s}} \\ 0 & \frac{1}{R_s}\frac{1-e^{-\frac{R_s}{L_{dq}}T_s}}{z-e^{-\frac{R_s}{L_{dq}}T_s}} & -\frac{3x_f^*\sin(\frac{\phi}{2})}{R_{f,dq}}\frac{1-e^{-\frac{R_{f,dq}}{3L_f}T_s}}{z-e^{-\frac{R_{f,dq}}{3L_f}T_s}} \\ -\frac{\lambda_{pm}}{L_{dq}}\frac{z-1}{z-e^{-\frac{R_s}{L_{dq}}T_s}} & 0 & 0 \\ 0 & -\frac{\lambda_{pm}}{L_{dq}}\frac{z-1}{z-e^{-\frac{R_s}{L_{dq}}T_s}} & 0 \end{bmatrix}^T \cdot \begin{bmatrix} U_\alpha(z) \\ U_\beta(z) \\ Z\{\cos(\theta_e(k))\} \\ Z\{\sin(\theta_e(k))\} \end{bmatrix}. \tag{3.24}$$

The algebraic equation describes the output rotor reference frame currents as in (1.28). However, this expression can be transformed into the stator reference frame, yielding

$$\begin{bmatrix} i_\alpha(k) \\ i_\beta(k) \end{bmatrix} = \begin{bmatrix} 1 & 0 & \frac{2}{3}x_f^*\cos\left(\frac{\phi}{2}\right) \\ 0 & 1 & -\frac{2}{3}x_f^*\sin\left(\frac{\phi}{2}\right) \end{bmatrix} \cdot \begin{bmatrix} i_{\alpha,h}(k) \\ i_{\beta,h}(k) \\ i_f(k) \end{bmatrix}. \tag{3.25}$$

Since the transition matrix in (3.25) is time-invariant, description (3.25) also holds for the signals defined in Z-transform. Therefore, this description might be applied to determine the input-output behavior of the permanent magnet synchronous machine under the inter-turn short circuit fault out of (3.24). We have

$$\begin{bmatrix} I_\alpha(z) \\ I_\beta(z) \end{bmatrix} = \begin{bmatrix} F_h(z) + (1+\cos(\phi))F_f(z) & -\sin(\phi)F_f(z) & F_{pm}(z) & 0 \\ -\sin(\phi)F_f(z) & F_h(z) + (1-\cos(\phi))F_f(z) & 0 & F_{pm}(z) \end{bmatrix} \cdot \begin{bmatrix} U_\alpha(z) \\ U_\beta(z) \\ Z\{\cos(\theta_e(k))\} \\ Z\{\sin(\theta_e(k))\} \end{bmatrix} \tag{3.26}$$

where

$$F_h(z) = \frac{1}{R_s}\frac{1-e^{-\frac{R_s}{L_{dq}}T_s}}{z-e^{-\frac{R_s}{L_{dq}}T_s}} \quad F_f(z) = \frac{x_f^{*2}}{R_{f,dq}}\frac{1-e^{-\frac{R_{f,dq}}{3L_f}T_s}}{z-e^{-\frac{R_{f,dq}}{3L_f}T_s}} \quad F_{pm}(z) = -\frac{\lambda_{pm}}{L_{dq}}\frac{z-1}{z-e^{-\frac{R_s}{L_{dq}}T_s}}. \tag{3.27}$$

System (3.26) is then transformed into the time domain resulting in the following description of $\alpha-\beta$ currents:

$$\begin{aligned} &\begin{bmatrix} i_\alpha(k) \\ i_\beta(k) \end{bmatrix} = \left(e^{-\frac{R_s}{L_{dq}}T_s} + e^{-\frac{R_{f,dq}}{3L_f}T_s}\right)\begin{bmatrix} i_\alpha(k-1) \\ i_\beta(k-1) \end{bmatrix} - e^{-\left(\frac{R_s}{L_{dq}}+\frac{R_{f,dq}}{3L_f}\right)T_s}\begin{bmatrix} i_\alpha(k-2) \\ i_\beta(k-2) \end{bmatrix} + \\ &+ (\sigma_h\mathbf{I}+\sigma_f\Phi)\cdot\begin{bmatrix} u_\alpha(k-1) \\ u_\beta(k-1) \end{bmatrix} - \left(\sigma_h e^{-\frac{R_{f,dq}}{3L_f}T_s}\mathbf{I} + \sigma_f e^{-\frac{R_s}{L_{dq}}T_s}\Phi\right)\cdot\begin{bmatrix} u_\alpha(k-2) \\ u_\beta(k-2) \end{bmatrix} - \\ &- \frac{\lambda_{pm}}{L_{dq}}\begin{bmatrix} \cos(\theta_e(k)) \\ \sin(\theta_e(k)) \end{bmatrix} + \frac{\lambda_{pm}}{L_{dq}}\left(1+e^{-\frac{R_{f,dq}}{3L_f}T_s}\right)\begin{bmatrix} \cos(\theta_e(k-1)) \\ \sin(\theta_e(k-1)) \end{bmatrix} - \\ &- \frac{\lambda_{pm}}{L_{dq}}e^{-\frac{R_{f,dq}}{3L_f}T_s}\begin{bmatrix} \cos(\theta_e(k-2)) \\ \sin(\theta_e(k-2)) \end{bmatrix} \end{aligned} \tag{3.28}$$

where

$$\begin{aligned} \sigma_h &= \frac{1}{R_s}\left(1-e^{-\frac{R_s}{L_{dq}}T_s}\right) & \sigma_f &= \frac{x_f^{*2}}{R_{f,dq}}\left(1-e^{-\frac{R_{f,dq}}{3L_f}T_s}\right) \\ \mathbf{I} &= \begin{bmatrix} 1 & 0 \\ 0 & 1 \end{bmatrix} & \Phi &= \begin{bmatrix} 1+\cos(\phi) & -\sin(\phi) \\ -\sin(\phi) & 1-\cos(\phi) \end{bmatrix}. \end{aligned} \tag{3.29}$$

Parameters that are related to the fault relevance ratio $\frac{x_f^{*2}}{R_{f,dq}}$ and $\frac{R_{f,dq}}{3L_f}$ are calculated based on the substitutions (1.16), (3.16), and (3.18), as in

$$\begin{aligned} \frac{x_f^{*2}}{R_{f,dq}} &= \frac{1}{3n_s^2R_fx_f^{-2} + 3n_sn_pR_sx_f^{-1} + (1-3n_p)R_s} \\ \frac{R_{f,dq}}{3L_f} &= \frac{3n_s^2R_fx_f^{-2} + 3n_sn_pR_sx_f^{-1} + (1-3n_p)R_s}{2n_p(n_s-1)L_{dq}}. \end{aligned} \tag{3.30}$$

Note that if $x_f = 0$, then $\frac{x_f^{*2}}{R_{f,dq}} \to 0$ and $e^{-\frac{R_{f,dq}}{3L_f}T_s} \to 0$. Hence, the behavior of the healthy currents (3.14) is achieved.

3.4 Discrete-time model verification

The continuous-time model of PMSM under the inter-turn short circuit fault was already validated via open-loop measurement of the back electromotive force and fault current of the configurable motor (Section 1.5). Therefore, since the fitting of the continuous-time model was already proven, it is possible to verify the discrete-time model only within the simulation. For this purpose, closed-loop verification is implemented.

The control system regulates the continuous-time model to the mechanical angular velocity setpoint ω_m^*, and the short circuits are simulated with the following fault relevance: $x_f = 6/25$ and $x_f = 14/25$ in cases $n_p = 1$, $n_s = 3$ and $n_p = 2$, $n_s = 3$, and $x_f = 3/25$ and $x_f = 6/25$ if $n_p = 1$, $n_s = 1$. The control system parameters and electrical parameters of machine models are defined for three winding connections in the initialization code of the subsystems. Then it is possible to change these parameters by a switch in the subsystems masks. Torque load is set to be 0 during this experiment, but the dry and viscous frictions are involved into the simulation. The maximum current is limited to $I_{max} = 8\,A$, and the DC bus voltage is $U_{dc} = 55\,V$. Figure 3.1 visualizes the MATLAB Simulink realization of the verification experiment.

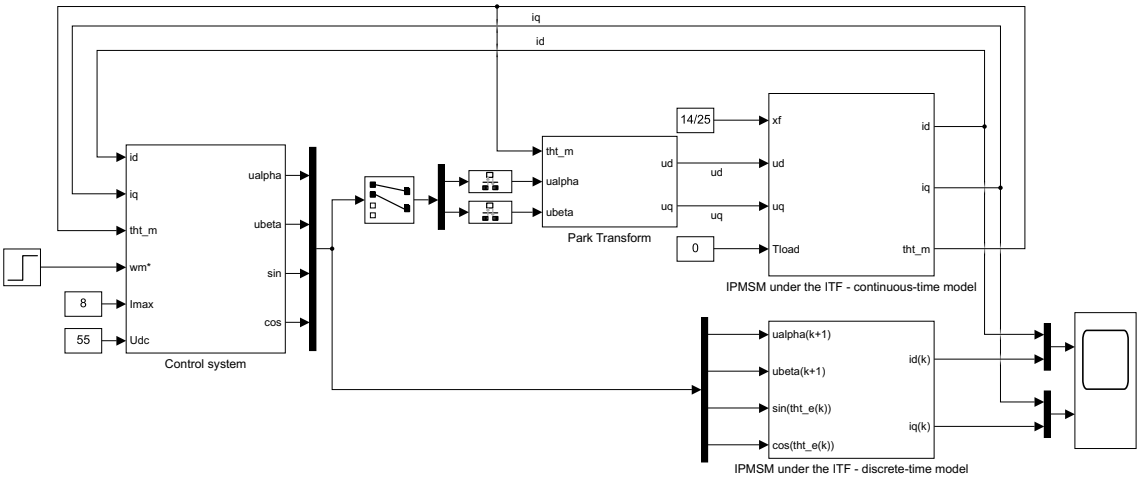

Fig. 3.1: Verification of the discrete-time model in a closed control loop

Since the continuous-time model is implemented in the rotor reference frame, the transformation of input currents from (abc) to $d-q$ is neglected in the control system (Section 2.4), and the transformation of output voltages is reduced only to the inverse Park's transformation (from $d-q$ to $\alpha-\beta$). Therefore, the condition of constant u_α and u_β over one sampling period is fulfilled. These voltages are then transformed back into the rotor reference frame using the rate transition blocks and

continuous-time Park's transformation (Figure 3.1). Due to this connection, the simulated closed control loop fits the actual machine behavior more precisely. The only difference in the interpretation of the inputs is caused by neglected inverter switching. Stator reference frame voltages are then together with the discretized sine and cosine of electrical angle connected as inputs of the discrete-time model. MATLAB Simulink implementation of model (3.28) is visualized in Figure 3.2.

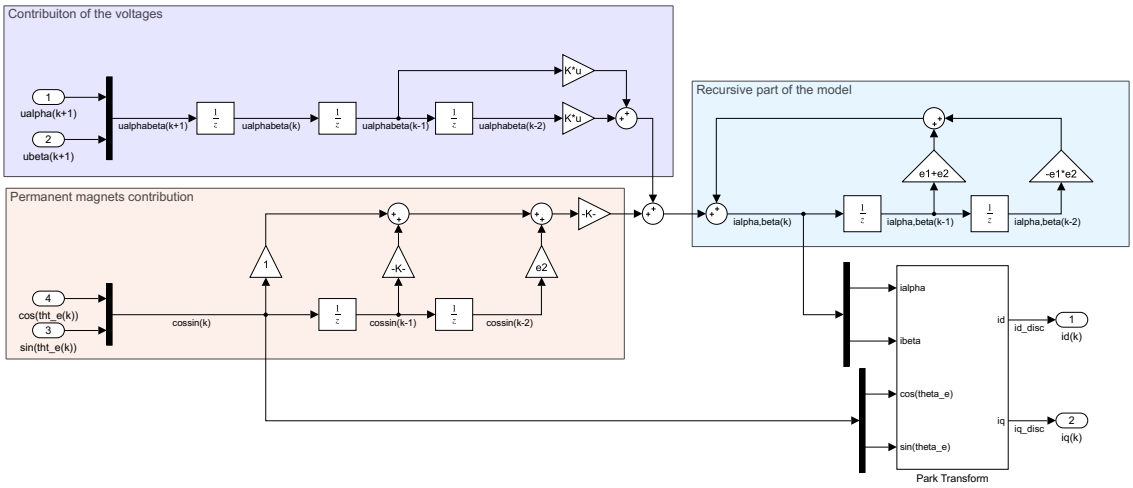

Fig. 3.2: Realization of the discrete-time model of IPMSM under ITF

As seen in Figure 3.2 the model is extended by discrete-time Park's transformation, and the rotor reference frame currents are sent to the outputs. Hence, the discrete and continuous-time models are excited with the same input signals, and the transients of the rotor reference frame currents are compared. The comparison of simulated continuous and discrete-time currents is visualized for three winding connections in Figure 3.3. Differences are caused by direct L_d and quadrature L_q axis inductance approximation by a common inductance L_{dq} in the discrete-time model.

a) winding connection $n_p = 1$; $n_s = 1$

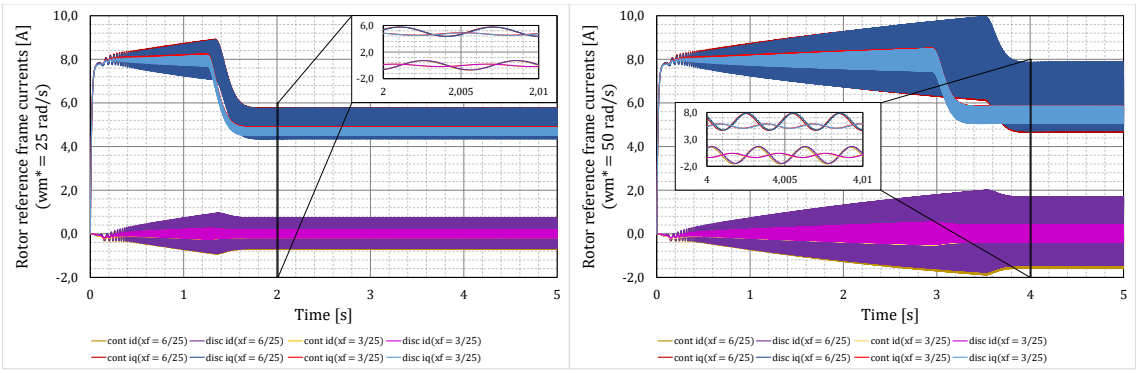

b) winding connection $n_p = 1$; $n_s = 3$

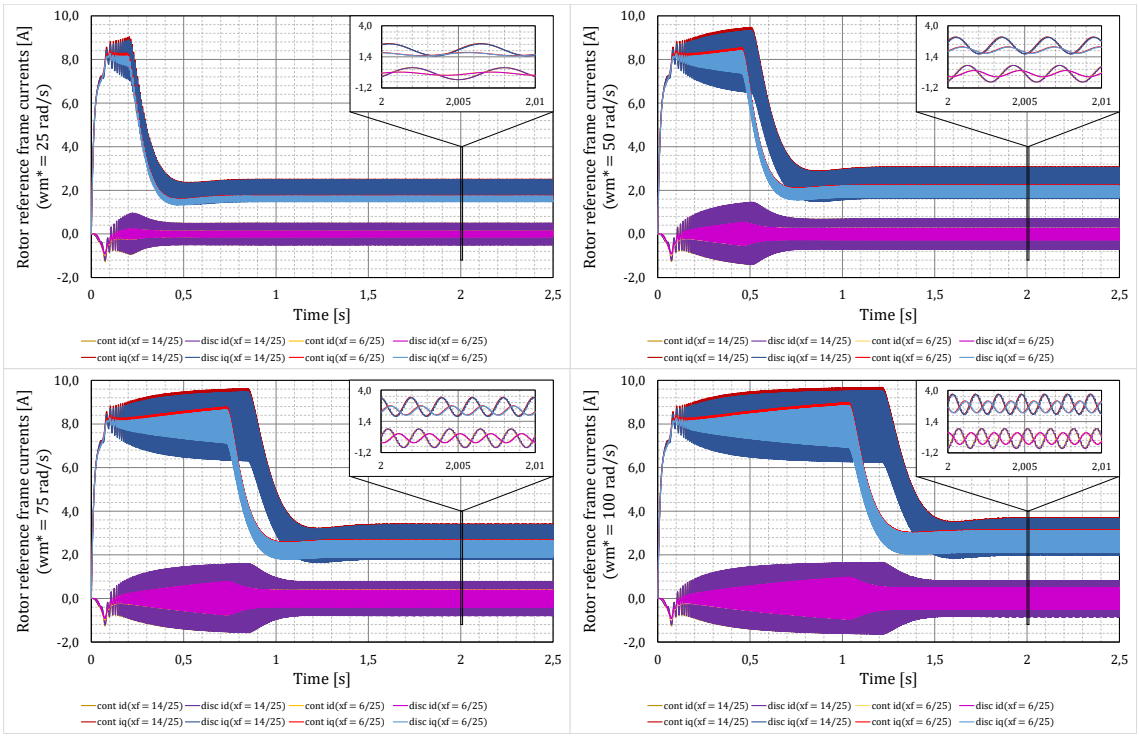

c) winding connection $n_p = 2$; $n_s = 3$

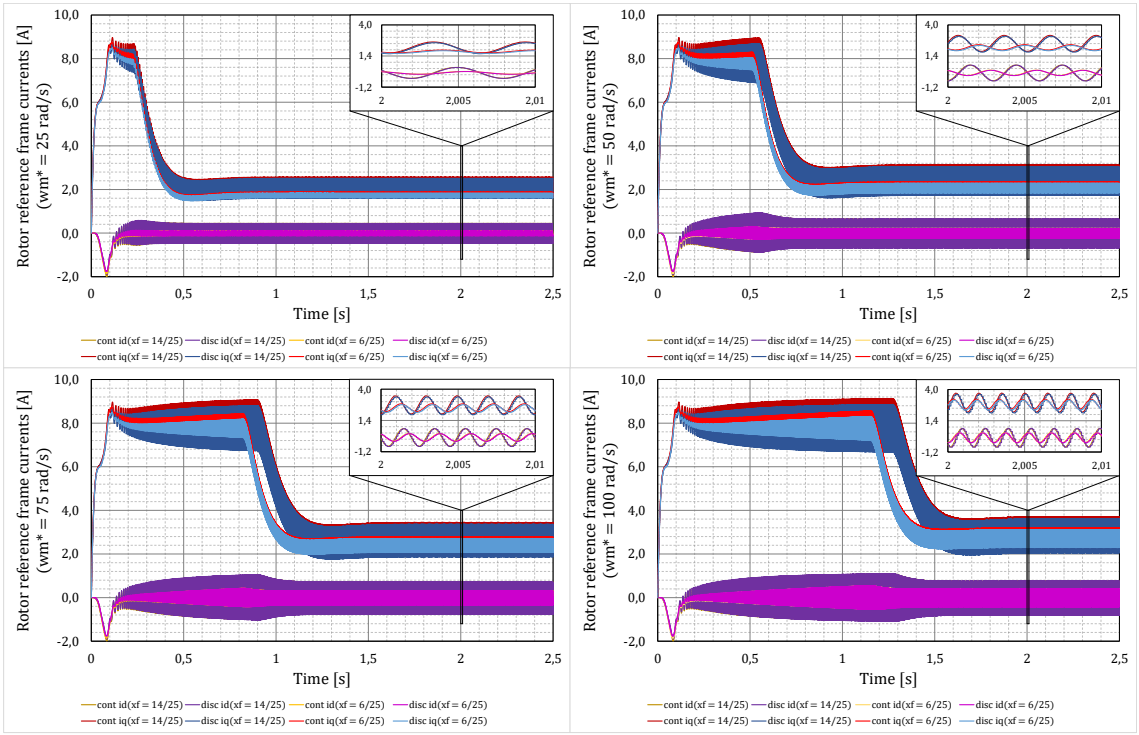

Fig. 3.3: Comparison between continuous and discrete-time model

4 Fault relevance identification

As presented in Section 3.3, PMSM under the ITF is described by the linear discrete-time model (3.28), where the fault-related specifications (fault relevance x_f and resistance of a short circuit R_f) are interpreted as time-varying parameters (3.30). Hence, the ITF diagnostics presented in this thesis are based on the parametric estimation of linear systems [27] - [28].

The input signals of discrete-time model (3.28) are combinations of sine and cosine waves with different amplitudes (defined by the rotor reference frame voltages u_d and u_q) and the same frequency ω_e. Therefore, the persistence of input signals is insufficient to identify all the parameters of the discrete-time model unless a machine is accelerating or decelerating. Hence, the discrete-time model must be modified to reduce the number of identified parameters.

4.1 Problem definition

Since the short circuits may occur only in three phases, there is a finite set of parameter ϕ values (if the ITF is in phase 'a' then $\phi = 0$, if the ITF is in phase 'b' then $\phi = \frac{2\pi}{3}$, and if the ITF is in phase 'c' then $\phi = -\frac{2\pi}{3}$). An interesting situation occurs if $\phi = 0$. In such a case, the input-output behavior of PMSM under the ITF can be determined out of (3.26) as in

$$\begin{bmatrix} I_\alpha(z) \\ I_\beta(z) \end{bmatrix} = \begin{bmatrix} F_h(z) + 2F_f(z) & 0 & F_{pm}(z) & 0 \\ 0 & F_h(z) & 0 & F_{pm}(z) \end{bmatrix} \cdot \begin{bmatrix} U_\alpha(z) \\ U_\beta(z) \\ Z\{\cos(\theta_e(k))\} \\ Z\{\sin(\theta_e(k))\} \end{bmatrix} \tag{4.1}$$

where the transmissions $F_h(z)$, $F_f(z)$, and $F_{pm}(z)$ are defined as in (3.27). In (4.1), only one currents component (i_α) is affected by ITF, and the other (i_β) follows healthy machine behavior. A similar situation can be achieved for short circuits in different phases by transforming currents and voltages. We have

$$\begin{bmatrix} i_\alpha \\ i_\beta \end{bmatrix} = \mathbf{R}(\phi) \begin{bmatrix} i^*_\alpha \\ i^*_\beta \end{bmatrix} \qquad \begin{bmatrix} u_\alpha \\ u_\beta \end{bmatrix} = \mathbf{R}(\phi) \begin{bmatrix} u^*_\alpha \\ u^*_\beta \end{bmatrix} \tag{4.2}$$

where

$$\mathbf{R}(\phi) = \begin{bmatrix} 1 & \frac{\sin(\phi)}{1+\cos(\phi)} \\ -\frac{\sin(\phi)}{1+\cos(\phi)} & 1 \end{bmatrix} \qquad \mathbf{R}^{-1}(\phi) = \frac{1}{2} \begin{bmatrix} 1+\cos(\phi) & -\sin(\phi) \\ \sin(\phi) & 1+\cos(\phi) \end{bmatrix}. \tag{4.3}$$

Note that the transformation matrices defined in (4.3) result in an identity matrix if the short circuit is in phase 'a'. If (4.2) is substituted into (3.26), an analogous

description to (4.1) is obtained. The only difference lies in the rotated contributions of permanent magnets. Therefore, the discrete-time model can always be simplified to the form that contains two independent currents components, where only one of them is affected by ITF. The cross-correlation between $i^*_\alpha(k)$ and $u^*_\beta(k-1)$ for all possible ϕ-based transformation matrices (4.3) can then be evaluated to determine which stator phase is shorted. For example, suppose a short circuit occurs in phase 'b'. In that case, the cross-correlation between the transformed variables $i^*_\alpha(k)$ and $u^*_\beta(k-1)$ that are obtained by applying transformation matrix $\mathbf{R}^{-1}(\frac{2\pi}{3})$ to $i_\alpha(k)$ and $u_\beta(k-1)$ is significantly lower than the cross-correlation evaluated from variables obtained by applying $\mathbf{R}^{-1}(0)$ and $\mathbf{R}^{-1}(-\frac{2\pi}{3})$. Therefore, fault in phase 'b' is indicated. However, since the configurable motor used for algorithm verification is primarily designed to support short circuits in phase 'a', the phase detection won't be implemented.

The simplified system (4.1) is then transformed into the time-domain, yielding

$$\begin{aligned}
i_\beta(k) &= e^{-\frac{R_s}{L_{dq}}T_s} i_\beta(k-1) + \sigma_h u_\beta(k-1) - \frac{\lambda_{pm}}{L_{dq}}(\sin(\theta_e(k)) - \sin(\theta_e(k-1))) \\
i_\alpha(k) &= \left(e^{-\frac{R_s}{L_{dq}}T_s} + e^{-\frac{R_{f,dq}}{3L_f}T_s}\right) i_\alpha(k-1) - e^{-\left(\frac{R_s}{L_{dq}}+\frac{R_{f,dq}}{3L_f}\right)T_s} i_\alpha(k-2) + \\
&\quad + (\sigma_h + 2\sigma_f) u_\alpha(k-1) - \left(\sigma_h e^{-\frac{R_{f,dq}}{3L_f}T_s} + 2\sigma_f e^{-\frac{R_s}{L_{dq}}T_s}\right) u_\alpha(k-2) - \\
&\quad - \frac{\lambda_{pm}}{L_{dq}}\cos(\theta_e(k)) + \frac{\lambda_{pm}}{L_{dq}}\left(1 + e^{-\frac{R_{f,dq}}{3L_f}T_s}\right)\cos(\theta_e(k-1)) - \\
&\quad - \frac{\lambda_{pm}}{L_{dq}} e^{-\frac{R_{f,dq}}{3L_f}T_s}\cos(\theta_e(k-2))
\end{aligned} \tag{4.4}$$

where σ_h and σ_f are defined as in (3.29). As seen in (4.4), the behavior of i_β is theoretically unaffected by ITF. Hence, it is possible to estimate the healthy parameters even if the ITF occurs. Rewriting the difference equation that describes i_β into a form suitable for parametric identification results in

$$\begin{bmatrix} i_\beta(k) \\ i_\beta(k-1) \\ i_\beta(k-2) \\ i_\beta(k-3) \\ \vdots \end{bmatrix} = \begin{bmatrix} i_\beta(k-1) & u_\beta(k-1) & \sin(\theta_e(k-1)) - \sin(\theta_e(k)) \\ i_\beta(k-2) & u_\beta(k-2) & \sin(\theta_e(k-2)) - \sin(\theta_e(k-1)) \\ i_\beta(k-3) & u_\beta(k-3) & \sin(\theta_e(k-3)) - \sin(\theta_e(k-2)) \\ i_\beta(k-4) & u_\beta(k-4) & \sin(\theta_e(k-4)) - \sin(\theta_e(k-3)) \\ \vdots & \vdots & \vdots \end{bmatrix} \cdot \begin{bmatrix} p_{h,1} \\ p_{h,2} \\ p_{h,3} \end{bmatrix} \tag{4.5}$$

where

$$\begin{aligned}
p_{h,1} &= e^{-\frac{R_s}{L_{dq}}T_s} & p_{h,2} &= \frac{1}{R_s}\left(1 - e^{-\frac{R_s}{L_{dq}}T_s}\right) & p_{h,3} &= \frac{\lambda_{pm}}{L_{dq}} \\
R_s &= \frac{1-p_{h,1}}{p_{h,2}} & L_{dq} &= -\frac{T_s(1-p_{h,1})}{\ln(p_{h,1})p_{h,2}} & \lambda_{pm} &= -\frac{T_s(1-p_{h,1})}{\ln(p_{h,1})p_{h,2}} p_3.
\end{aligned} \tag{4.6}$$

Note that the persistence of input signals is insufficient to identify three parameters if the machine runs at constant angular velocity. Generally, it is possible to identify two parameters by a harmonic signal that contains only one frequency [27]. This problem has a relatively simple solution. The identification procedure of healthy parameters has to start before a machine is driven to the velocity setpoint.

The estimated healthy parameters $p_{h,1}$, $p_{h,2}$, and $p_{h,3}$ are then used to reduce the order of difference equation that describes i_α. We have the following output and input transformation:

$$\begin{aligned} y(k) &= i_\alpha(k) - p_{h,1} i_\alpha(k-1) - p_{h,2} u_\alpha(k-1) + p_{h,3}\cos(\theta_e(k)) - p_{h,3}\cos(\theta_e(k-1)) \\ v(k) &= u_\alpha(k) - p_{h,1} u_\alpha(k-1) \end{aligned} \tag{4.7}$$

where y is the new output and v is the new input. Since these variables are formed as a linear combination of harmonic waveforms, they are also harmonic with the same frequency as the original signals. If (4.7) is substituted into i_α description (4.4), the transformed difference equation is derived as in

$$y(k) = e^{-\frac{R_{f,dq}}{3L_f}T_s} y(k-1) + 2\frac{x_f^{*2}}{R_{f,dq}}\left(1 - e^{-\frac{R_{f,dq}}{3L_f}T_s}\right) v(k-1). \tag{4.8}$$

Equation (4.8) is then easily transformable into a form suitable for parametric identification. We have

$$\begin{bmatrix} y(k) \\ y(k-1) \\ y(k-2) \\ y(k-3) \\ \vdots \end{bmatrix} = \begin{bmatrix} y(k-1) & v(k-1) \\ y(k-2) & v(k-2) \\ y(k-3) & v(k-3) \\ y(k-4) & v(k-4) \\ \vdots & \vdots \end{bmatrix} \cdot \begin{bmatrix} p_{f,1} \\ p_{f,2} \end{bmatrix} \tag{4.9}$$

where

$$p_{f,1} = e^{-\frac{R_{f,dq}}{3L_f}T_s} \qquad p_{f,2} = 2\frac{x_f^{*2}}{R_{f,dq}}\left(1 - e^{-\frac{R_{f,dq}}{3L_f}T_s}\right) \qquad \frac{R_{f,dq}}{x_f^{*2}} = 2\frac{1-p_{f,1}}{p_{f,2}}. \tag{4.10}$$

In this case, the persistence of the input signal v does not cause trouble since only two parameters are identified. Therefore, fault-related parameters can be estimated even if a machine runs at constant angular velocity.

As seen in (3.30), fault relevance x_f can not be calculated out of $R_{f,dq}/x_f^{*2}$ since the information about R_f is missing. There are a few ways how to deal with this issue. For example, it is possible to express fault relevance as a function dependent on short circuit resistance $x_f = f(R_f)$. However, in this thesis, the fault relevance is normalized and expresses what portion of winding is shorted by the zero short circuit

resistance $x_{f,n} = f(R_f = 0)$. Normalized fault relevance $x_{f,n}$ is then calculated as in

$$x_{f,n} = \frac{3n_s n_p R_s}{\frac{R_{f,dq}}{x_f^{*2}} + (3n_p - 1)R_s} \qquad x_{f,n} = \frac{x_f^2}{\frac{n_s R_f}{n_p R_s} + x_f}. \tag{4.11}$$

The online fault relevance diagnostic algorithm then contains the following steps:

1. Update the estimation of healthy parameters (4.5).
2. Calculate input and output transformation (4.7).
3. Update the estimation of ITF parameters (4.9).
4. Calculate series resistance R_s (4.6).
5. Evaluate $R_{f,dq}/x_f^{*2}$ (4.10).
6. Calculate normalized fault relevance $x_{f,n}$ (4.11).

It is assumed that information about winding architecture (number of parallel branches n_p and number of coils in series n_s) is available.

4.2 System noise analysis and filter design

This thesis aims to achieve fault relevance diagnostics running online on the drive system of the validated motor. Therefore, the possible sources of the system noise have to be analyzed. This step is essential since PMSMs are rotating machines and measured signals often contain periodic distortions. In terms of parametric estimation, the periodic distortion cause trouble since the system's inputs and outputs are correlated with the noise. The following sections will discuss only the particular case of winding connection $n_p = 1$, $n_s = 3$ since the configurable machine is designed to be connected as a double three-phase motor with three series-connected coils in the phase. It was measured that the periodic distortion is significantly higher in other connections than $n_p = 1$, $n_s = 3$ (Figure 2.8).

Traditionally, machine nonlinearities, periodic distortions, and measurement errors are reflected primarily in currents waveforms. One can admit that the angle measurement poses a source of uncertainties as well; however, an encoder measures the mechanical angle relatively precisely, and the contribution of angle uncertainties to the system noise is minimal. Hence, the measured stator currents can be used for the purpose of system noise analysis. We have

$$\begin{aligned} i_{a,r} &= i_a + \varepsilon_{a,p} + \varepsilon_{a,n} \\ i_{b,r} &= i_b + \varepsilon_{b,p} + \varepsilon_{b,n} \\ i_{c,r} &= i_c + \varepsilon_{c,p} + \varepsilon_{c,n} \end{aligned} \tag{4.12}$$

where $i_{a,r}$, $i_{b,r}$, and $i_{c,r}$ stand for measured stator currents, i_a, i_b, and i_c are ideal stator currents, $\varepsilon_{a,p}$, $\varepsilon_{b,p}$, and $\varepsilon_{c,p}$ represent periodic distortions, and $\varepsilon_{a,n}$, $\varepsilon_{b,n}$, and $\varepsilon_{c,n}$ stand for random non-periodic noises.

Due to the star connection of the motor, the ideal currents must satisfy the following equation (even if ITF is emulated):

$$i_a + i_b + i_c = 0. \tag{4.13}$$

However, most of the periodic distortions satisfy condition (4.13) as well, yielding

$$\varepsilon_{a,p} + \varepsilon_{b,p} + \varepsilon_{c,p} = 0. \tag{4.14}$$

Since all three stator currents are measured, conditions (4.13) and (4.14) can be applied to determine the random noise level of measured currents as in

$$i_{a,r} + i_{b,r} + i_{b,r} = \varepsilon_{a,n} + \varepsilon_{b,n} + \varepsilon_{c,n} = \varepsilon_n. \tag{4.15}$$

Hence, the sum of random noise components ε_n is calculated out of the sum of the measured currents, and the statistical properties can be evaluated. For this purpose, the data from experiments in Section 2.5 are used. The measured stator currents are summed up (including the data from transients areas where the machine is speeding up to the angular velocity setpoint ω_m^* and areas where the short circuits are emulated) and the mean values μ and variances σ^2 are calculated and presented together with the histograms in Figure 4.1.

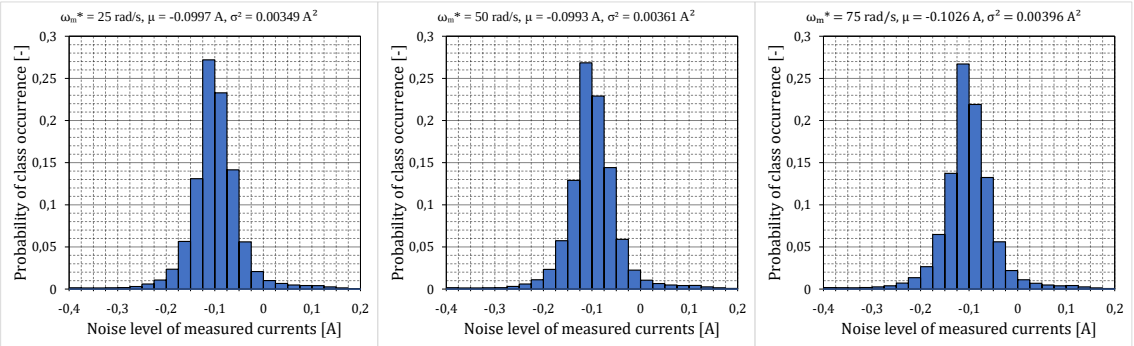

Fig. 4.1: Histograms of measured random noise; connection: $n_p = 1$, $n_s = 3$

As shown in Figure 4.1, the random noises contain the non-zero mean value. This offset is probably caused by converting the numbers obtained by the analog-digital converters to currents inside the processor. According to the algebra of random variables [29], the mean value of the sum of noises μ is obtained as in

$$\mu = \mu_a + \mu_b + \mu_c \tag{4.16}$$

where μ_a, μ_b, and μ_c are the mean values of random variables $\varepsilon_{a,n}$, $\varepsilon_{b,n}$, and $\varepsilon_{c,n}$. Since $\mu \neq 0$, there is a high probability that $\mu_a \neq 0$, $\mu_b \neq 0$, and $\mu_c \neq 0$. Therefore, the DC offset is most likely propagated into the stator reference frame, yielding

$$\begin{bmatrix} \mu_\alpha \\ \mu_\beta \end{bmatrix} = \frac{2}{3} \begin{bmatrix} 1 & -\frac{1}{2} & -\frac{1}{2} \\ 0 & \frac{\sqrt{3}}{2} & -\frac{\sqrt{3}}{2} \end{bmatrix} \cdot \begin{bmatrix} \mu_a \\ \mu_b \\ \mu_c \end{bmatrix}. \tag{4.17}$$

Similarly, the variances σ_a^2, σ_b^2, and σ_c^2 of random variables $\varepsilon_{a,n}$, $\varepsilon_{b,n}$, and $\varepsilon_{c,n}$ are transformed into the stator reference frame as in

$$\begin{bmatrix} \sigma_\alpha^2 \\ \sigma_\beta^2 \end{bmatrix} = \frac{4}{9} \begin{bmatrix} 1 & \frac{1}{4} & \frac{1}{4} \\ 0 & \frac{3}{4} & \frac{3}{4} \end{bmatrix} \cdot \begin{bmatrix} \sigma_a^2 \\ \sigma_b^2 \\ \sigma_c^2 \end{bmatrix}. \tag{4.18}$$

If it is assumed that $\sigma_a^2 = \sigma_b^2 = \sigma_c^2 = \sigma^2/3$, then the errors propagated to the stator reference frame have the following variances: $\sigma_\alpha^2 = \frac{2}{9}\sigma^2$ and $\sigma_\beta^2 = \frac{2}{9}\sigma^2$. Therefore, according to histograms in Figure 4.1, the random noise component is modeled as the normally distributed random number with the variance of $1 \cdot 10^{-3}$. The mean value of the modeled noise is biased according to equations (4.16) and (4.17).

Another factor that causes a significant problem in parametric estimation is the presence of periodic distortions $\varepsilon_{a,p}$, $\varepsilon_{b,p}$, and $\varepsilon_{c,p}$. For example, the electrical parameters are not concentrated and might slightly differ in each winding slot. Same for the contributions of permanent magnets. Therefore, there is significant distortion in frequency $\omega_m = \omega_e/p$, where p is the number of pole pairs. Such distortion can be seen in the fault current waveform in Figure 2.8. Another source of periodic fluctuations is an inverter's nonlinearity. As mentioned by Buchta in [30] the distortion caused by the inverter can be modeled as follows:

$$\begin{bmatrix} \Delta_{u,a} \\ \Delta_{u,b} \\ \Delta_{u,c} \end{bmatrix} = u_{dead} \begin{bmatrix} \frac{2}{3} & -\frac{1}{3} & -\frac{1}{3} \\ -\frac{1}{3} & \frac{2}{3} & -\frac{1}{3} \\ -\frac{1}{3} & -\frac{1}{3} & \frac{2}{3} \end{bmatrix} \cdot \begin{bmatrix} \text{sign}(i_a) \\ \text{sign}(i_b) \\ \text{sign}(i_c) \end{bmatrix} \tag{4.19}$$

where $\Delta_{u,a}$, $\Delta_{u,b}$, and $\Delta_{u,c}$ are contributions to the required stator voltages, and u_{dead} is the dead time voltage that reflects voltage drops on the switches of the inverter. If (4.19) is expressed in the stator reference frame using the trigonometric series, the periodic distortions are obtained as in

$$\begin{aligned} \Delta_{u,\alpha} &= u_{dead}\frac{4}{\pi}(\sin(\theta_e) + S_\alpha) \\ \Delta_{u,\beta} &= -u_{dead}\frac{4}{\pi}(\cos(\theta_e) + S_\beta) \end{aligned} \tag{4.20}$$

where

$$S_\alpha = \sum_{n=1}^{\infty} \left(\frac{\sin((6n-1)\theta_e)}{6n-1} + \frac{\sin((6n+1)\theta_e)}{6n+1} \right)$$
$$S_\beta = \sum_{n=1}^{\infty} \left(\frac{\cos((6n-1)\theta_e)}{6n-1} + \frac{\cos((6n+1)\theta_e)}{6n+1} \right). \tag{4.21}$$

Since a machine follows linear model (4.4), the same frequencies as in (4.20) and (4.21) are propagated to the stator reference frame currents. It was estimated that the dead time voltage u_{dead} is equal to $0.02\,V$ in the case of the motor used for algorithm validation.

Since the frequency of the stator reference frame signals is estimated by the angle tracking observer (Section 2.3) in the control system, band-pass filtering is the most straightforward way to deal with the DC offset and periodic distortions. Generally, the transfer function of the band-pass filter can be defined as in

$$F_{filt}(s) = \frac{Y(s)}{U(s)} = \frac{2\zeta\omega_r s}{s^2 + 2\zeta\omega_r s + \omega_r^2} \tag{4.22}$$

where ω_r is the reference frequency, ζ stands for the damping ratio, and $U(s)$ and $Y(s)$ are the input and output of the filter expressed in Laplace transform. The passing frequency must correspond to the electrical angular velocity, yielding the value $\omega_r = \omega_e(k)$ adapted in each step. The damping ratio is adjusted to achieve suitable suppression of higher spectrum components. The calculated value $\zeta = 0.3$ ensures that the frequencies $\omega_e/5$ and $5\omega_e$ are suppressed by approximately $18\,dB$. Transfer function (4.22) is then discretized resulting in the following expression:

$$y(k+1) = b(k)(u(k) - u(k-1)) + a_1(k)y(k) + a_2(k)y(k-1) \tag{4.23}$$

where $u(k)$ and $y(k)$ are the filter input and output expressed in time-domain and adapted coefficients $b(k)$, $a_1(k)$, and $a_2(k)$ are calculated as in

$$b(k) = 2\frac{\zeta}{\sqrt{1-\zeta^2}} e^{-\zeta\omega_e(k)T_s} \sin(\omega_e(k)T_s\sqrt{1-\zeta^2})$$
$$a_1(k) = 2e^{-\zeta\omega_e(k)T_s} \cos(\omega_e(k)T_s\sqrt{1-\zeta^2})$$
$$a_2(k) = -e^{-2\zeta\omega_e(k)T_s}. \tag{4.24}$$

Note that this filter does not entirely suppress the inverter's nonlinearity since the distortion contains a component with frequency ω_e. Therefore, the estimated parameters are always biased. However, due to the low level of dead time voltage u_{dead}, the bias is not so significant. The advantage of signals filtering is suppressing the DC component and distortion on frequency ω_m. The fault relevance diagnostic algorithm presented in Section 4.1 is then extended by adaptive filters as follows:

1. Update filter coefficients (4.24).
2. Filter the signals u_β, i_β, and $\sin(\theta_e)$ by the adaptive filters (4.23).
3. Update the estimation of healthy parameters (4.5).
4. Calculate input and output transformation (4.7).
5. Filter the transformed input v and output y by the adaptive filters (4.23).
6. Update the estimation of ITF parameters (4.9).
7. Calculate series resistance R_s (4.6).
8. Evaluate $R_{f,dq}/x_f^{*2}$ (4.10).
9. Calculate normalized fault relevance $x_{f,n}$ (4.11).

4.3 Parametric estimation

For the purpose of online fault relevance diagnostics, the parameters in equations (4.5) and (4.9) have to be recursively estimated. In the case of healthy parameters (4.5), the persistence of input signals cause trouble with the forgetting factor selection. On the one hand, since the persistence of input signals is insufficient if a machine runs at a constant angular velocity, the forgetting factor has to be 1 to preserve information obtained during transients. On the other hand, the healthy parameters of a real motor are time-variant. For example, the inductances decrease with the growing current due to the saturation effect, or the resistance increases with the rising temperature. Therefore, the forgetting factor must be less than 1 to track these changes correctly. The solution to this situation leads to the variable forgetting factor. In the case of ITF parameters (4.9), if a machine is not shorted, the identified ITF parameters have no meaning and must be quickly forgotten after ITF occurs. Hence, there is a high demand for reliable online adjustment of the forgetting factor. Moreover, the identification algorithm must be calculated under $100\,\mu s$ on AURIX application kit TC277. The defined requirements are perfectly satisfied by the regularized parametric estimation algorithm described by Dokoupil in [31].

As mentioned in [31], the presented estimation strategy expands on the classical recursive least squares method [27] by designing a data-driven forgetting strategy that operates in synergy with the variable regularization. The regularization is conceived to employ the previous parameter estimate to stabilize the updated one via retention of the externally supplied information. The soft equality constraints on the regression parameters Ξ (where Ξ is some real regular square matrix with a dimension corresponding to the number of identified parameters) are then incorporated into the learning procedure to smooth the parameter estimate. Generally, the algorithm contains the data-updating steps, forgetting factor adjustment, and time-updating steps. During the data-updating steps, the variables that transmit

information between the previous and actual time steps $f(k, k-1)$ are updated in terms of transmitted data $f(k, k-1) \rightarrow f(k, k)$. An example of such variables is the number of degrees of freedom $\nu(k, k-1)$ (scalar variable) or the least squares reminder $\Sigma(k, k-1)$ (scalar variable), representing the estimated minimum of a quadratic criterion. Note that $\Sigma(k, k-1)$ and $\nu(k, k-1)$ are the required statistics of normal-Wishart probability distribution. The forgetting factor adjustment $\lambda(k, k-1) \rightarrow \lambda(k+1, k)$ is then based on the Kullback-Leibler divergence between two normal-Wishart probability density functions, where one is described by the previous step statistics $\Sigma(k, k-1)$ and $\nu(k, k-1)$ and the other by the data-updated statistics $\Sigma(k, k)$ and $\nu(k, k)$. Therefore, if a rapid parameter change occurs, it is quickly reflected by the least squares reminder $\Sigma(k, k)$ and thus by the Kullback-Leibler divergence. In the last algorithm part, the data-transmitting variables are updated in terms of time $f(k, k) \rightarrow f(k+1, k)$. Hence, some of the information passed to the next step is forgotten based on the currently calculated forgetting factor $\lambda(k+1, k)$.

During the data-updating steps, firstly, the update of the projection matrix $\mathbf{P}(k, k)$ is calculated. The projection matrix is not propagated to the next step in the implemented algorithm version; instead, the information matrix $\mathbf{V}(k, k-1)$, which represents the inversion of the normalized projection matrix, is passed. The projection matrix data update $\mathbf{P}(k, k)$ is then calculated using the information matrix $\mathbf{V}(k, k-1)$. We have

$$\begin{aligned}
\mathbf{P}_c^{-1}(k, k-1) &= \mathbf{V}(k, k-1) + (1 - \lambda(k, k-1))\Xi \\
\mathbf{V}(k, k) &= \mathbf{P}_c^{-1}(k, k-1) + \mathbf{h}(k) \cdot \mathbf{h}^T(k) \\
\mathbf{K}(k) &= \mathbf{P}_c(k, k-1) \cdot \mathbf{h}(k) / (1 + \mathbf{h}^T(k) \cdot \mathbf{P}_c(k, k-1) \cdot \mathbf{h}(k)) \\
\mathbf{P}(k, k) &= (\mathbf{I} - \mathbf{K}(k) \cdot \mathbf{h}^T(k)) \cdot \mathbf{P}_c(k, k-1) \cdot (\mathbf{I} - \mathbf{K}(k) \cdot \mathbf{h}^T(k))^T + \\
&\quad + \mathbf{K}(k) \cdot \mathbf{K}^T(k)
\end{aligned} \tag{4.25}$$

where $\mathbf{I}$ is the identity matrix of dimension corresponding to the number of identified parameters and $\mathbf{h}(k)$ stands for the column regression vector. Note that the constrained terms Ξ realize penalization in information matrix $\mathbf{V}(k, k)$. If the rapid change of forgetting factor occurs, it is reflected in the information matrix and thus in the projection matrix $\mathbf{P}(k, k)$. In subsequent algorithm part, the column vector of parameters estimated in the previous step $\Theta(k, k-1)$ is penalized based on the constrained terms Ξ and the old estimation of parameters $\Theta(k-1, k-2)$, yielding

$$\begin{aligned}
\varepsilon(k) &= \Theta(k, k-1) - \Theta(k-1, k-2) \\
\Theta_c(k, k-1) &= \Theta(k, k-1) + \mathbf{P}_c(k, k-1) \cdot \Xi \cdot \varepsilon(k).
\end{aligned} \tag{4.26}$$

As seen in (4.26), the changes in estimated parameters between the two steps are more penalized by the higher values in matrix Ξ. Then the penalized estimated

parameters $\Theta_c(k, k-1)$ are applied to determine the parameters in the recent step $\Theta(k, k)$ as in

$$\begin{aligned} \hat{e}_c(k, k-1) &= y(k) - \mathbf{h}^T(k) \cdot \Theta_c(k, k-1) \\ \Theta(k, k) &= \Theta_c(k, k-1) + \mathbf{K}(k) \cdot \hat{e}_c(k, k-1) \end{aligned} \tag{4.27}$$

where $y(k)$ is the measured system output in the recent step and $\hat{e}_c(k, k-1)$ is the estimated model error. At the end of the data-updating steps, the normal-Wishart distribution statistics ($\nu(k, k)$ and $\Sigma(k, k)$) are actualized based on the estimated error $\hat{e}_c(k, k-1)$. We have

$$\begin{aligned} \nu(k, k) &= \nu(k, k-1) + 1 \\ \Sigma_c(k, k-1) &= \Sigma(k, k-1) - \varepsilon^T(k) \cdot (\Xi + \Xi \cdot \mathbf{P}_c(k, k-1) \cdot \Xi) \cdot \varepsilon(k) \\ \Sigma(k, k) &= \Sigma_c(k, k-1) + \hat{e}_c^2(k, k-1)/(1 + \mathbf{h}^T(k) \cdot \mathbf{P}_c(k, k-1) \cdot \mathbf{h}(k)). \end{aligned} \tag{4.28}$$

Note that the least squares reminder $\Sigma(k, k-1)$ is firstly actualized based on the penalization of parameters changes $\Sigma(k, k-1) \to \Sigma_c(k, k-1)$, and then the data update is calculated $\Sigma_c(k, k-1) \to \Sigma(k, k)$.

During the forgetting factor adjustment, the estimations of system noise variance in the previous step $\hat{d}(k, k-1)$ and the data-updated step $\hat{d}(k, k)$ are calculated together with the changes of data-updated parameters $\varepsilon(k+1)$ as follows:

$$\begin{aligned} \hat{d}(k, k-1) &= \nu(k, k-1)/\Sigma(k, k-1) \\ \hat{d}(k, k) &= \nu(k, k)/\Sigma(k, k) \\ \varepsilon(k+1) &= \Theta(k, k) - \Theta(k, k-1). \end{aligned} \tag{4.29}$$

Then the Kullback-Leibler divergence is evaluated as in

$$\begin{aligned} X_\zeta = \operatorname{trace}(\mathbf{V}(k, k-1) \cdot \mathbf{P}(k, k)) + \nu(k, k-1) \ln \left(\frac{\hat{d}(k, k-1)}{\hat{d}(k, k)} \right) + \\ + \hat{d}(k, k)\Sigma(k, k-1) + \zeta \hat{d}(k, k) \varepsilon^T(k+1) \cdot \mathbf{V}(k, k-1) \cdot \varepsilon(k+1) + \\ + \frac{\nu(k, k-1)}{\nu(k, k)} - \nu(k, k-1) \end{aligned} \tag{4.30}$$

where $\operatorname{trace}(\mathbf{X})$ stands for the trace of square matrix $\mathbf{X}$ and ζ is user-defined scalar constant. This constant represents an artificial increase in the expected noise level and reduces false detected changes of parameters caused by the system noise. The higher the value of $\zeta \in (0, 1\rangle$, the more prediction error is reflected in the new value of the forgetting factor. The forgetting factor $\lambda(k, k-1)$ is then updated based on the calculated divergence X_ζ and number of identified parameters n. The limitation

of the forgetting factor $\lambda(k+1,k) \in \langle \alpha, 1\rangle$ is implemented using the $if-else$ conditioning to achieve only the valid values of $\lambda(k+1,k)$. We have

$$\begin{array}{lcl}
\textbf{if} & 1 \leq X_\zeta \alpha/((n+1)\lambda(k,k-1)) & \textbf{then} \\
 & \lambda(k+1,k) = \alpha & \\
\textbf{else if} & 1 \geq X_\zeta/((n+1)\lambda(k,k-1)) & \textbf{then} \\
 & \lambda(k+1,k) = 1 & \\
\textbf{else} & & \\
 & \lambda(k+1,k) = (n+1)\lambda(k,k-1)/X_\zeta & \\
\textbf{end if} & &
\end{array} \tag{4.31}$$

where the lower bound of the forgetting factor α lies on the interval $\alpha \in (0,1)$.

During the time-updating steps, the data-updated parameters are actualized in terms of exponential forgetting, yielding

$$\begin{array}{ll}
\mathbf{V}(k+1,k) = \lambda(k+1,k)\mathbf{V}(k,k) & \Sigma(k+1,k) = \lambda(k+1,k)\Sigma(k,k) \\
\Theta(k+1,k) = \Theta(k,k) & \nu(k+1,k) = \lambda(k+1,k)\nu(k,k).
\end{array} \tag{4.32}$$

Similarly, for the purpose of the covariance checking, the projection matrix might be time-updated as well $\mathbf{P}(k+1,k) = \mathbf{P}(k,k)/\lambda(k+1,k)$. However, since the projection matrix presented in the explained algorithm represents the normalized values, it must be denormalized as in $\mathbf{P}_M(k+1,k) = \mathbf{P}(k+1,k)/\hat{d}(k,k)$ to achieve real covariance values. The recursive parametric estimation algorithm then periodically calculates the following steps:

1. Obtain inputs $[\mathbf{V}(k,k-1);\ y(k);\ \mathbf{h}(k);\ \Theta(k,k-1);\ \Theta(k-1,k-2);$ $\Sigma(k,k-1);\ \nu(k,k-1);\ \lambda(k,k-1)]$.
2. Load constants out of memory $[\Xi;\ \zeta;\ n;\ \alpha]$.
3. Execute the data-updating steps in the following order: (4.25), (4.26), (4.27), and (4.28).
4. Update the forgetting factor in the following order: (4.29), (4.30), and (4.31).
5. Calculate the time updates (4.32).
6. Write outputs $[\mathbf{V}(k+1,k);\ \Theta(k+1,k);\ \Sigma(k+1,k);\ \nu(k+1,k);\ \lambda(k+1,k)]$.

The proper operation of the described algorithm is achieved only if the following initial conditions are chosen: $\mathbf{V}(1,0) = \Xi$, $\Sigma(1,0) > 0$, $\nu(1,0) > 0$, and $\lambda(1,0) = 1$. To reduce parameters oscillations at the beginning of the identification procedure, it is also essential to fill the regression vector $\mathbf{h}(k)$ first and initialize the estimated parameters as in $\Theta(0,-1) = \Theta(1,0)$.

4.4 Implementation of the diagnostic algorithm

The fault relevance diagnostic algorithm described in Section 4.1 and extended by the adaptive band-pass filters in Section 4.2 is realized in MATLAB Simulink, as shown in Figure 4.2.

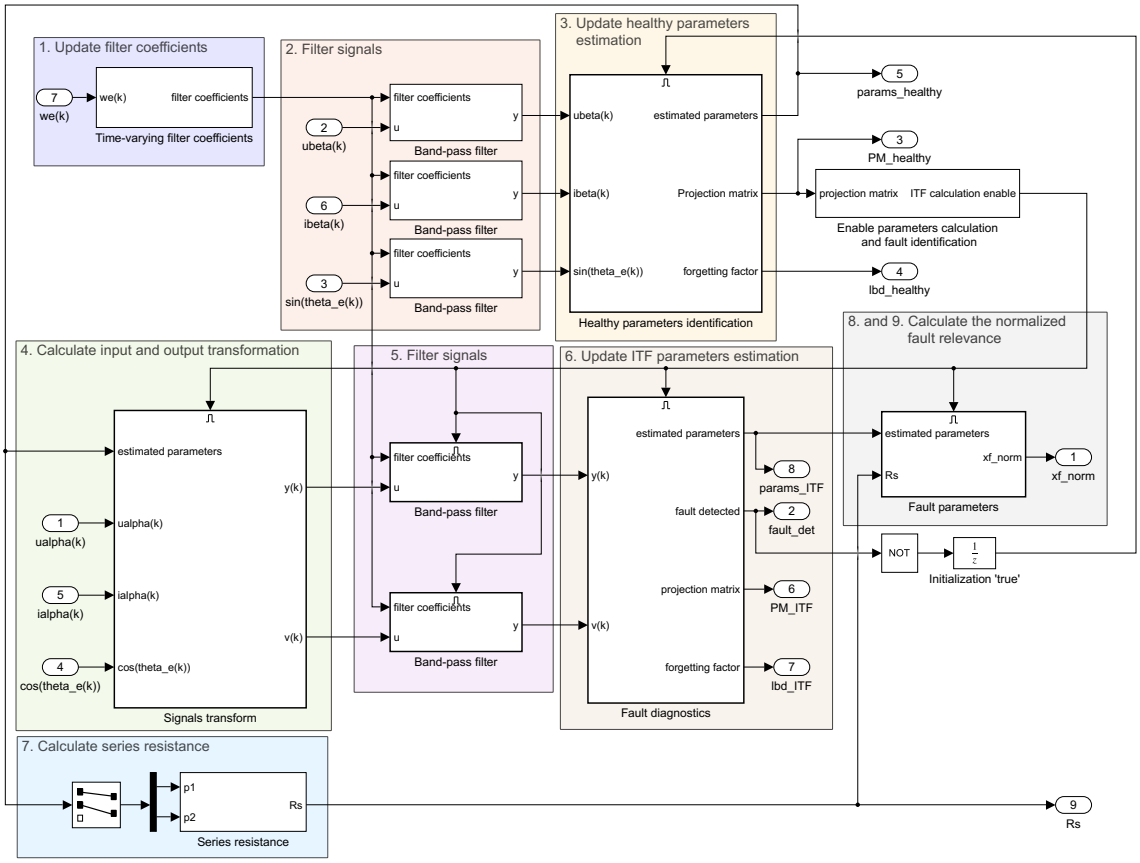

Fig. 4.2: Implementation of the diagnostic algorithm in MATLAB Simulink

Furthermore, as seen in Figure 4.2, the enabled subsystems are incorporated into the described algorithm since there is no reason to calculate ITF parameters estimation unless the healthy parameters are identified with sufficient precision. Enabling is then realized based on the covariance of healthy parameters. Figure 4.3 visualizes the implemented covariance checking.

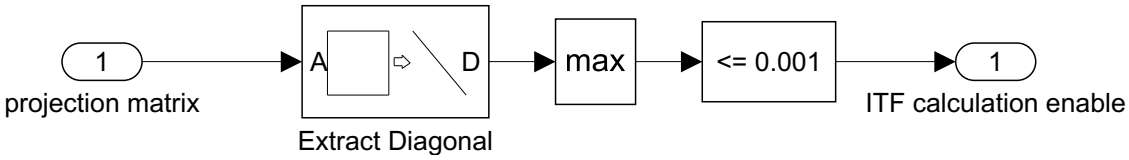

Fig. 4.3: Checking the covariance of healthy parameters

Another enabling is realized in healthy parameters estimation. Since the real behavior is not as idealized as the model describes, the fault also slightly affects the healthy parameters. Therefore, identifying the healthy parameters is turned off after the inter-turn short circuit is detected. The fault is detected by reaching the lower forgetting factor bound in the ITF parameters estimation algorithm. Adaptive signals filtering is then realized according to equations (4.23) and (4.24).

The implementation of recursive healthy parameters identification can be seen in Figure 4.4.

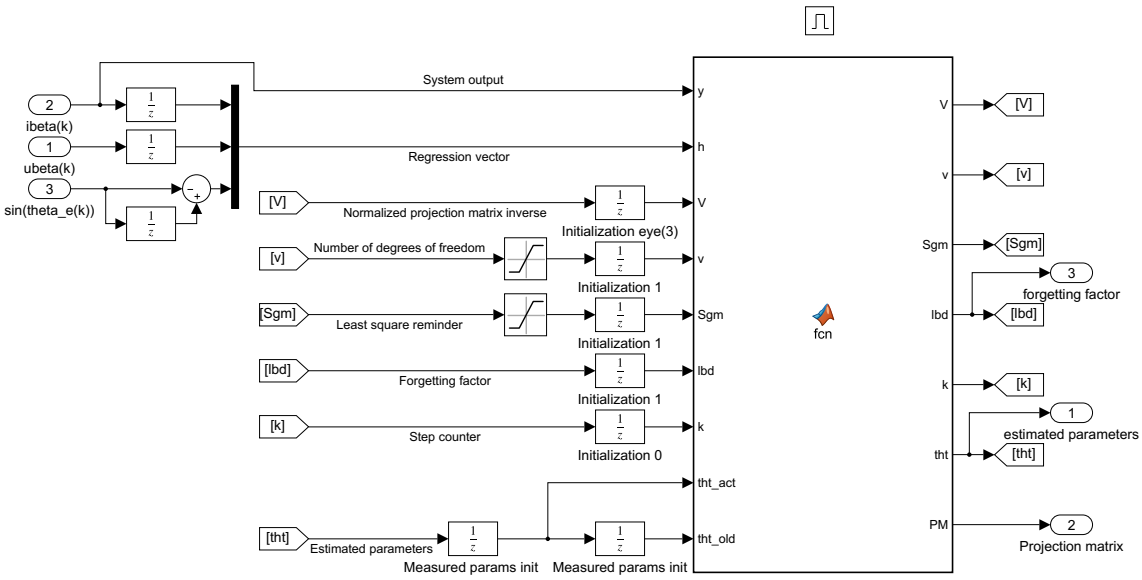

Fig. 4.4: Healthy parameters estimation in MATLAB Simulink

Theoretically, the number of degrees of freedom ν and the least squares reminder Σ can grow to infinity. Therefore, they are saturated between 0 and 10^5 (Figure 4.4). For the purpose of regression vector filling up, the step counter k is also present. Parametric estimation is then started after three steps to ensure that all delays are reflected. Initial values of variables required in the parametric estimation algorithm are presented under the unit delay blocks in Figure 4.4. If they are not mentioned, the initial condition is a scalar value equal to 0. Estimated parameters are initialized based on Table 1.2 and equation (4.6). The lower bound of the forgetting factor is $\alpha = 0.95$ to track changes in electrical parameters with the operating point. Constrained terms Ξ correspond to the identity matrix. This value enables effective tracking of parameters changes and ensures relatively smooth evolution of parameters in time. User-defined parameter ζ is then set to be 0.05. The low value of ζ helps to smooth the forgetting factor, which is welcome since the persistence of input signals is mostly insufficient. The parametric estimation algorithm is then implemented using the MATLAB function block as follows:

Listing 4.1: Parametric estimation algorithm realized as a MATLAB function

```
function [V,v,Sgm,lbd,k,tht,PM]  = fcn(y,h,V,v,Sgm,k,...
                                   lbd,tht_act,tht_old)
% Constant parameters:
n = 3; Xi = eye(n); alpha = 0.95; zeta = 0.05;
del = 3; I = eye(n);
if (k<del)
    k = k + 1; tht = tht_act; PM = eye(n);
else
    % Data-updating steps:
    V_old = V; Sgm_old = Sgm; v_old = v;
    V = V_old + (1-lbd)*Xi + h*h';
    Pc = (V_old + (1-lbd)*Xi)^(-1);
    K = Pc*h/(1 + h'*Pc*h);
    P = (I-K*h')*Pc*(I-K*h')' + K*K';
    eps = tht_act - tht_old;
    thtc = tht_act + Pc*Xi*eps;
    ec = y - h'*thtc;
    Sgmc = Sgm - eps'*(Xi + Xi*Pc*Xi)*eps;
    Sgm = Sgmc + ec^2/(1+h'*Pc*h);
    v = v + 1;
    tht = thtc + K*ec;
    % Forgetting factor adjustement:
    d_old = v_old/Sgm_old; d = v/Sgm;
    eps_new = tht - tht_act;
    Xz = trace(V_old*P)+v_old*log(d_old/d)+d*Sgm_old...
         +d*eps_new'*zeta*V_old*eps_new+v_old/v-v_old;
    if (1 <= Xz*alpha/(lbd*(n+1))), lbd = alpha;
    elseif (1 >= Xz/(lbd*(n+1))), lbd = 1;
    else, lbd = lbd*(n+1)/Xz;
    end
    % Time-updating steps:
    V = V*lbd; Sgm = Sgm*lbd; v = v*lbd;
    % Denormalized projection matrix:
    PM = (P/lbd)/d;
end
```

Note that the denormalized projection matrix is sent to the output and provides the information about covariance necessary for the ITF parameters estimation enabling.

Similarly, the recursive identification of ITF parameters is shown in Figure 4.5.

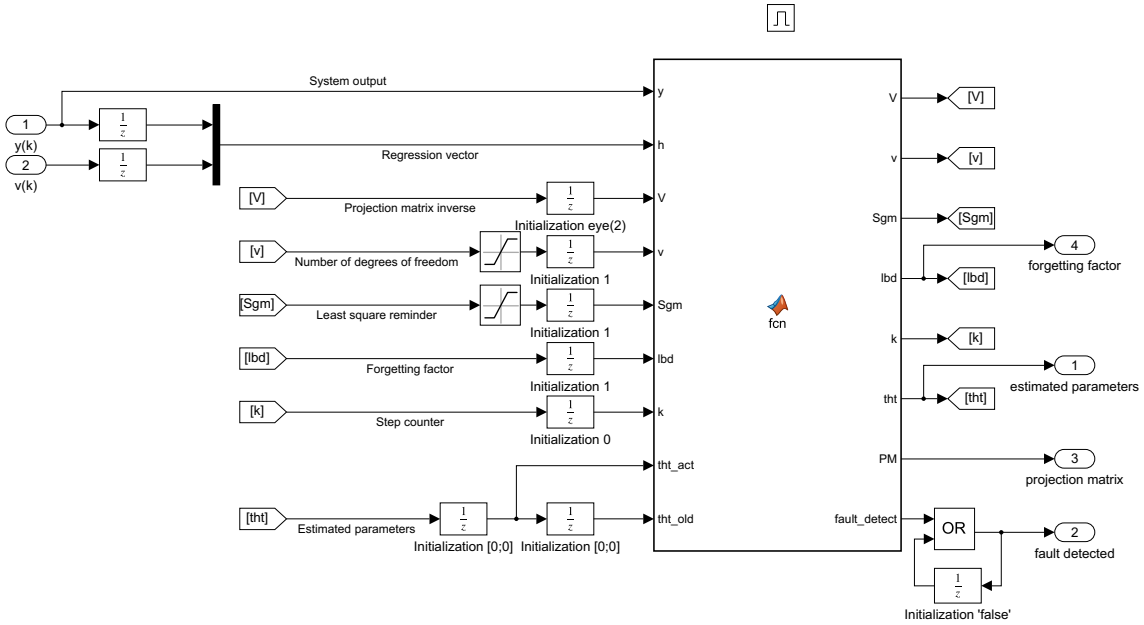

Fig. 4.5: ITF parameters estimation in MATLAB Simulink

The differences between the recursive estimation of healthy (Figure 4.4) and ITF (Figure 4.5) parameters lie in different lower bounds of forgetting factor α, numbers of identified parameters n, user-defined factors ζ, and the initial delays before the algorithm is started. Identifying two ITF parameters is started after four steps in the wake of reaching the required covariance of healthy parameters. This value reflects especially the delays caused by the input and output transformation (4.7). The lower bound of the forgetting factor α is then set to be 0.6. If α is reached, then to improve the learning of actual ITF parameters, the algorithm is reset, and one additional logical output indicates that the fault was detected. This is realized by the following code inserted after line 35 of Listing 4.1:

Listing 4.2: Reset of recursive identification of ITF parameters

```
1 fault_detect = false;
2 if (lbd==alpha)
3     Sgm = 1; v = 1; V = eye(n); lbd = 1; tht = tht_act;
4     PM = eye(n); fault_detect = true;
5 end
```

If the logical value 'true' of $fault\_detect$ is reached, it is held using a simple flip-flop (Figure 4.5), and the recursive updating of healthy parameters is switched off (Figure 4.2). In the case of ITF parametric estimation, the user-defined factor ζ is equal to 0.5 to achieve faster forgetting factor changes at the expense of smoothness. The constrained terms Ξ are similarly given by the identity matrix.

The calculation of series resistance and normalized fault relevance is then extended by conditions that prevent reaching undefined values (for example, caused by dividing numbers by 0). These conditions are visualized in Figure 4.6.

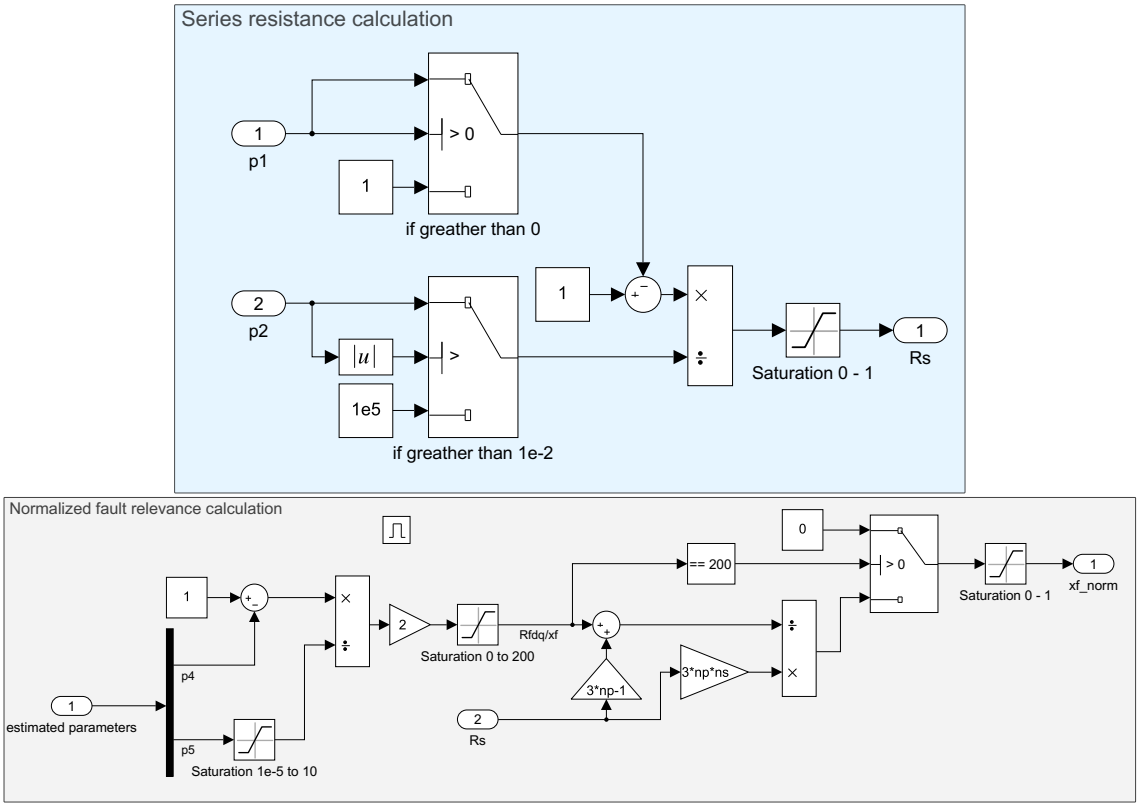

Fig. 4.6: Calculation of series resistance and normalized fault relevance

As shown in Figure 4.6, the series resistance and normalized fault relevance are saturated between 0 and 1. The limitation of normalized fault relevance is straightforward since this parameter can achieve only values between 0 and 1. The series resistance is then saturated based on the initial estimation (Table 1.2) to prevent reaching highly overrated values. Since the band-pass filter filters the input signals of the ITF parameters estimation algorithm, there is always some harmonic signal (even if the short circuit is not emulated) that causes the estimation of low-level fault relevance. Therefore, if the fault relevance reaches the defined value given by saturation of $R_{f,dq}/x_f^{*2}$, the output normalized fault relevance is set to be 0.

4.5 Diagnostics verification within the simulation

The algorithm described in the previous sections is firstly evaluated within the simulation. For this purpose, the model visualized in Figure 4.7 is utilized.

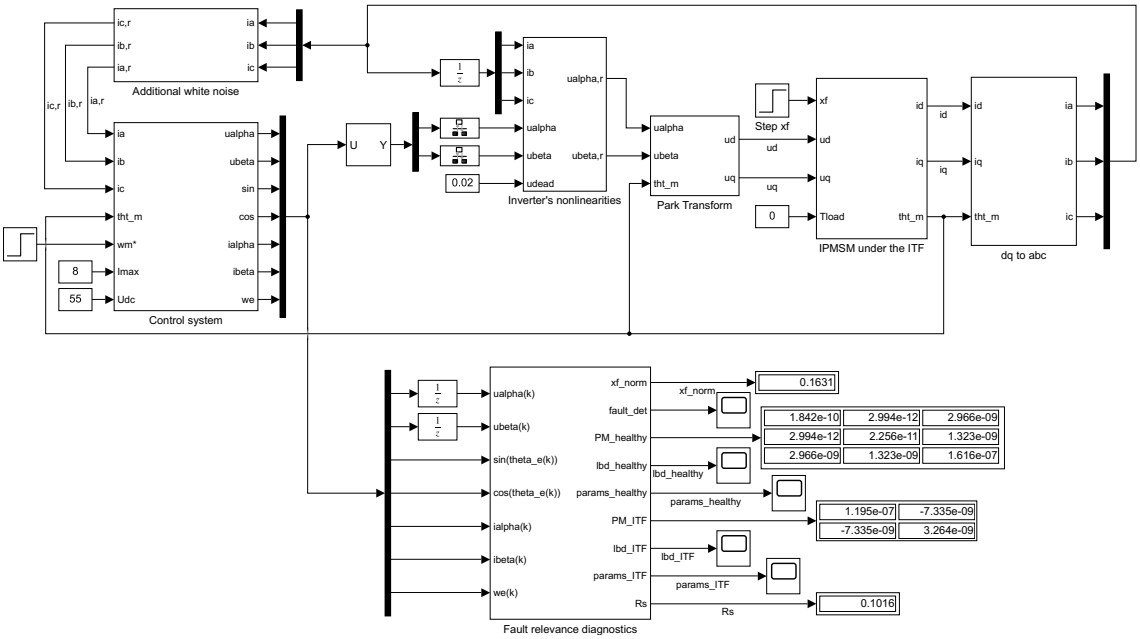

Fig. 4.7: Model for the diagnostics verification within the simulation

The classical control scheme described in the previous chapters is extended by the inverter's nonlinearity (4.20) with the dead time voltage u_{dead} equal to $0.02\,V$. The stator currents are then distorted by additional white noises with the variance of $1 \cdot 10^{-3}$ and randomly selected mean values. The mean values of additional white noises are not so crucial since the adaptive band-pass filter suppresses the DC components of the signals. However, the dead time voltage level noticeably impacts the parameters bias. As mentioned before, the bias is caused by the distortion on frequency ω_e that can not be suppressed since ideal voltage inputs u_α and u_β are harmonic signals of this frequency.

The simulated motor is controlled to the angular velocity setpoint $\omega_m^* = 75\,rad/s$, and after six seconds, inter-turn short circuits are simulated in phase 'a' with different fault relevance: $x_f = 4/25$, $x_f = 6/25$, $x_f = 9/25$, and $x_f = 14/25$. These experiments are realized only for the winding connection $n_p = 1$ and $n_s = 3$. The torque load connected to the shaft of the simulated machine is equal to 0 to achieve the minimum signal-to-noise ratio. If the higher value of torque load is present, the amplitudes of currents are growing, and the signal-to-noise ratio is higher. Signals for the fault relevance estimation are then obtained from the control system, and the diagnostic algorithm starts in time $0\,s$ with the velocity step request.

Figure 4.8 visualizes the estimated healthy parameters and calculated series resistance.

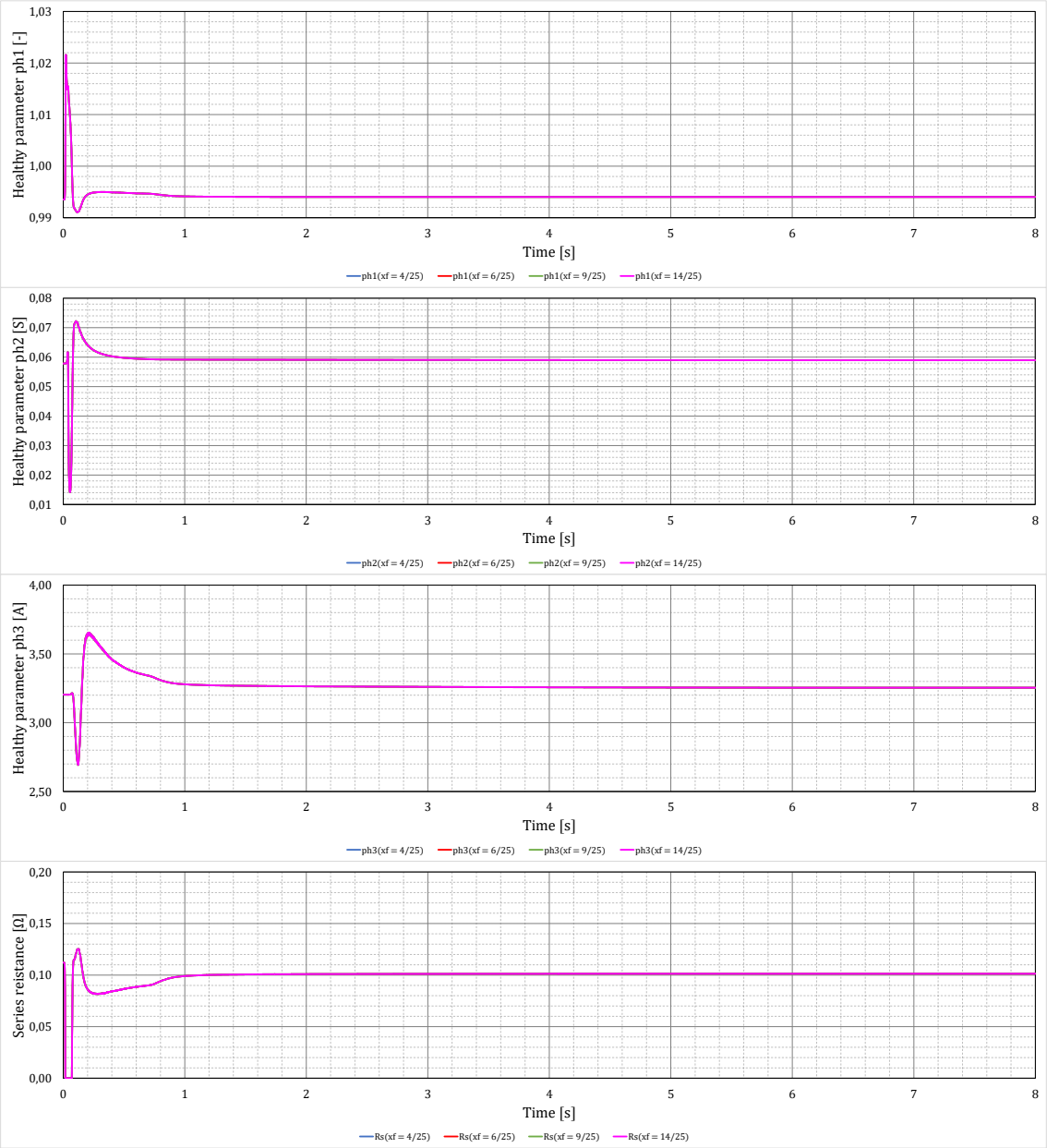

Fig. 4.8: Estimated healthy parameters and series resistance, simulation

Since the identification algorithm is robustly tuned and the simulated electrical parameters are constant, the calculated forgetting factor equals 1 in each algorithm step. The identified healthy parameters are stabilized after one second of the algorithm run. However, this value is mainly given by the moment of inertia. If less inertia is applied, a machine tracks the velocity setpoint faster, making the frequency sweep more significant. Hence, the input signals have higher persistence resulting in faster stabilization of estimated parameters.

Figure 4.9 then visualizes the time evolution of the ITF parameters.

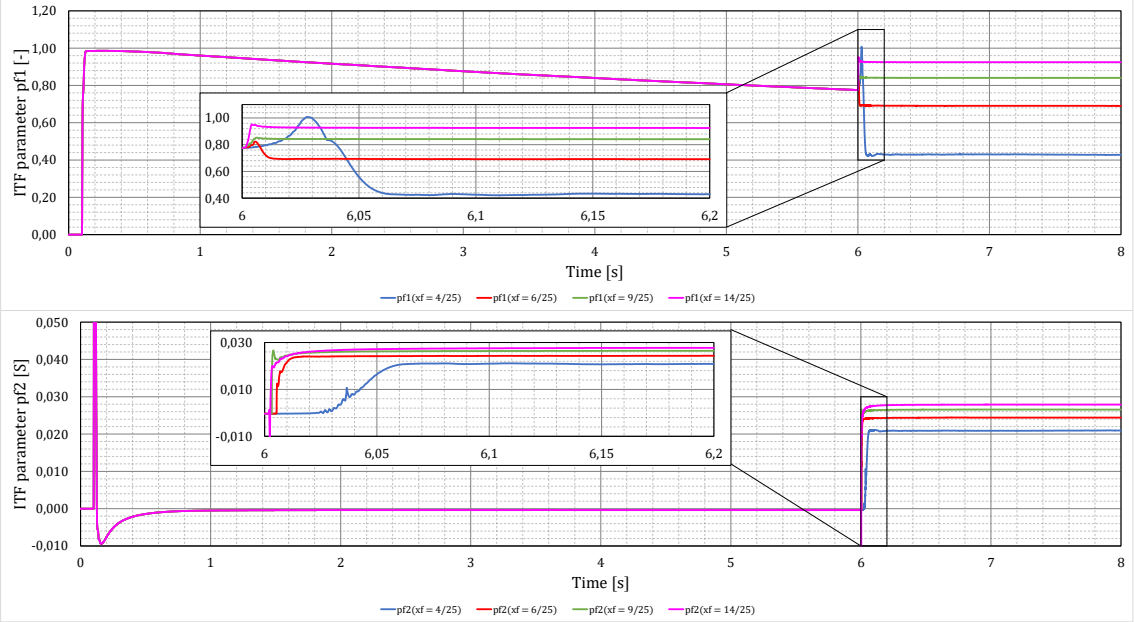

Fig. 4.9: Estimated ITF parameters, simulation

The ITF parameters (Figure 4.9) have no meaning until the short circuit is simulated in time 6 s. After the fault occurs, it is quickly detected by the rapid changes in the forgetting factor, as shown in Figure 4.10.

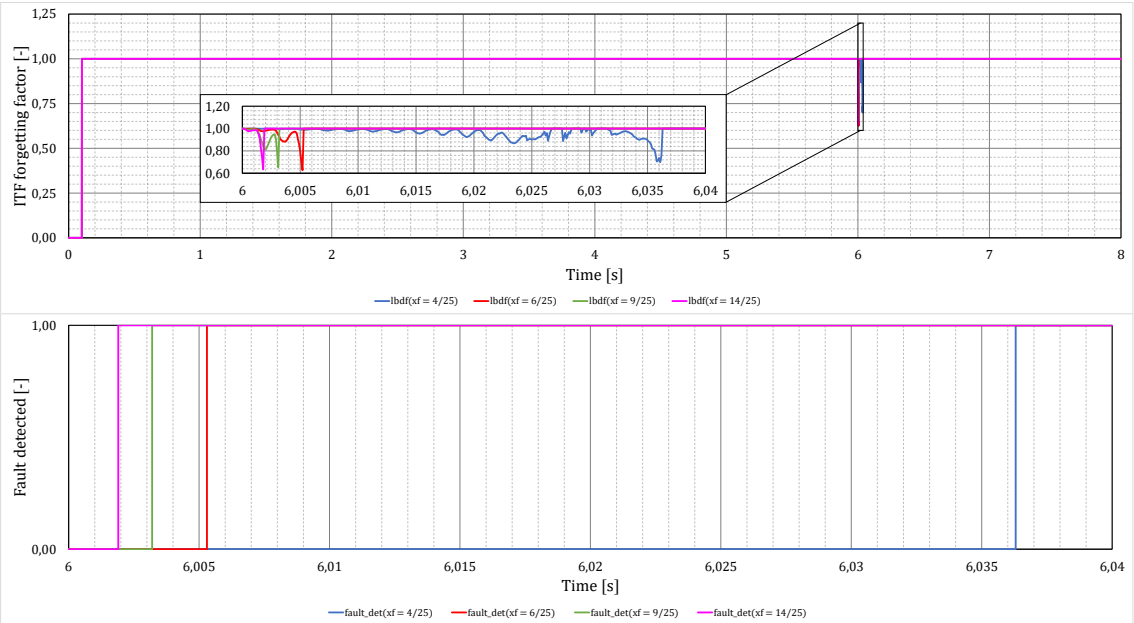

Fig. 4.10: ITF forgetting factor and fault detection, simulation

Generally, the higher values of fault relevance are detected faster than lower ones

due to the higher signal-to-noise ratio of the output signal y obtained by (4.7). The electrical angular velocity of the simulated motor is $1575\,rad/s$, approximately corresponding to the $4\,ms$ electrical period. Hence, the presented algorithm detects higher fault values under one electrical revolution (Figure 4.10). The waveforms of normalized fault relevance can be seen in Figure 4.11.

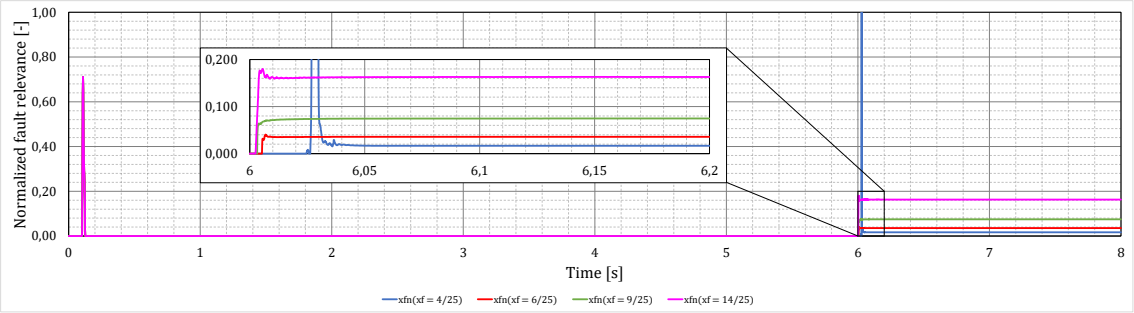

Fig. 4.11: Identified normalized fault relevance, simulation

The estimated normalized fault relevance is then compared with the value calculated by (4.11), assuming the electrical parameters as in Table 1.2. The relative errors are calculated similarly as in (1.33) and presented in the following table:

Tab. 4.1: The error of estimated normalized fault relevance, simulation

x_f [−]	4/25	6/25	9/25	14/25
calculated $x_{f,n}$ [-]	0.0187	0.0397	0.0826	0.1772
estimated $x_{f,n}$ [-]	0.0166	0.0357	0.0748	0.1630
error [%]	11.2	10.1	9.4	8.0

The biased parameters are the primary sources of differences between the estimated and calculated values. For example, the estimated resistance is approximately equal to $0.101\,\Omega$, but the resistance used in the simulation is $0.112\,\Omega$.

4.6 Diagnostics verification on the real motor

Similarly, the diagnostic algorithm is verified on the control system of the experimental motor for the winding connection $n_p = 1$ and $n_s = 3$. A C code is generated from the MATLAB Simulink model of the described algorithm and programmed into AURIX Application kit TC277. Control system is then running in the processor's core 0, and fault diagnostics are running in core 2 (core 1 is used for online communication via ethernet). Short circuits are then emulated with $x_f = 3/25$, $x_f = 6/25$,

$x_f = 9/25$, and $x_f = 14/25$ fault relevance after six seconds from the velocity step request $\omega_m^* = 75\,rad/s$. During this experiment, the machine is disconnected from the dynamometer. Hence, the moment of inertia is lower than the value utilized in simulations, and the torque load equals 0. The time evolution of estimated healthy parameters is visualized in Figure 4.12.

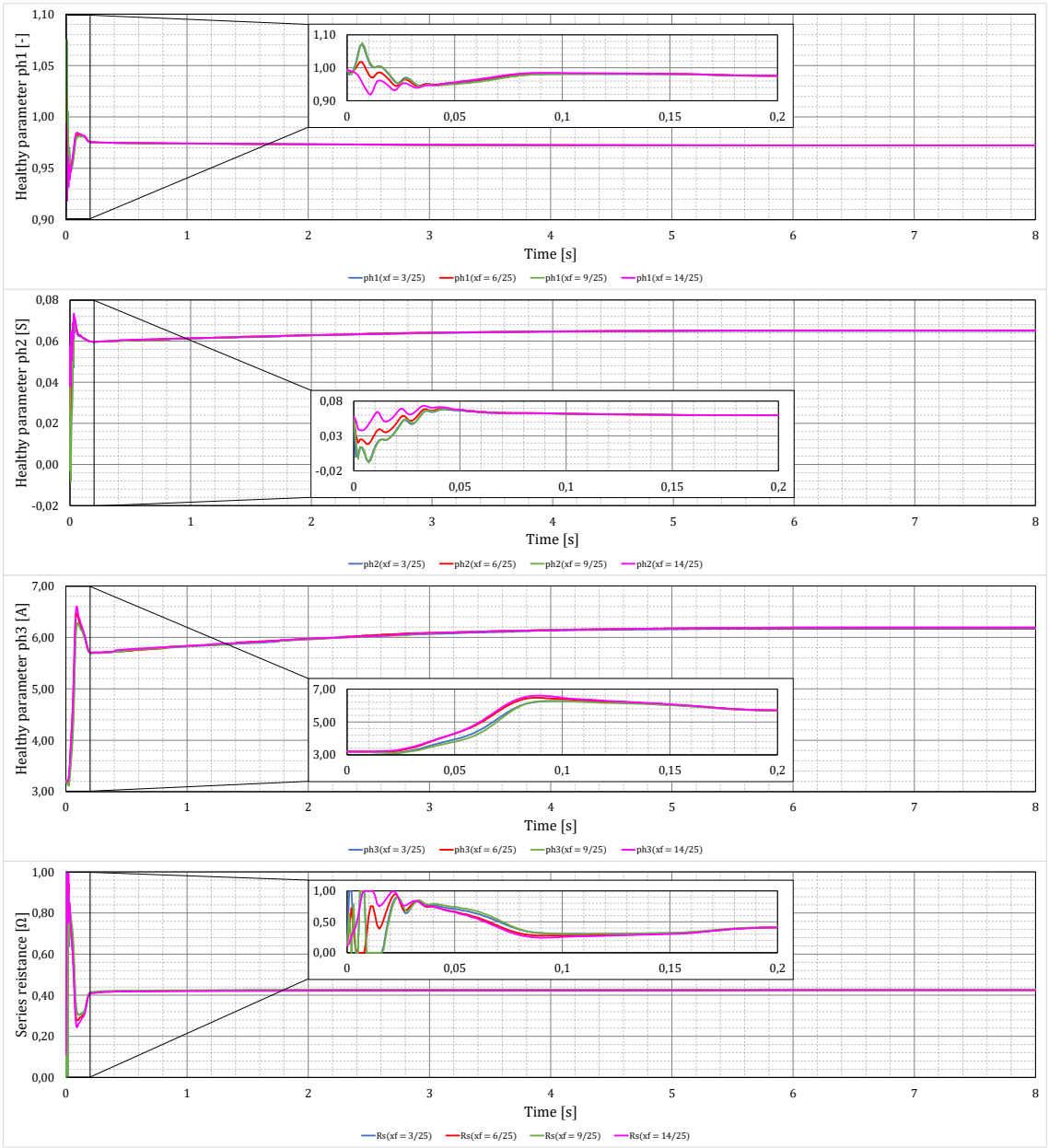

Fig. 4.12: Estimated healthy parameters and series resistance, real motor

In the case of Figure 4.12, the healthy parameters are dependent on the operating point, and the time-variance of parameters (especially of the inductance) is reflected in the estimation. The identified resistance (Figure 4.12) significantly differs from the value implemented in the simulation (Table 1.2) since the model's parameters

were only roughly fit based on the open-loop measurements. The time-varying changes of identified parameters are also reflected in the forgetting factor that is no longer equal to 1 for all the time, as shown in Figure 4.13.

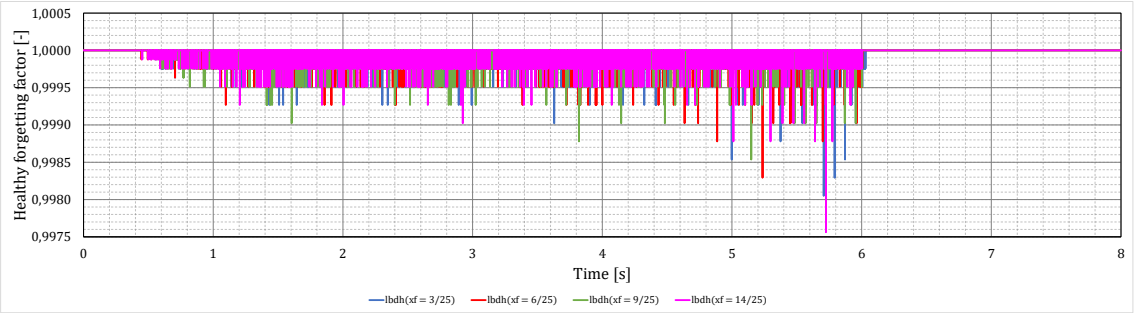

Fig. 4.13: Forgetting factor - healthy parameters estimation, real motor

Note that the forgetting factor is together with the identified healthy parameters held on the last estimated value after the fault is detected.

The estimated ITF parameters are then visualized in Figure 4.14.

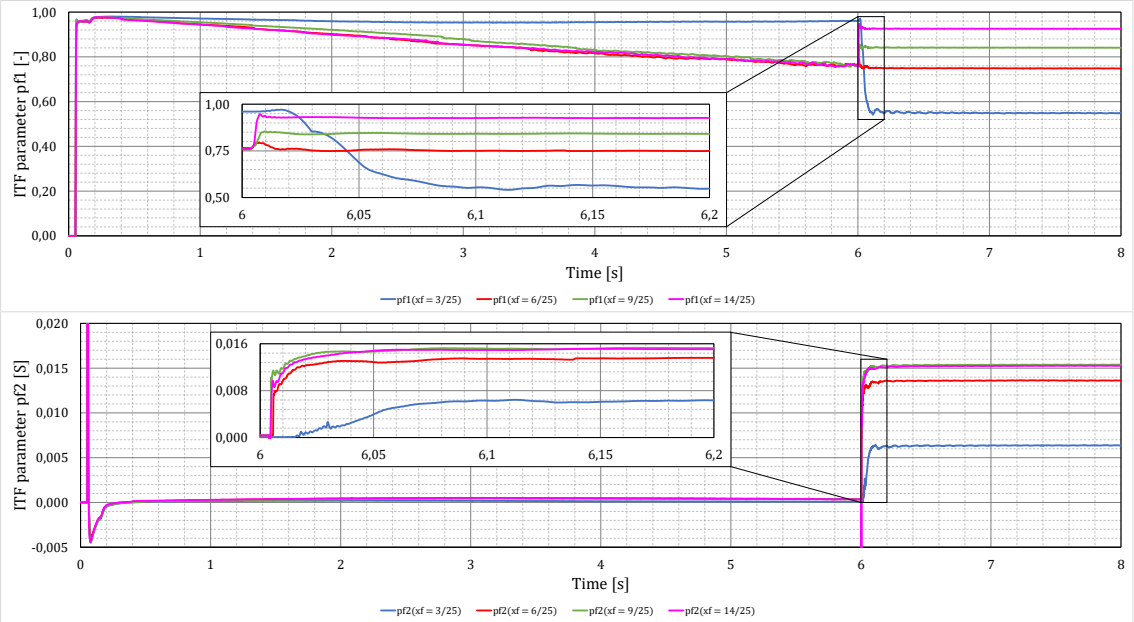

Fig. 4.14: Estimated ITF parameters, real motor

Unlike in case of simulations, the fault is not precisely emulated six seconds after the velocity step request occurs. Inter-turn short circuits are emulated using a relay, and some transport delay is propagated. It was quantified that the fault emulation is approximately delayed by $2\,ms$; however, the precise value of transport delay is unknown. Figure 4.15 then shows the fault detection moments signalized by the processor and the time evolution of the forgetting factor of ITF parameters.

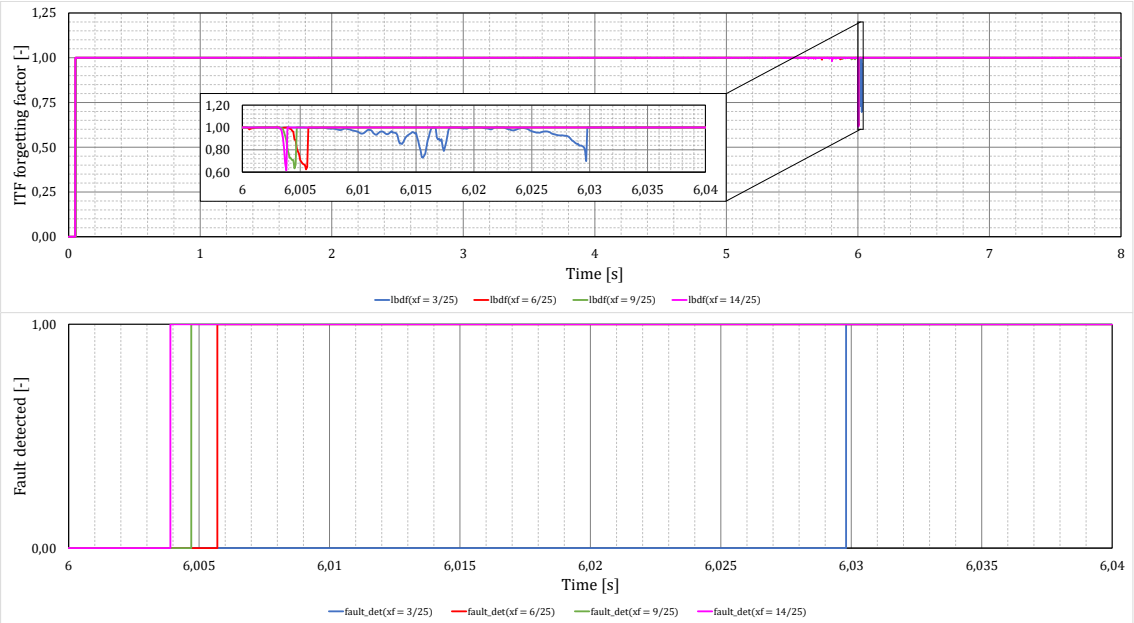

Fig. 4.15: ITF forgetting factor and fault detection, real motor

The waveforms of normalized fault relevance are visualized in Figure 4.16.

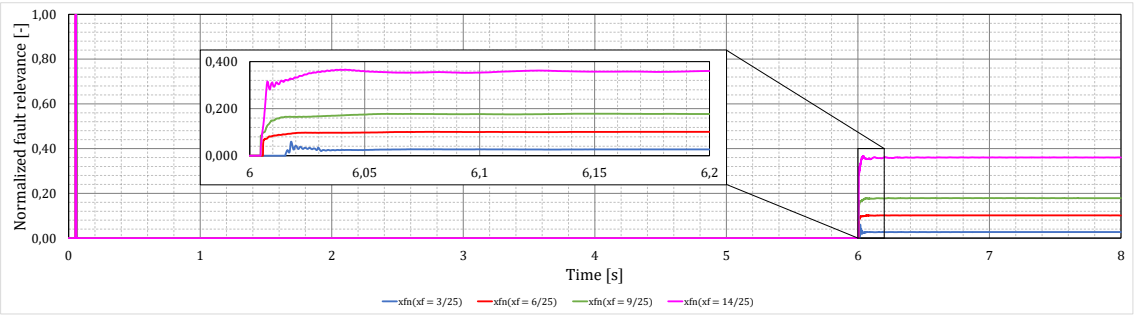

Fig. 4.16: Identified normalized fault relevance, real motor

The estimated series resistance $R_s = 0.425\,\Omega$ is then utilized to calculate $x_{f,n}$ reference, and the fault relevance error is evaluated in the table bellow:

Tab. 4.2: The error of estimated normalized fault relevance, real motor

x_f [−]	3/25	6/25	9/25	14/25
calculated $x_{f,n}$ [-]	0.0329	0.1033	0.1912	0.3573
estimated $x_{f,n}$ [-]	0.0270	0.1014	0.1786	0.3603
error [%]	17.9	1.8	6.6	0.8

Conclusion

In this thesis, the modeling of a synchronous motor with permanent magnets under the stator winding's inter-turn short circuit fault was described (Chapter 1). The model that assumes the combination of serial and parallel winding connections was defined in the stator variables and transformed into the rotor reference frame. It was shown that the model utilizes the well-known healthy motor description (1.25) and one additional differential equation related to the current flowing through the short circuit (1.26). Both model's parts are then linked by the coupling equation (1.24). The presented models were validated via measurement of the fault current's first harmonic and the second harmonic of the back electromotive force transformed into the rotor reference frame (Figure 1.9). The measurement was performed on a configurable machine driven by a dynamometer, at different winding connections, fault relevance, and electrical angular velocities. The measured values were compared with the simulated ones, using the mean relative error and variance (Table 1.3). The mean relative error did not exceed 4.4 %.

In Chapter 2, the field-oriented control of permanent magnet synchronous motors was described. The control system utilizes the dynamical decoupling technique inside the current controller (Figure 2.1), and the parameters of the velocity and current controllers are analytically calculated out of the estimated motor's parameters as in (2.6). The clamping (Figure 2.2) and back-calculation (Figure 2.4) anti-windup techniques are then incorporated into the discrete-time equivalent of the control system. The discrete-time implementation of angle tracking observer and space vector modulation is also described. The control system is programmed into the AURIX application kit TC277 and applied to control the experimental motor with different winding connections to the velocity setpoint (Figure 2.8).

The model derived in Chapter 1 is semi-analytically discretized in Chapter 3. For this purpose, the linear time-varying systems approach is utilized. The electrical angular velocity is considered the time-varying parameter with the defined integral that is equal to the electrical angle. The discrete-time model is then transformed into the stator reference frame to maximize the persistence of input signals resulting in description (3.28). The validation of the discrete-time model is then based on the comparison with the continuous-time model within the simulation (Figure 3.3).

The fault relevance identification is described in Chapter 4 together with the system noise analysis and filter design. For the purpose of parametric estimation, the regularized algorithm with the variable exponential forgetting is applied. Reaching the lower bound of the forgetting factor is then interpreted as a fault presence indicator. The designed fault relevance diagnostic procedure is firstly validated within the simulation (Figures 4.8, 4.9, 4.10, and 4.11). The precision of identified

fault relevance is significantly affected by biases in estimated parameters (especially in estimated series resistance). Relative errors between estimated and calculated normalized fault relevance are presented in Table 4.1. Similarly, the algorithm is validated on the experimental motor (Figures 4.12, 4.13, 4.14, 4.15, and 4.16). Calculated relative errors of normalized fault relevance estimations are presented in Table 4.2.

Together with the electrical parameters of a machine, the identified normalized fault relevance provides necessary information for fault current estimation. Therefore, in future work, the designed fault detector will be extended by the fault compensator that will utilize the identified parameters to calculate fault current and modify control actions to compensate for the fault.

Bibliography

[1] A. K. Bonnett and G. C. Soukup, "Cause and analysis of stator and rotor failures in 3-phase squirrel cage induction motors," Conference Record of 1991 Annual Pulp and Paper Industry Technical Conference, Montreal, Quebec, Canada, 1991, pp. 22-42, doi: 10.1109/PAPCON.1991.239667.

[2] L. Zezula, Inter turn short-circuit detection in vector controlled PMS motor using AI, Brno, 2020, 60 p. Bachelor thesis. Brno University of Technology, Faculty of Electrical Engineering and Communication, Department of Control and Instrumentation. Advised by doc. Ing. Petr Blaha, Ph.D.

[3] S. Toma, L. Capocchi and G. Capolino, "Wound-Rotor Induction Generator Inter-Turn Short-Circuits Diagnosis Using a New Digital Neural Network," in IEEE Transactions on Industrial Electronics, vol. 60, no. 9, pp. 4043-4052, Sept. 2013, doi: 10.1109/TIE.2012.2229675.

[4] P. J. Broniera, W. S. Gongora, A. Goedtel and W. F. Godoy, "Diagnosis of stator winding inter-turn short circuit in three-phase induction motors by using artificial neural networks," 2013 9th IEEE International Symposium on Diagnostics for Electric Machines, Power Electronics and Drives (SDEMPED), Valencia, 2013, pp. 281-287, doi: 10.1109/DEMPED.2013.6645729.

[5] K. Kim, "Simple Online Fault Detecting Scheme for Short-Circuited Turn in a PMSM Through Current Harmonic Monitoring," in IEEE Transactions on Industrial Electronics, vol. 58, no. 6, pp. 2565-2568, June 2011, doi: 10.1109/TIE.2010.2060463.

[6] L. Otava, Monitoring and Diagnosis Algorithms for Synchronous Motor Drives, Brno, 2021, 142 p. Doctoral thesis. Brno University of Technology, Faculty of Electrical Engineering and Communication, Department of Control and Instrumentation. Advised by prof. Ing. Pavel Václavek, Ph.D.

[7] I. B. A. Bazine, S. Tnani, T. Poinot, G. Champenois and K. Jelassi, "On-line detection of stator and rotor faults occurring in induction machine diagnosis by parameters estimation," 8th IEEE Symposium on Diagnostics for Electrical Machines, Power Electronics & Drives, Bologna, 2011, pp. 105-112, doi: 10.1109/DEMPED.2011.6063609.

[8] A. Sarikhani and O. A. Mohammed, "Inter-Turn Fault Detection in PM Synchronous Machines by Physics-Based Back Electromotive Force Estimation," in IEEE Transactions on Industrial Electronics, vol. 60, no. 8, pp. 3472-3484, Aug. 2013, doi: 10.1109/TIE.2012.2222857.

[9] S. Nadarajan, S. K. Panda, B. Bhangu and A. K. Gupta, "Online Model-Based Condition Monitoring for Brushless Wound-Field Synchronous Generator to Detect and Diagnose Stator Windings Turn-to-Turn Shorts Using Extended Kalman Filter," in IEEE Transactions on Industrial Electronics, vol. 63, no. 5, pp. 3228-3241, May 2016, doi: 10.1109/TIE.2016.2535959.

[10] A. Mahmoudi, I. Jlassi, A. J. Marques Cardoso, K. Yahia and M. Sahraoui, "Inter-Turn Short-Circuit Faults Diagnosis in Synchronous Reluctance Machines, Using the Luenberger State Observer and Currents Second-Order Harmonic," in IEEE Transactions on Industrial Electronics, doi: 10.1109/TIE.2021.3109514.

[11] S. K. Sul, Control of electric machine drive system, Hoboken, N.J.: Wiley-IEEE Press, 2011, ISBN 978-0-470-59079-9.

[12] P. Krause, O. Wasynczuk, S. D. Sudhoff and S. Pekarek, Analysis of electric machinery and drive systems, Third edition, Hoboken, N.J.: Wiley-IEEE Press series on power engineering, 2013, ISBN 978-1-118-02429-4.

[13] B. Du, S. Wu, S. Han and S. Cui, "Interturn Fault Diagnosis Strategy for Interior Permanent-Magnet Synchronous Motor of Electric Vehicles Based on Digital Signal Processor," in IEEE Transactions on Industrial Electronics, vol. 63, no. 3, pp. 1694-1706, March 2016, doi: 10.1109/TIE.2015.2496900.

[14] A. Sarikhani and O. A. Mohammed, "Inter-Turn Fault Detection in PM Synchronous Machines by Physics-Based Back Electromotive Force Estimation," in IEEE Transactions on Industrial Electronics, vol. 60, no. 8, pp. 3472-3484, Aug. 2013, doi: 10.1109/TIE.2012.2222857.

[15] B. Gu, "Study of IPMSM Interturn Faults Part I: Development and Analysis of Models With Series and Parallel Winding Connections," in IEEE Transactions on Power Electronics, vol. 31, no. 8, pp. 5931-5943, Aug. 2016, doi: 10.1109/T-PEL.2015.2496142.

[16] G. Xingye, L. Chuang, Z. Yuefei and W. Kai, "Analysis and dynamic decoupling control schemes for PMSM current Loop," 2016 IEEE International Conference on Aircraft Utility Systems (AUS), Beijing, China, 2016, pp. 570-574, doi: 10.1109/AUS.2016.7748115.

[17] L. Zezula, "IPMSM drive system parameters tuning - an analytic solution," in Proceedings II of the 27th student EEICT 2021 selected papers, 2021, pp. 69-72, ISBN 978-80-214-5943-4.

[18] H. Qin and Z. Wu, “Angle tracking observer with improved accuracy for resolver-to-digital conversion,” Symmetry (Basel), vol. 11, no. 11, p. 1347, 2019, doi: 10.3390/sym11111347.

[19] F. Wang, T. Shi, Y. Yan, Z. Wang and C. Xia, "Resolver-To-Digital Conversion Based on Acceleration-Compensated Angle Tracking Observer," in IEEE Transactions on Instrumentation and Measurement, vol. 68, no. 10, pp. 3494-3502, Oct. 2019, doi: 10.1109/TIM.2018.2882047.

[20] U. Subramaniam, S. M. Bhaskar, D. J.Almakhles, S. Padmanaban, and Z. Leonowicz, “Investigations on EMI Mitigation Techniques: Intent to Reduce Grid-Tied PV Inverter Common Mode Current and Voltage,” Energies, vol. 12, no. 17. MDPI AG, p. 3395, Sep. 03, 2019. doi: 10.3390/en12173395.

[21] P. Vaclavek and P. Blaha, "PMSM model discretization for Model Predictive Control algorithms," Proceedings of the 2013 IEEE/SICE International Symposium on System Integration, 2013, pp. 13-18, doi: 10.1109/SII.2013.6776649.

[22] H. Trabelsi, A. Chbeb and A. Sellami, "Discrete time sliding mode control of PMSM," 2013 International Conference on Electrical Engineering and Software Applications, 2013, pp. 1-6, doi: 10.1109/ICEESA.2013.6578485.

[23] R. Tóth, P. M. J. Van den Hof, and P. S. C. Heuberger, “Discretisation of linear parameter-varying state-space representations,” IET Control Theory & Applications, vol. 4, no. 10. Institution of Engineering and Technology (IET), pp. 2082–2096, Oct. 01, 2010. doi: 10.1049/iet-cta.2009.0572.

[24] E. Kamen, “Fundamentals of Linear Time-Varying Systems,” The Control Systems Handbook, Second Edition. CRC Press, pp. 3-1-3–33, Dec. 08, 2010. doi: 10.1201/b10384-5.

[25] D. S. Bernstein and W. So, "Some explicit formulas for the matrix exponential," in IEEE Transactions on Automatic Control, vol. 38, no. 8, pp. 1228-1232, Aug. 1993, doi: 10.1109/9.233156.

[26] K. E. Atkinson, An Introduction to Numerical Analysis, Second edition, New York, John Wiley & Sons, 1989. ISBN 978-0-471-50023-0

[27] T. Söderström and P. Stoica, System identification, Uppsala, Prentice Hall International, 2001, ISBN 0-13-881236-5.

[28] L. Ljung, System identification - theory for the user, Second edition, Englewood Cliffs, Prentice Hall International, 1999, ISBN 0-13-656695-2.

[29] M. D. Springer, The algebra of random variables, New York, John Wiley & Sons, 1979, ISBN 0-471-01406-0.

[30] L. Buchta, Compensation of nonlinearities in AC motor control algorithms, Brno, 2019, 153 p. Doctoral thesis. Brno University of Technology, Faculty of Electrical Engineering and Communication, Department of Control and Instrumentation. Advised by doc. Ing. Petr Blaha, Ph.D.

[31] J. Dokoupil and P. Václavek, "Regularized Estimation with Variable Exponential Forgetting," 2020 59th IEEE Conference on Decision and Control (CDC), 2020, pp. 312-318, doi: 10.1109/CDC42340.2020.9304385.

Symbols and abbreviations

ATO	Angle Tracking Observer
DC	Direct Current
IPMSM	Interior Permanent Magnet Synchronous Machine
ITF	Inter-Turn Fault
PI	Proportional-Integral
PMSM	Permanent Magnet Synchronous Machine
SPMSM	Surface-mounted Permanent Magnet Synchronous Machine
SVM	Space Vector Modulation

List of appendices

A Derivation of the open-loop ITF model

System definition (ITF is in phase 'a'):

$$\frac{\mathrm{d}}{\mathrm{d}t}\begin{bmatrix} i_{d,h} \\ i_{q,h} \end{bmatrix} = \begin{bmatrix} -\frac{R_s}{L_d} & \frac{L_q}{L_d}\omega_e \\ -\frac{L_d}{L_q}\omega_e & -\frac{R_s}{L_q} \end{bmatrix} \cdot \begin{bmatrix} i_{d,h} \\ i_{q,h} \end{bmatrix} + \begin{bmatrix} \frac{1}{L_d} & 0 \\ 0 & \frac{1}{L_q} \end{bmatrix} \cdot \begin{bmatrix} u_d \\ u_q \end{bmatrix} + \begin{bmatrix} 0 \\ -\frac{\omega_e \lambda_{pm}}{L_q} \end{bmatrix}$$

$$x_f^* = \frac{x_f}{n_s}$$

$$R_f^* = x_f^*(1 - x_f^*)(n_p - 1)R_s + R_f$$

$$L_f = {x_f^*}^2 n_p(n_s - 1)L_{aa}$$

$$\begin{bmatrix} i_d \\ i_q \end{bmatrix} = \begin{bmatrix} i_{d,h} \\ i_{q,h} \end{bmatrix} + \frac{2x_f^*}{3}\begin{bmatrix} \cos(\theta_e) \\ -\sin(\theta_e) \end{bmatrix} i_f$$

$$\frac{\mathrm{d}}{\mathrm{d}t}\left(3L_f i_f\right) = -(x_f^*\left(3 - 2x_f^*\right)R_s + 3R_f^*)i_f + 3x_f^*\begin{bmatrix} \cos(\theta_e) & -\sin(\theta_e) \end{bmatrix} \cdot \begin{bmatrix} u_d \\ u_q \end{bmatrix}$$

Voltage form of the healthy part equations:

$$\begin{bmatrix} u_d \\ u_q \end{bmatrix} = \begin{bmatrix} L_d & 0 \\ 0 & L_q \end{bmatrix} \cdot \frac{\mathrm{d}}{\mathrm{d}t}\begin{bmatrix} i_{d,h} \\ i_{q,h} \end{bmatrix} + \begin{bmatrix} R_s & -L_q\omega_e \\ L_d\omega_e & R_s \end{bmatrix} \cdot \begin{bmatrix} i_{d,h} \\ i_{q,h} \end{bmatrix} + \begin{bmatrix} 0 \\ \omega_e \lambda_{pm} \end{bmatrix}$$

Open-loop assumption:

$$i_d = 0$$

$$i_q = 0$$

$$\begin{bmatrix} i_{d,h} \\ i_{q,h} \end{bmatrix} = \frac{2x_f^*}{3}\begin{bmatrix} -\cos(\theta_e) \\ \sin(\theta_e) \end{bmatrix} i_f$$

Expressing derivative of the coupling equation:

$$\frac{\mathrm{d}}{\mathrm{d}t}\begin{bmatrix} i_{d,h} \\ i_{q,h} \end{bmatrix} = \frac{2x_f^*}{3}\begin{bmatrix} \sin(\theta_e) \\ \cos(\theta_e) \end{bmatrix} i_f + \frac{2x_f^*}{3}\begin{bmatrix} -\cos(\theta_e) \\ \sin(\theta_e) \end{bmatrix} \frac{\mathrm{d}i_f}{\mathrm{d}t}$$

Substituting for the healthy currents derivative and healthy currents in the voltage equation:

$$\begin{bmatrix} u_d \\ u_q \end{bmatrix} = \frac{2x_f^*}{3}\begin{bmatrix} L_d & 0 \\ 0 & L_q \end{bmatrix} \cdot \left(\begin{bmatrix} \sin(\theta_e) \\ \cos(\theta_e) \end{bmatrix} i_f + \begin{bmatrix} -\cos(\theta_e) \\ \sin(\theta_e) \end{bmatrix} \frac{\mathrm{d}i_f}{\mathrm{d}t}\right) + \frac{2x_f^*}{3}\begin{bmatrix} R_s & -L_q\omega_e \\ L_d\omega_e & R_s \end{bmatrix} \cdot \begin{bmatrix} -\cos(\theta_e) \\ \sin(\theta_e) \end{bmatrix} i_f + \begin{bmatrix} 0 \\ \omega_e \lambda_{pm} \end{bmatrix}$$

Substituting for the voltages in the fault current equation and expressing the derivative:

$$Z_f = \frac{\left((R_f^* + x_f^* R_s) + \left(\frac{\mathrm{d}L_f}{\mathrm{d}t} + {x_f^*}^2 \frac{\mathrm{d}L_{aa}}{\mathrm{d}t}\right)\right)}{\left(L_f + {x_f^*}^2 L_{aa}\right)}$$

$$\frac{\mathrm{d}i_f}{\mathrm{d}t} = -Z_f i_f - \frac{x_f^* \omega_e \lambda_{pm} \sin(\theta_e)}{\left(L_f + {x_f^*}^2 L_{aa}\right)}$$

Substituting for the fault current derivative in the voltage equation and expressing

the back electromotive force:

$$\begin{bmatrix} u_d \\ u_q \end{bmatrix} = \frac{2}{3} \begin{bmatrix} L_d x_f^* Z_f - R_s x_f^* & -x_f^* \omega_e (L_d - L_q) \\ -x_f^* \omega_e (L_d - L_q) & L_q x_f^* Z_f - R_s x_f^* \end{bmatrix} \cdot \begin{bmatrix} \cos(\theta_e) \\ -\sin(\theta_e) \end{bmatrix} i_f + \lambda_{pm} \omega_e \begin{bmatrix} \frac{x_f^{*2} L_d \sin(2\theta_e)}{3\left(L_f + x_f^{*2} L_{aa}\right)} \\ 1 - \frac{x_f^{*2} L_q (1 - \cos(2\theta_e))}{3\left(L_f + x_f^{*2} L_{aa}\right)} \end{bmatrix}$$

Figure A.1 shows the realization of open-loop ITF model in MATLAB Simulink.

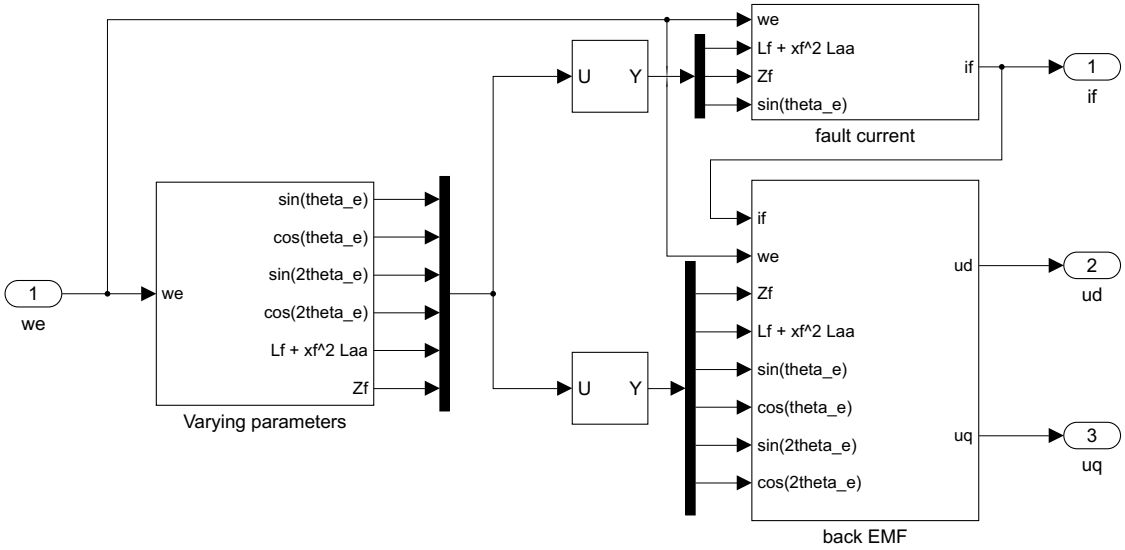

Fig. A.1: Open-loop ITF model realization in MATLAB Simulink

B Content of the electronic attachment

- `/` ..... root of the attached archive
  - `Thesis.pdf` ..... text of the diploma thesis
  - `Models_codegen` ..... MATLAB Simulink models for c-code generating
    - `ctrl_core.slx` ..... control system model
    - `fault_diag.slx` ..... model of fault relevance detector
  - `Models_sim` ..... MATLAB Simulink models for simulations
    - `discr_mod_val.slx` ..... model for discrete-time equivalent verification
    - `fault_diagnostics.slx` ..... model for fault diagnostics testing
    - `ITF_model.slx` ..... model of control system and shorted machine
    - `open_loop_model.slx` ..... model for open-loop shorted machine validation

NOTE: The MATLAB Simulink models are realized in the MATLAB version R2020b.